Understanding near Fermi-level electronic structure through x-ray emission spectroscopy

Devon R. Mortensen

A dissertation

submitted in partial fulfillment of the

requirements for the degree of

Doctor of Philosophy

University of Washington

2016

Reading Committee:

Gerald T. Seidler, Chair

Marjorie Olmstead

Xiaodong Xu

Program Authorized to Offer Degree:

Physics

University of Washington

Abstract

Understanding near Fermi-level electronic structure through x-ray emission spectroscopy

Devon R. Mortensen

Chair of the Supervisory Committee:
Professor Gerald T. Seidler
Physics

Atomic and molecular chemical properties are largely determined by the electronic structure of near Fermi-level states. Determining this structure is therefore one of the central tasks in materials characterization and development. In the work of this dissertation I explore the capabilities and limitations of non-resonant x-ray emission spectroscopy (NXES) as an analytical technique aimed at addressing these issues. To this end, I report the development of novel laboratory- and synchrotron-based instrumentation for the study of transition metal and lanthanide compounds. One of the primary results of this research thrust is increased accessibility and throughput, making NXES measurements a more viable option in routine and research-grade materials study. Using experimental data obtained from these spectrometers, I evaluate current state-of-the-art theory in terms of modeling valence structure in ambient

transition-metal complexes. Additionally, I use NXES to elucidate the evolving 4f-electronic structure in the early light lanthanides under pressure. In particular these results show a persistent 4f-moment across certain volume collapse transitions in Cerium and Praseodymium, thus helping settle a long-standing debate about the nature of volume collapse.

TABLE OF CONTENTS

LIST OF FIGURES

LIST OF TABLES

ACKNOWLEDGEMENTS

"Sometimes our light goes out but is blown into flame by another human being. Each of us owes deepest thanks to those who have rekindled this light." –Albert Schweitzer

Graduate school, like life, is often fraught with difficulties. My own experience has been no exception. I would not be submitting this dissertation were it not for a great number of people in my life. I would like to sincerely thank my advisor Jerry Seidler, whose lessons have extended well beyond the realm of x-ray physics. None of this work would have been possible without him or the many collaborators I have worked with throughout my studies. You are far too many to list, but I greatly appreciate all you taught me. I am thankful to all my group members, former and present for sharing this journey with me. I would also like to acknowledge the United States Department of Energy, Pacific Northwest National Laboratory, Lawrence Livermore National Laboratory, and the University of Washington Clean Energy Institute for funding my research.

Lastly, and with deepest gratitude, I would like to thank my family and friends. You stood by me when my light went out and shone your own flames to light my path. I would truly not be here without you. Thank you for your love and support.

Chapter 1. INTRODUCTION

1.1 OUTLINE OF DISSERTATION

In the course of this dissertation, I will discuss the application of non-resonant x-ray emission spectroscopy (NXES) in understanding the near Fermi-level electronic structure in transition metal and lanthanide compounds and complexes. As valence-level orbitals are those most sensitive to the local environment they are an excellent source for information on chemical state (spin, oxidation, bonding, pressure, temperature, etc.).

In the remainder of this chapter I outline how these orbitals are probed using hard x-ray techniques. I begin with a broad overview of x-ray spectroscopy (Section 1.2) before focusing more closely on NXES (Section 1.4) which is the primary experimental method employed in this work. Chapter 2 surveys the landscape of instrumentation, both tabletop and large facility-based, employed for these techniques. In Chapter 3, I discuss in detail the weakest of all emission lines, the so-called valence-to-core (VTC). Here I present several examples of application as well as a review of the theoretical framework for modeling x-ray spectra.

In Chapters 4–6, I report the development and refinement of a robust, versatile monochromator for high-resolution laboratory-based x-ray spectroscopic studies. These instruments fill a unique space in x-ray spectroscopy capability: entry-level and routine research-grade. Prior to this work the ability to perform these advanced analytical methods was almost exclusively confined to a handful of large-scale, state-funded synchrotron and x-ray free electron laser facilities. In addition to enabling fine studies of weak valence-to-core emission lines, such as is discussed in Chapter 7, we predict that this work will prove to have broad applicability in the scientific

community and will expand the reach and availability of x-ray spectroscopy as routine characterization method.

In Chapter 8, I detail the design and performance of a medium-resolution x-ray emission spectrometer. The intermediate resolution provided by this instrument is well matched to the study of lanthanide fluorescence lines where intrinsic physical properties limit the achievable resolution to 3-5 eV, achieving vastly superior count rates to high-resolution instruments without loss of information. This spectrometer was successfully employed in a study examining the nature of f-electrons and their evolution under extreme pressures, reported in Chapter 9. In Chapter 10, I conclude and provide an outlook for the future directions of this work.

1.2 Overview of X-ray Spectroscopy

X-ray radiation is perfectly matched to both atomic energy levels and interatomic spacings, making them ideally suited for the study of electronic and local structure in atoms and molecules. The interaction of x-rays with matter can be grouped into three distinct scattering categories: 1) photoabsorption; 2) elastic Rayleigh scattering; and 3) inelastic Compton scattering. In the following sections, and in the work of this thesis, I focus on a subset of spectroscopies falling under photoabsorption, namely x-ray absorption fine structure (XAFS) and non-resonant x-ray emission spectroscopy (XES). In particular, I will discuss how these techniques can be applied to elucidate valence-level electronic structure in a material.

Unlike diffraction-based methods, x-ray spectroscopy is a localized atomic probe which does not require long range crystallinity. As such it is one of only a small number of analytical techniques equally suited to crystalline and amorphous, heterogeneous or nano-crystalline systems. Furthermore, because each element has its own unique characteristic atomic energy levels, x-ray spectroscopy is an inherently element-selective technique.

While it is possible to apply these techniques as a direct probe of the Fermi-level electronic states (e.g., L-edge spectroscopy in transition metals), it is often quite difficult in practice. These orbitals are typically bound by less than 1.5 keV, which falls into the soft x-ray regime. The small absorption length of low energy x-rays or electrons in air (μm scale) imposes sizeable experimental constraints, requiring the use of ultra-high vacuum. Similarly, the minimal penetration into solids (nm scale) means the measurement is fundamentally limited to surface-level sampling. Such a restriction means sample preparation is frequently an arduous task and many sample conditions required for *in-situ* operation are difficult to implement.

When bulk-sensitivity and/or complex sample environments (absorbing matrices, high pressure cells, cooling refrigerators, furnaces, etc.) are required, hard x-ray spectroscopy is a much better suited technique. When working in the hard x-ray regime (> 5 keV), the radiation typically penetrates cm-to-m in air or helium environments and 10-100 μm into the sample bulk, thus circumventing the limitations discussed above.

Instead of directly interrogating valence electrons, hard x-ray spectroscopy instead targets core-level states. The wave functions of deep-core electrons, however, overlap with those from the valence and the resulting spectra therefore contain indirect information on near-Fermi level physics. In Sections 1.3 and 1.4, I detail the sensitivity of hard x-ray XAFS and XES to valence shell structure.

1.3 X-RAY ABSORPTION FINE STRUCTURE

X-ray absorption fine structure (XAFS) is a measurement of the energy dependence of photoabsorption probability at energies around the binding energy of core-level electrons. The primary metric of interest is the x-ray absorption coefficient, $\mu(E)$, derives from Beer's law:

$$P = e^{-\mu(E)t} \tag{1.1}$$

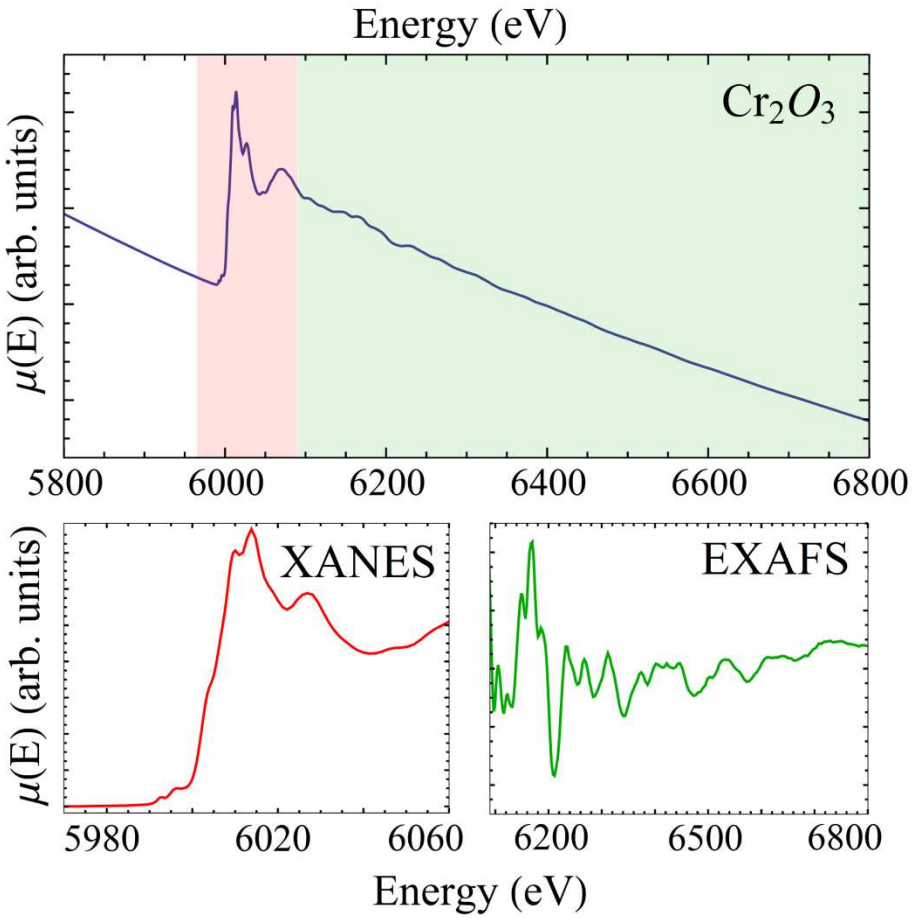

Figure 1.1. Top: Absorption coefficient, $\mu(E)$, for Cr_2O_3 powder. Bottom left: XANES region with pre-edge and white line features. Bottom right: EXAFS region normalized to the atomic background to emphasize oscillations. Data was collected from Cr_2O_3 powder on Kapton tape in transmission mode at a synchrotron light source.[1]

where P is the absorption probability and t is the thickness of the sample. Because of electron-electron interactions and the wave nature of photoelectrons, $\mu(E)$ contains a rich structure indicative of local geometry and chemical state. The sensitivity of XAFS to oxidation state and coordination chemistry has made it a mainstay in a range of scientific fields such as catalysis, electrochemistry, organic chemistry, geology, and materials research.

XAFS is typically divided into two regimes, as shown in Figure 1.1, each with distinct materials information: x-ray absorption near edge structure (XANES) and extended x-ray absorption fine structure (EXAFS).

1.3.1 X-RAY ABSORPTION NEAR EDGE STRUCTURE

The XANES region consists of incident x-rays within a ~100 eV band of the electron binding energy (see Figure 1.1 bottom left). At energies slightly below the edge, the so-called "pre-edge" region, a core electron can be promoted to non-continuum states resulting in increasedμ. The size of these features is usually quite weak but can in some instances rival the intensity of the main absorption edge depending on symmetry. The absorption rises sharply as the incident x-ray energy approaches the binding energy, corresponding to excitation of a core electron into unbound, continuum states. This first large peak is commonly referred to as the "white line" as absorption spectra were historically measured by exposing photographic plates. Immediately above the edge are a number of absorption modulations caused by interference effects in the outgoing and back-scattering photoelectron wave function. The oscillations in this regime are irregular due to the contribution of multiple-scattering events from all atoms in the local environment.[2]

In general, XANES exhibits extreme sensitivity to oxidation state. In particular the absorption edge shifts to higher energy with increased metal oxidation. While the theoretical model of XANES is well established, it is often sufficient to simply compare the absorption edge energy to that of known reference to extract mean oxidation state and distribution of the local environment via fingerprinting or principal component analysis. The prominence of multiple-scattering interference effects also means that XANES contains information on coordination symmetry.

1.3.2 Extended X-ray Absorption Fine Structure

When multiple-scattering gives way to primarily few-scattering events we enter the EXAFS regime (see Figure 1.1 bottom right). This region typically begins ~100 eV above the binding edge and extends ~800-1000 eV past. Here the absorption modulations are broad and smooth (the result of short-scattering paths being dominant) and are composed of various oscillation frequencies corresponding to scattering from different near-neighbor shells. Analysis of the frequency content is therefore used to determine coordination number and near-neighbor distances. In principle EXAFS modeling can also determine ligand species, although as we will discuss in Section 1.4.3 there are complications in resolving ligands of similar atomic number.[3]

1.4 Non-resonant X-ray Emission Spectroscopy

X-ray emission is a second order process following from the creation of a photoelectron in an absorption event as discussed in Section 1.3. The resultant deep-core-hole is unstable and is quickly (~few femtoseconds) filled by de-excitation of a higher-orbital electron. To conserve energy this downward transition is accompanied by either photon emission or promotion of a second electron (the so-called Auger effect), the former being the observed event in x-ray emission spectroscopy (XES). The energy of the fluoresced photon depends on the initial orbital of the downward transitioning electron. Each subshell shows fine structure in emission resulting from electron interactions. It is the ability to resolve these fine features which distinguishes XES from the more common technique of x-ray fluorescence (XRF), which is used extensively for elemental analysis. The achievement of fine resolution in experiment is discussed in Chapter 2.

Emission lines are labeled according to the shell of the core-hole and intensity. For example, an x-ray resulting from the filling of a K-shell hole is called K fluorescence. The most intense of

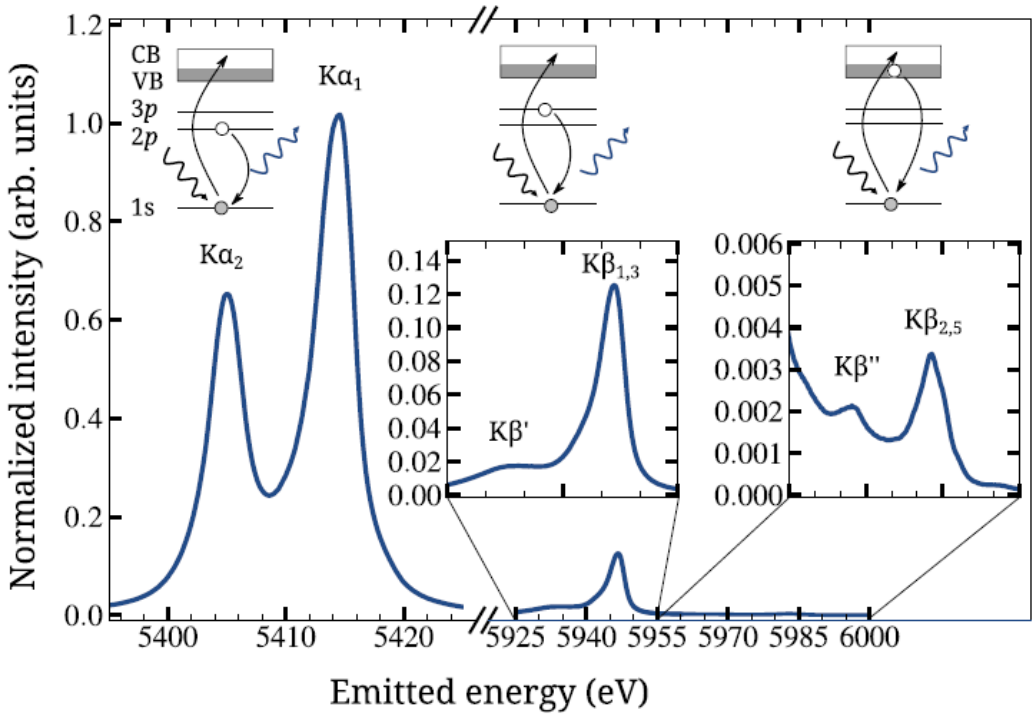

Figure 1.2. Cr K fluorescence in Cr_2O_3. Intensity has been normalized to the $K\alpha_1$ peak. Insets showed magnified views (note the scales). Above each emission line is an energy level diagram showing the initial excitation of a core-level electron into the conduction band (CB) and the corresponding de-excitation from atomic orbitals or the valence band (VB). Reproduced from M. Rovezzi and P. Glatzel, Semiconductor Science and Technology **29** (2), 19 (2014)[4].

these K fluorescence lines are called α, followed by β, then γ, etc. Lastly, a number is appended to each line which indicates the originating subshell of the de-excited electron. The numbering scheme is largely historical, being borrowed from neutron scattering. As such the progression in numbering typically does not follow any meaningful physical pattern. As an example of labeling in 3d-transition metal XES, the most intense emission lines are $K\alpha_1$ and $K\alpha_2$, corresponding to $2p_{3/2} \rightarrow 1s_{1/2}$ and $2p_{1/2} \rightarrow 1s_{1/2}$ respectively.

The following sections outline the various emission lines and their sensitivity to the local chemical environment. For brevity I will discuss only major K fluorescence in 3d-transition metal complexes. More exhaustive descriptions of emission lines can be found elsewhere.[5-8]

1.4.1 Kα EMISSION

Kα emission corresponds to 2p → 1s transitions (see Figure 1.2). While these lines are the most intense due to the large overlap of the 2p orbitals with the 1s core-hole, they show the weakest coupling to valence structure. The splitting between $K\alpha_1$ and $K\alpha_2$ is dominated by spin-orbit interactions. The widths, however, of each feature are in principle governed by (2p,3d) exchange and according to multiplet theory scales linearly with spin state. A number of studies have verified the effectiveness of this method.[9-11]

Because the Kα lines are largely indifferent to local chemical environment, they are also at times useful as internal calibrants for measuring relative intensity changes in the weaker emission lines. For example, changes in the branching ratio between Kβ and Kα fluorescence have been used as a marker for determining valence electron structure in 3d-transition metals.[12-17]

1.4.2 Kβ EMISSION

Kβ emission is roughly 8-10 times weaker than Kα and several hundred eV higher in energy for the 3d-transition metals. These features can be divided into two main regions as shown in Figure 1.2. The main $K\beta_{1,3}$ peak is due to direct 3p → 1s transitions. Unlike for the 2p orbitals, here the spin-orbit interactions are weak and the splitting between the transitions from $3p_{1/2}$ and $3p_{3/2}$ are unresolvable to within the intrinsic broadening of the finite core-hole lifetime. Upon de-excitation of the 3p electron there is a small probability that the 3d valence band will respond to

the sudden change in screened potential by flipping spin.[18, 19] This effect gives rise to a slightly lower energy feature which in turn causes the asymmetry in the $K\beta_{1,3}$ peak. Energy shifts in $K\beta_{1,3}$ peak position indicate changes in the spin state and other electronic properties.[16] In fact, the shift of $K\beta_{1,3}$ (on the order of ~1 eV) has been shown to be a more reliable metric in measuring oxidation state than edge shifts in XANES.[20-24]

The second region is the Kβ′ peak, which arises from (3p,3d) exchange interaction. In the final state there is a hole in the 3p subshell which has two possible spin orientations. Interaction with the spin of the 3d valence band breaks the degeneracy of this state causing the splitting between the $K\beta_{1,3}$ and Kβ′ features. As such, the Kβ′ peak is an excellent candidate for elucidating metal-ion spin state. A number of careful studies have shown that both the intensity and separation of Kβ′ with respect to $K\beta_{1,3}$ scale with increased oxidation and valence spin.[16, 19, 20]

1.4.3 VALENCE-TO-CORE EMISSION

At energies slightly below the K-edge there are a number of weak emission features referred to as Kβ satellite or valence-to-core (VTC) lines (see Figure 1.2). In contrast to the core-to-core transitions discussed above, which have only indirect coupling to valence structure, these emissions involve direct transitions from valence-band orbitals to the 1s hole and are therefore the most sensitive to changes in the chemical environment. The VTC region has two dominate features, $K\beta_{2,5}$ and Kβ″, which correspond to transitions from metal valence and ligand electronic states respectively. The intensity of VTC emission is attributed mainly to dipole transitions from metal valence and ligand electron states with p-character ($K\beta_{2,5}$) and from ligand s-states (Kβ″).[25-28] Quadrupole transitions from d-character states can in some cases also be a significant contribution.[29, 30] As a result of the weaker 1s overlap, these lines are 50-100 times weaker than the main Kβ.

As is the case with the $K\beta_{1,3}$ lines discussed above, the $K\beta_{2,5}$ peak shifts in energy with changings in screening make it an excellent fingerprint of oxidation state. Unlike $K\beta_{1,3}$, however, $K\beta_{2,5}$ exhibits an opposite energy shift more similar to the behavior of the white line in XANES.[23, 24, 31]

The ligand-to-metal cross-over transition (Kβ″) contains a wealth of information related to bonding. While EXAFS is successful in extracting coordination number and bond-lengths it does a poor job at ligand speciation, particularly when between light atom ligands of similar atomic number such as C, N, and O.[3, 32, 33] Such ambiguity poses serious problems in analysis especially for catalysis. The location of the Kβ″ peak in XES, however, depends strongly on the ligand 2s binding energy and hence is a sensitive index of ligand speciation.[31, 33-37] Furthermore, it has been shown that the Kβ″ intensity relative to $K\beta_{2,5}$ scales logarithmically with metal-ligand bond length.[35, 38-40]

I will discuss VTC-XES in greater depth in Chapter 3. In Section 3.2, I give several recent practical applications in the fields of catalysis and environmental remediation. Additionally, I present the theoretical background of VTC emission in Section 3.3.

Chapter 2. SURVEY OF INSTRUMENTATION

In this chapter, I review x-ray instrumentation. In Section 2.1, I provide a broad overview of x-ray methods. The most common spectrometers are based on wavelength-dispersive methods which fall into focusing and dispersive geometries as discussed in Sections 2.2 and 2.3 respectively. In Sections 2.4 and 2.5, I provide a brief survey of synchrotron- and laboratory-based implementations.

2.1 BACKGROUND

In experimental practice, each of the spectroscopies discussed in Chapter 1 depend on isolating energy bands in either the incident (XAFS) or emitted radiation (XES). The methods for doing so fall into two main categories: energy dispersion and wavelength dispersion. The former is usually accomplished via semiconductor, scintillation, or gas ionization detectors which deduce energy deposition via photoelectron current or luminescence generated by absorption events. While these detectors offer high quantum efficiencies the achievable resolutions range from several hundred to thousands of eV, which is insufficient to resolve the fine features in XAFS and XES discussed in Chapter 1. These detectors are useful, however, when used in tandem with wavelength-dispersive instrumentation to isolate monochromatized signal from background contributions thereby providing enhanced signal-to-noise compared to integrating detectors.

A new class of energy dispersion based on cryogenic superconducting detectors utilizing calorimetric energy detection, has been shown to achieve resolutions of a few eV.[41, 42] This capability is potentially suitable for some studies requiring intermediate resolution. The major drawback of these systems is the requirement of maintain operating temperatures below 1 K and, at present, low count rates before detector saturation.

The vast majority of x-ray emission spectroscopy, however, relies on wavelength-dispersive crystal spectrometers. A review of these instruments forms the remainder of this chapter.

2.1.1 BRAGG DIFFRACTION

Wavelength-dispersive methods are founded upon the geometric energy dependence of x-ray diffraction in periodic crystals as discovered by William Lawrence Bragg and William Henry Bragg in 1913:

$$n\lambda = 2d \sin\theta \tag{2.1}$$

where n is the order of diffraction, λ the wavelength of diffracted x-rays, d the spacing of the crystallographic planes, and θ the diffraction angle.[43] In honor of the Braggs' discovery the diffraction angle is typically referred to as the Bragg angle, θ_B.

In x-ray spectroscopy it is often advantageous to work in terms of energy rather than wavelength. Eq. (2.1) can be recast in energy space as:

$$E = E_0 / \sin\theta_B \tag{2.2}$$

with E being the energy of the diffracted photon and E_0 the backscatter energy (i.e., $\theta_B = 90°$) for the chosen crystal diffraction planes and order. The resolving power of diffraction-based dispersion is found by differentiating eq. (2.2):

$$E/\Delta E = \tan\theta_B / \Delta\theta \tag{2.3}$$

where the angular spread $\Delta\theta$ includes both geometric factors from the incident radiation and intrinsic broadening from the crystal rocking curve. High-resolution crystal spectrometers, such as are presented in this chapter, offer resolving powers of 10^3-10^5 far outstripping the capability of all traditional energy-dispersive detectors (10^1-10^2). It is this exact quality which makes wavelength-dispersion the dominant instrumentation utilized in x-ray spectroscopy.

The two main approaches towards wavelength-dispersive spectroscopy are point-to-point scanning (focusing) and fixed (dispersive) instruments. Each setup has its own unique advantages and challenges. Focusing spectrometers provide excellent rejection of background and offer the highest possible resolutions. Each spectrum, however, is collected in pieces, which requires high precision in monitoring incident flux as well as completely ruling out "single-shot" experiments such as those at x-ray free electron lasers and laser-shock facilities. Dispersive methods, on the other hand, record the full spectrum all at once, enabling single-shot mode. The requirement of large, exposed detector areas, however, means that signal-to-noise is necessarily reduced, compared to focusing geometries, and there are increased systematic errors due to inhomogeneous effects of stray scatter.

2.1.2 CURVED CRYSTALS

To this point we have made no reference to diffraction in extended crystals. The simplest case is flat crystals. These planar crystals work well with highly collimated x-ray beams, such as those produced at synchrotron light sources and free-electron lasers. When coupled to a diverging source, however, each point on the crystal will be struck at a slightly different incident angle, thus satisfying Bragg's Law for different energies. It is therefore often advantageous to curve the crystal such that the portions, or the entirety, of the analyzer will output in the same energy bandwidth. Depending on the application, cylindrical, spherical, toroidal, logarithmic, and other more complex shapes can be employed.

As spherically-bent Bragg crystal analyzers (SBCAs) are particularly relevant to the discussions in Sections 2.2 and Chapter 3-5, I will describe them briefly here. SBCAs are manufactured by bonding or gluing flat wafers to a concave glass lens.[44-46] Special care must be

taken to ensure the bonding is even and free of contaminants as any imperfections in the resulting analyzer surface will negatively affect resolution and efficiency.

In principle, a tighter radius of curvature allows for closer working distances and subsequently higher solid angle collection. In practice, however, the achievable curvature is limited by lattice strains introduced in elastic deformation. Such strains significantly broaden the intrinsic rocking curve, degrading resolution. Taken to the furthest extent the strains will overcome the wafer elastic limit causing breakage. The magnitude of the strain is most intense along the edges and scales with crystal size. As a result, the vast majority of applications use SBCAs with 10-cm diameter and 1-m curvature. A handful of methods exist aimed at circumventing these issues including stripping or dicing to relieve strain and approximating the curved surface with small, flat crystals.

2.2 FOCUSING CRYSTAL SPECTROMETERS

2.2.1 THE ROWLAND CIRCLE

Modern focusing x-ray spectrometers are rooted in various designs developed in the 1930's.[47-50] Each of these schemes in turn draw from the geometry of the Rowland circle which was first employed in optical grating spectrometers.[51] It was found that for x-ray Bragg diffraction there exists a circle, with diameter equal to the optic radius of curvature, on which the divergence from a point source has the same angle of incidence at all points on the optic surface. This criterion naturally results in the diffracted light being refocused to the symmetrically opposite on-circle location as shown in Figure 2.1.

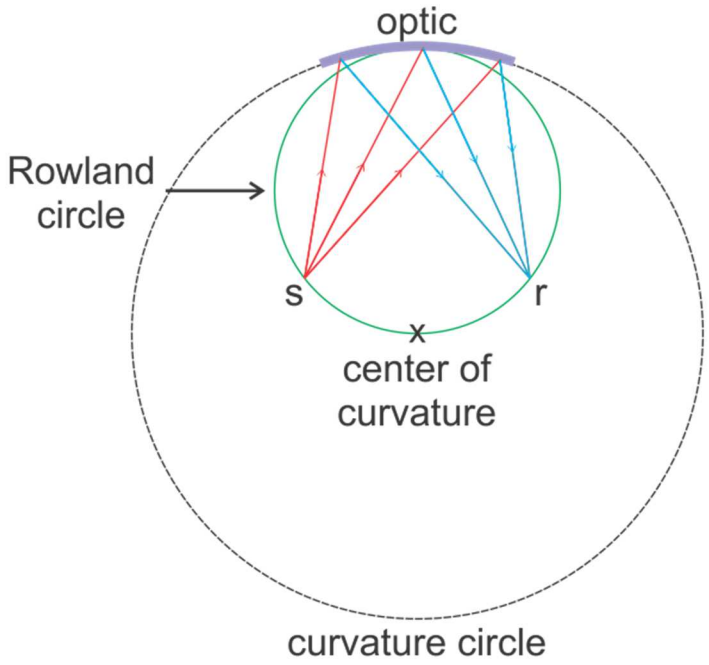

Figure 2.1. The Rowland circle geometry. For a concave diffractive optic (purple arc), there exists a Rowland circle (green) such that the divergence from a point source (s) is refocused back onto the circle (r) after diffracting from the optic.

The earliest implementations of this geometry made use of single-curved optics, bent cylindrically to the Rowland circle. Modern applications typically use double-curved spherical crystals which offer improved efficiencies and energy resolutions. While Figure 2.1 shows explicitly a reflection (Bragg) geometry, the spectral focusing can also be achieved via transmission (Laue) through the optic. I will review each of these cases in Sections 2.2.2 and 2.2.3 respectively.

2.2.2 BRAGG GEOMETRIES

The simplest and most common realization of the Rowland circle in x-ray spectroscopy is the Johann geometry.[47] Here a flat Bragg analyzer is bent to twice the radius of the Rowland circle

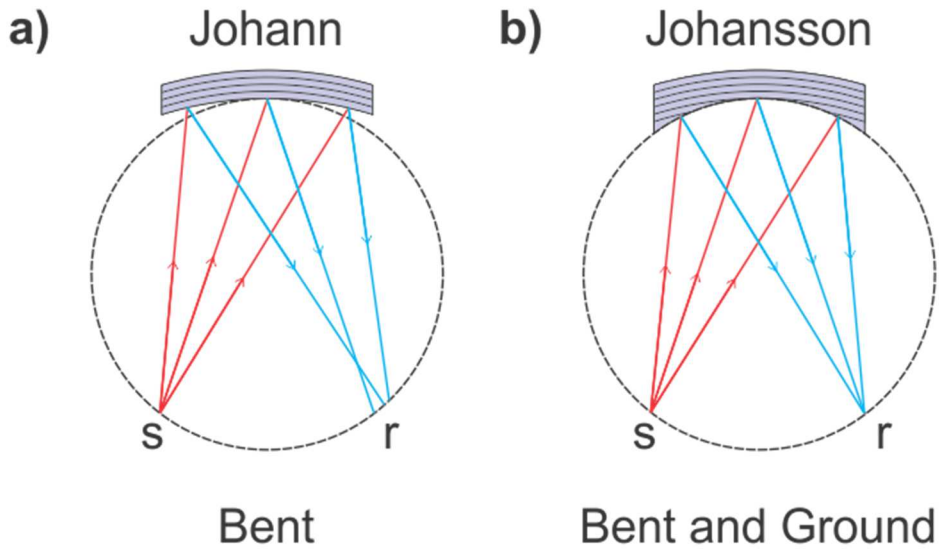

Figure 2.2. a) Johann implementation of the Rowland circle geometry. The analyzer is bent to twice the radius of the Rowland circle which causes refocusing errors at positon *r* (shown exaggerated for effect). b) Johansson geometry. The crystal is bent and then ground such that it is coincident to the Rowland circle at all points. In this case the refocusing is exact.

as shown in Figure 2.2a. Because only the center of the analyzer lays tangent to the Rowland circle, the focusing is inexact. The degree of deviation, known as the Johann error, is:

$$\Delta\theta \cong -\frac{1}{2}\left(\frac{\rho}{R}\right)^2 \cot\theta_B \qquad (2.4)$$

where $\Delta\theta$ is the angular aberration, ρ is the distance from the crystal center, and R is the optic radius of curvature.[52, 53] The geometrical error can be minimized by working with small crystals, such that$\left(\frac{\rho}{R}\right) \ll 1$, in near-backscatter configurations, such that $\cot\theta_B \ll 1$. Satisfying these constraints is not difficult. As close to backscatter geometries are commonplace in resonant inelastic x-ray scatter (RIXS) experiments where highest possible resolutions are required, there exists a veritable library of analyzers with suitably high Bragg angles for energies greater than ~4

keV. Furthermore, the small crystal size requirement can be alleviated by tiling multiple SBCAs to increase solid angle capture.

A modified version of this geometry was proposed and constructed by Johansson in 1933.[48] In this design the crystal is bent to twice the radius of the Rowland circle, as it is for the Johann geometry. The surface of the analyzer, however, is then ground such that each point is exactly on circle, see Figure 2.2b. As such the entire analyzer surface responds to the same Bragg angle, thus recovering exact focusing and removing the Johann error. Historically, Johansson's scheme has been less prevalent than Johann's due to the difficulty in maintain a pristine surface upon grinding. With present technology this is a much less salient problem and the Johansson geometry has become more common, especially in lower energy applications (> 4 keV) where crystals with working Bragg angles close to backscatter are rare. They are also employed in combined imaging and spectroscopic applications in laser shock studies.

2.2.3 LAUE GEOMETRIES

For very high x-ray energies (< 15-20 keV) where penetration lengths into crystals are large, Bragg reflection near backscatter with curved optics has low efficiency and large broadening. In this regime focusing is instead more easily achieved via Laue-type (transmission) geometries. In contrast to the Bragg geometries in Section 2.2.2, the diffraction here occurs along crystal planes perpendicular to the surface. Because the x-rays must transmit entirely through the analyzer crystal this technique is rarely employed at lower energies.

The quintessential focusing Laue design is the DuMond[50] spectrometer shown in Figure 2.3. The source, which is ideally very narrow in the in-plane direction, is placed on circle. In contrast

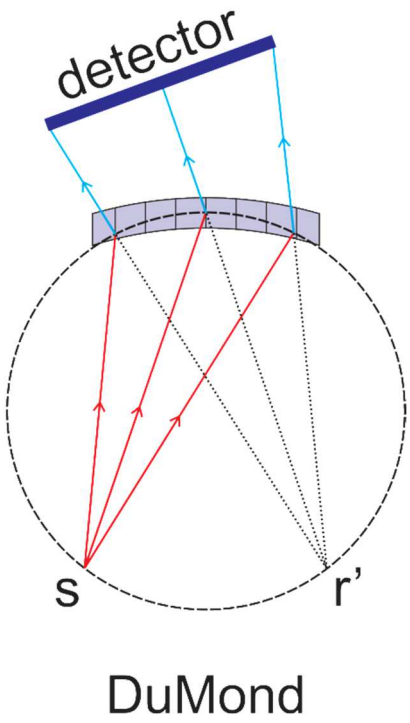

Figure 2.3. A DuMond-type focusing-Laue spectrometer. Radiation from the point source (s) is diffracted by transmission through the bent crystal. The rays diverge after diffraction creating an on-circle virtual image at r', the position of which is characteristic of x-ray energy. An extended detector captures the diffracted rays behind the Rowland circle.

to Bragg geometries the optic is oriented such that its center, rather than surface is tangent to the Rowland circle. The detector is placed off-circle behind the curved analyzer. Here the Laue geometry is not point-to-point focusing as it is for the Bragg-based implementations. Instead the crystal creates a virtual on-circle image position (r' in Figure 2.3) from which the diffracted rays appear to originate. As a result the detector must be large to capture the resulting monochromatic rays. The use of an extended detector can result in high backgrounds, as discussed in Section 2.1, and collimating Soller slits are often employed to boost the signal-to-noise ratio.

2.3 DISPERSIVE CRYSTAL SPECTROMETERS

2.3.1 VON HAMOS GEOMETRY

The von Hamos geometry[49] is a common dispersive method utilizing Bragg crystals coupled to position sensitive detectors. To increase efficiency the crystal is cylindrically bent which focuses along the curvature axis while still maintaining dispersion in the perpendicular plane. This is shown schematically in Figure 2.4. Each vertical slice of the curved analyzer corresponds to a constant Bragg angle, which in turn reflects x-rays to a unique line on the detector face. A spectrum is obtained by integrating counts on the detector along the focusing direction. As this is a fixed spectrometer, the energy bandwidth is set and depends on the width of the crystals as well its geometric position relative to the sample.

As is the case for spherically-bent analyzers in discussed in Section 2.2, several von Hamos optics can be tiled to increase the solid angle. Exact considerations for crystal size depend on required energy bandwidth, solid angle collection, and resolution and as such are experiment specific. The same is true of curvature; tighter curvature leads to increased efficiency, but at the cost of energy resolution and *vice-versa*. As for all Bragg-type analyzers, best energy resolution is obtained by working close to backscatter.

In applications where efficiency is prized over resolution the optic can be made from a mosaic crystal such as highly-oriented or highly-annealed pyrolytic graphite.[54, 55] Mosaic crystals are composed of a large number of small crystallites whose orientation randomly deviated from parallelness by a small amount. The mosaicity effectively broadens the optic rocking curve leading to higher integrated reflectivity.

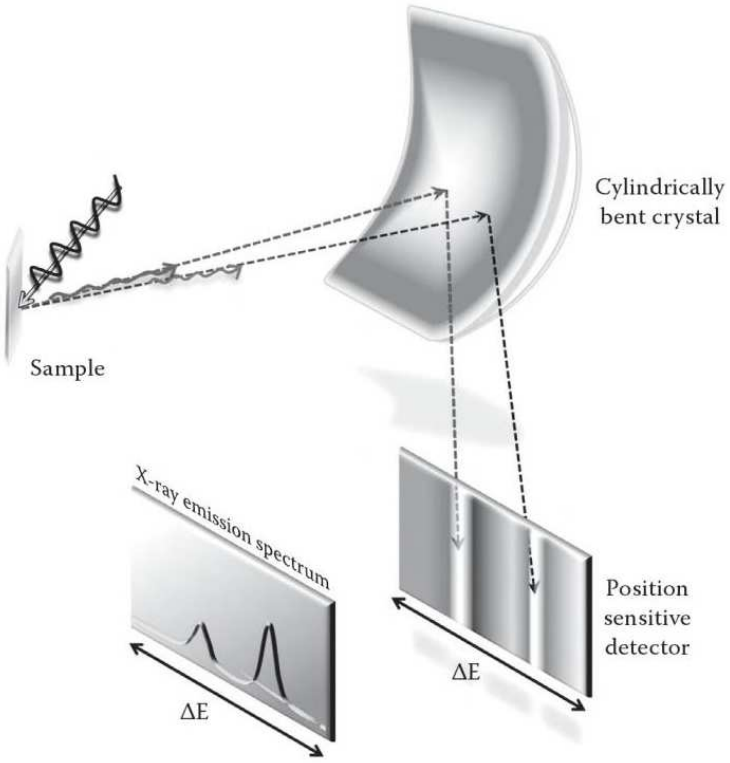

Figure 2.4. A von Hamos-type dispersive spectrometer. The curved optic is focusing along the cylindrical axis (vertical) and dispersive in the perpendicular plan. The reflected x-ray energy is therefore a function of horizontal position on the detector. Figure reproduced from J. C. Dousse and J. Hoszowska, in *High Resolution XAS/XES: Analyzing Electronic Structures of Catalysts*, edited by J. Sa (CRC Press, Boca Raton, 2015).[56]

2.3.2 OFF-CIRCLE BRAGG GEOMETRY

The Rowland circle geometry discussed in Section 2.2.1 can be made dispersive by working off circle. In this case, the spectrometer is operated in a non-scanning mode. By moving the diverging point-source inside the circle, as shown in Figure 2.5, each ray striking the analyzer appears to originate from a unique on-circle virtual source point. Each “virtual source point” is refocused

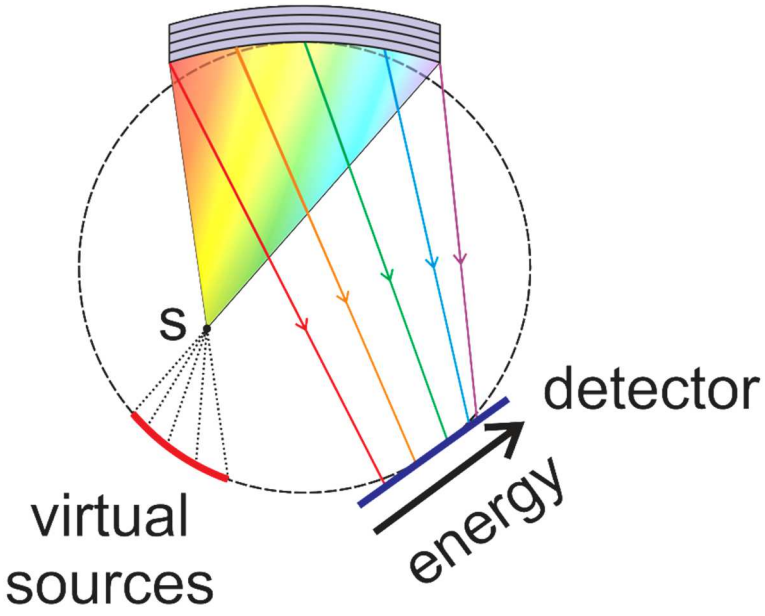

Figure 2.5. An off-circle Rowland geometry. Here the diverging point source (s) is moved inside the Rowland circle which creates an arc of virtual source locations on circle. Each of these virtual sources corresponds to a unique Bragg angle (energy) in the typical Rowland circle scheme. The refocused x-ray energy is therefore a function of lateral detector position.

according to the usual geometry discussed in Section 2.2.1. Since each corresponds to a different Bragg angle, x-ray energy becomes a function of lateral position on the detector face.

2.3.3 DISPERSIVE LAUE GEOMETRY

As is the case for the focusing Laue spectrometer, dispersive Laue methods are ideal for high x-ray energies (< 15-20 keV) where Bragg optics fail. The dispersive geometry, shown in Figure 2.6, was first achieved by Yvette Cauchois in 1932 and the geometry bears her name.[57] It is nearly identical to the DuMond design (see Section 2.2.3), but with the source and detector flipped. It should be noted that Cauchois proposed her geometry two years prior to DuMond.[50]

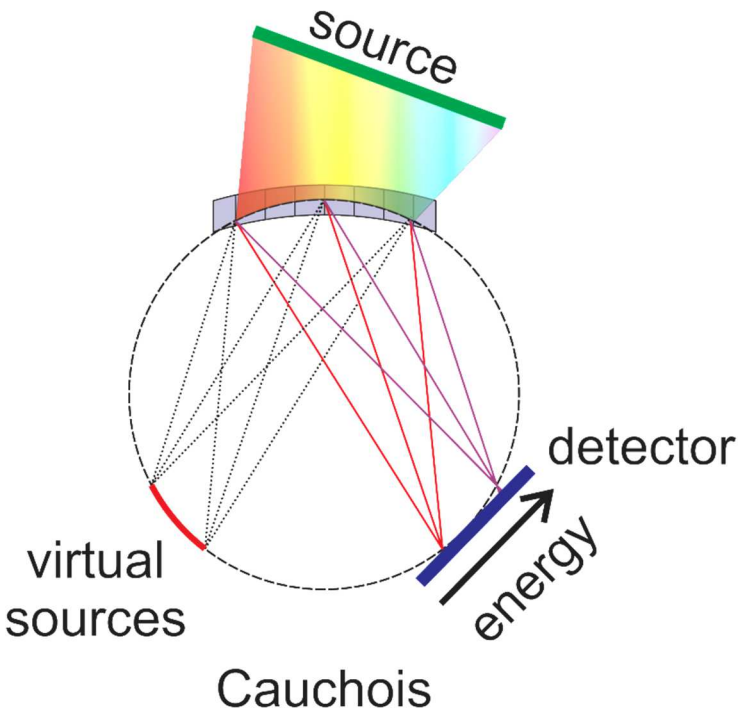

Figure 2.6. A Cauchois-type dispersive-Laue spectrometer. An extended source illuminates the curved optic from many angles of incidence, causing multiple energies to be focused simultaneously. X-ray energy is then a function of lateral position on a position-sensitive detector.

Here an extended source, such as a line focused source with the long direction in the Rowland plane, is positioned behind the Rowland circle. The curved crystal is illuminated from many angles, causing a wide range of energies to be focused on-circle simultaneously. A position-sensitive detector is then used to map spectrum energy. As with the von Hamos spectrometer, see Section 2.3.1, this is a line focusing geometry with dispersion in-plane. The focusing is inexact, suffering from the same aberrations as the Johann Bragg geometry (see Section 2.2.2).

2.4 SYNCHROTRON IMPLEMENTATIONS

X-ray beams generated from synchrotron radiation have very high initial collimation compared to conventional tube sources. As such, rapid energy tunability of the incident beam can be easily achieved via double flat-crystal monochromators.[58, 59] For experiments requiring monochromatization after scattering from the sample, such as x-ray emission and inelastic x-ray scattering spectroscopies, the curved geometries discussed above are often required. The remainder of this section reviews several synchrotron-based implementations of such spectrometers.

2.4.1 MULTI-ANALYZER ROWLAND SPECTROMETERS

The first synchrotron-based Johann-type Rowland spectrometer using an SBCA was built at the National Synchrotron Light Source in 1992.[60] Since then they have become increasingly common in synchrotron applications with several dedicated instruments now existing with multiple crystal analyzers.[16, 61-65] These multi-element systems are designed to increased solid angle collection for improved counting statistics and/or to simultaneous capture a range of momentum transfers for inelastic x-ray scattering studies.

As a representative example, I present a seven-crystal Johann spectrometer installed at the Stanford Synchrotron Radiation Lightsource.[64] Each analyzer exists on separate Rowland circles which are designed to overlap along the sample-detector axis as shown in Figure 2.7. All of the optics are mounted onto a common, translatable plate as well as their own linear stages. This motion is required to keep the circles overlapping when scanning Bragg angle. Here a single detector is used to record the analyzed signal from all crystals. In some applications it is

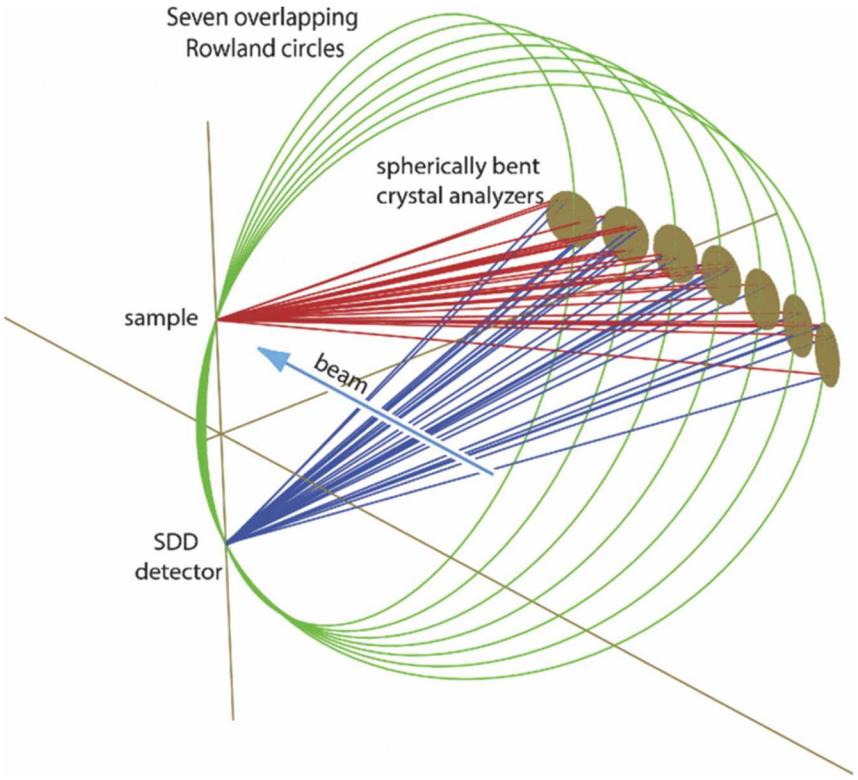

Figure 2.7. A seven-crystal Johann crystal spectrometer. Reproduced from D. Sokaras, T. C. Weng, D. Nordlund, R. Alonso-Mori, P. Velikov, D. Wenger, A. Garachtchenko, M. George, V. Borzenets, B. Johnson, T. Rabedeau and U. Bergmann, Review of Scientific Instruments 84 (5), 8 (2013).[64]

advantageous to separate the contribution from each crystal with either a positon sensitive or multiple detectors. In such cases the detector is backed off the intersection point.

The seven crystals combine to capture 0.45% of 4π steradian over a Bragg angle range of 74-88°. While the exact resolving power depends on the type of optic (conventional vs. diced), $E/\Delta E$ is typically on the order of 10^4. It has been found that resolution can be improved up to 20% by masking the outer edges of each optic, where the Johann error becomes more severe.[52, 53]

These characteristics provide excellent capability for a wide range of emission-based measurements. For example, the spectrometer can be held at a single energy where the narrow

bandwidth is ideal for high energy resolution fluorescence detection (HERFD) measurements. Or they can be used in a scanning mode such as is suitable in XES and RIXS. In either case the increased collection solid angle enables studies on dilute species or complex *in situ* samples.

2.4.2 A MINIATURE VON HAMOS SPECTROMETER

While Johann-type spectrometers in point-to-point focusing geometries are the most commonly employed at synchrotron light sources, growing interest in time-resolved or single-shot studies at synchrotron and x-ray free electron laser (XFEL) facilities has led to the development of a number of dispersive instruments.[66-68] Among the most popular are systems in the von Hamos geometry (see Section 2.3.1). In contrast to Johann-type spectrometers, which have working distances of ~1m or greater, these instruments can provide high resolution at much shorter working distances.

The most successful of these instruments is that of J. Hoszowska and collaborators at the University of Fribourg.[69] This spectrometer has been used in numerous studies with both synchrotron and laboratory sources. I will discuss this system in detail in Section 2.5.1. The collection efficiency of this design has been upgraded in recent years with the inclusion of strip-line crystals.[68]

Other examples of the von Hamos geometry include the miniature x-ray emission spectrometers (miniXES) developed at the University of Washington.[70, 71] In place of the single cylindrically bent crystal in the classic von Hamos geometry, these instruments utilize a series of small crystals as shown in Figure 2.8. When tiled together, they approximate the cylindrical surface. In this geometry each single crystal approximately satisfies its own Rowland circle, with dispersion shown in Figure 2.8a. Typical source-to-crystal distances are on the order of only ~50 mm. A 2-D position sensitive detector is placed off circle such that the analyzed signal from each

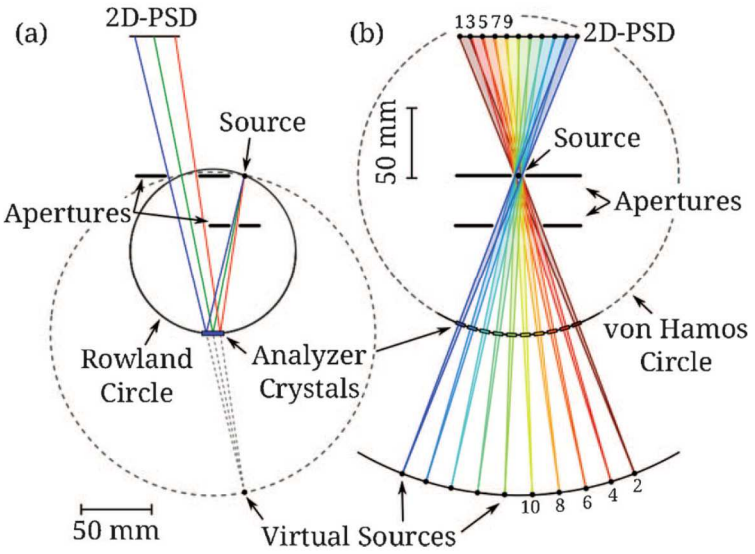

Figure 2.8. Geometrical ray tracing for a segmented von Hamos spectrometer. (a) Side view: of a single flat crystal; (b) Front view: tracing from all the analyzer crystals. Here the source-to-analyzer rays have been omitted for clarity. Reproduced from B. A. Mattern, G. T. Seidler, M. Haave, J. I. Pacold, R. A. Gordon, J. Planillo, J. Quintana and B. Rusthoven, Review of Scientific Instruments **83** (2), 023901 (2012).[70]

crystal illuminates a unique area (see Figure 2.8b). As with all dispersive geometries, energy becomes of function of position on the detector face. The energy conversion is determined practically by measuring a series of elastic scatter lines are measured across the instrument bandwidth.

2.5 LABORATORY IMPLEMENTATIONS

Laboratory-based instruments experienced their zenith in the earliest days of XAFS.[72-76] When synchrotron light houses emerged in the mid 1970's to early 1980's, however, they fell largely out of favor due to the inferior brilliance and tunability of x-ray tubes and, nontrivially, due to

the difficulty of acquiring high-quality optics and detector limitations in rejecting background and harmonics. Nonetheless, a small number of dedicated systems continued to be developed over the past thirty years.[77-85] As the supporting components, particularly crystal optics, solid-state energy dispersive detectors, and micro-focused tube sources, have continued to improve, the gap between laboratory and synchrotron is no longer quite so striking. The remainder of this section looks at several representative laboratory-based spectrometers from the past several decades.

2.5.1 A CONVENTIONAL VON HAMOS SPECTROMETER

In 1996, the Hoszowska group at the University of Fribourg developed a versatile von Hamos-type spectrometer (see Figure 2.9).[69] Free adjustment of the source-to-crystal and crystal-to-detector distances (being careful to keep the two equal) results in a tunable energy bandwidth adaptable for a broad range of studies. The curved cylindrical crystal and CCD detector sit on high-precision linear stages. The spectrometer covers a geometric range of 24.4-61.1° corresponding to 1.32-16.8 keV for a set of five crystals. Each of these crystals is cylindrically bent to a radius of 25.4 cm. To achieve useful counting rates at lower energies, the sample, crystal and detector are contained within a vacuum chamber. As a shared instrument between the University of Fribourg and the Paul Scherrer Institute, the intended excitation source is either a standard x-ray tube (photoionization) or charged particle beam (particle impact). It has also seen extensive use at synchrotron facilities.

The major limiting factor in instrument resolution is the extended source size. This can be partially recovered by restricting the emission via slits. The slits here are adjustable between 0.05-0.50 mm, allowing for some tuning in the resolution, with obvious trade-offs in counting

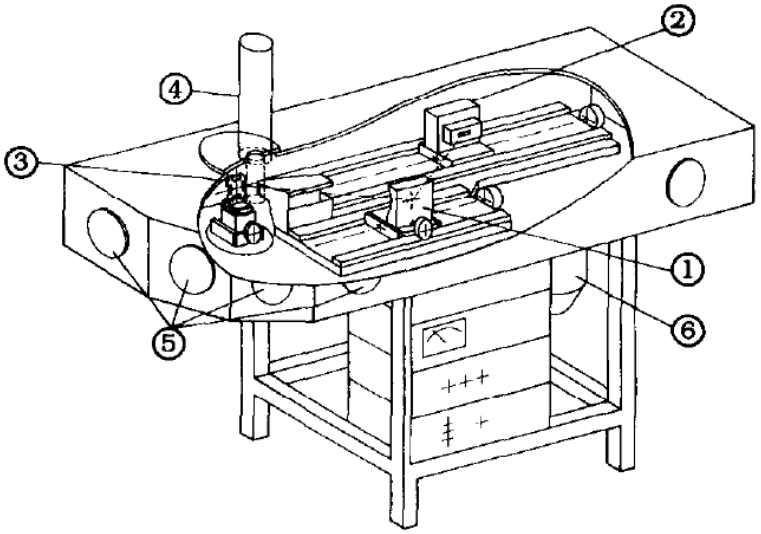

Figure 2.9. Rendering of a von Hamos x-ray crystal spectrometer: 1) cylindrically bent crystal, 2) position-sensitive CCD detector, 3) target barrel, 4) x-ray tube source, 5) beam ports and 6) vacuum pump. Reproduced from J. Hoszowska, J. C. Dousse, J. Kern and C. Rheme, Nuclear Instruments & Methods in Physics Research Section a-Accelerators Spectrometers Detectors and Associated Equipment 376 (1), 129-138 (1996).[69]

rate. Cu Kα XES was measured to evaluate instrumental resolution, yielding a range of 3.0-6.7 eV at 8048 eV emission energy.

While primarily developed to study x-ray emission, this spectrometer can also be used in XANES measurements. In this case a broad source, such as an x-ray tube, directly illuminates the crystal. As the von Hamos geometry is dispersive, sample inhomogeneity becomes a major source of systematic error.

2.5.2 A NOVEL VON HAMOS SPECTROMETER

More recently, a group from the Technical University of Berlin presented a laboratory spectrometer based on a novel application of the von Hamos geometry.[86] In contrast to the

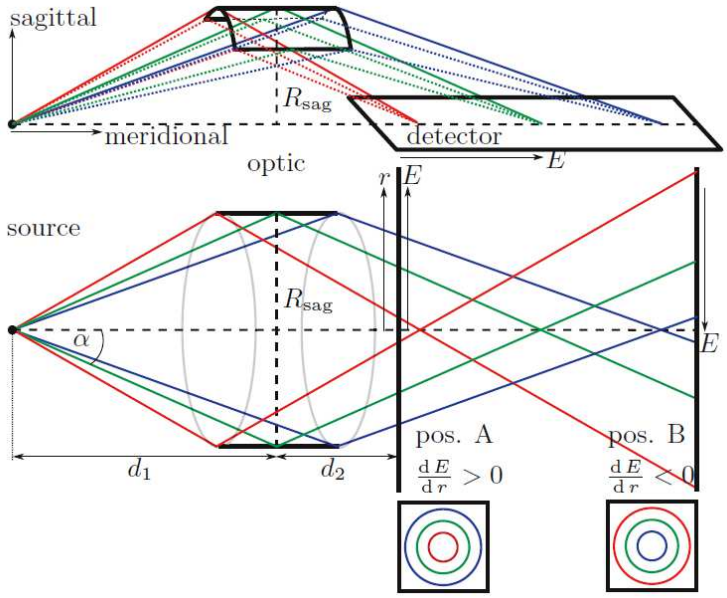

Figure 2.10. (Top) the classical von Hamos geometry in which the position sensitive detector is oriented along the cylindrical axis of the bent optic. (Bottom) A novel, full-cylinder geometry which places the detector face perpendicular to the crystal bend axis. Reproduced from L. Anklamm, C. Schlesiger, W. Malzer, D. Grotzsch, M. Neitzel and B. Kanngiesser, Review of Scientific Instruments **85** (5), 053110 (2014).[86]

classical design (see Section 2.3.1), here the position sensitive detector is oriented perpendicular to the bend axis of the cylindrical crystal optic. This adjustment causes a mapping of circles of constant x-ray energy on the detector face as shown in Figure 2.10. The major result of this geometry is that for certain placements of the detector relative to the source and optic, the radius of each circle will be unique to a single energy, allowing for resolution of the full energy bandwidth.

The advantage of this design is its compatibility large (i.e., full cylinder) dispersive optics, with obvious gains to captured solid angle. As perfect crystals experience larges strains when bent to

such a degree, this application utilizes highly annealed pyrolytic graphite (HAPG) sheets. HAPG is a mosaic crystal composed of small, perfect crystallites and thus is much more flexible to tight bends than single, perfect crystals such as Ge and Si. Additionally, the mosaicity results in improved integral reflectivity (albeit at a small cost to energy resolution). Using a 30 mm HAPG crystal bent to 150 mm radius of curvature, the researchers were able to capture on the order of 1 msr.

The exact details of the spectrometer are as follows. The radiation source is a commercial, 100-W micro-focus (~50 μm) x-ray tube. As this instrument is used for XES studies the tube output is refocused onto the sample using a polycapillary full-lens. More details on polycapillary optics can be found in Chapter 8. The HAPG optic and CCD detector are placed in a vacuum chamber allowing operations at low energies. The energy range is adjustable from 2.5-15 keV. The resolving power, as estimate by the FWHM of Cu Kα emission, was determined to be $E/\Delta E =$ 2000 at 8 keV.

2.5.3 A DuMond-type Laue spectrometer

Also coming out of the University of Fribourg is a focusing crystal spectrometer based on the DuMond geometry discussed in Section 2.2.3.[87] This instrument, shown schematically in Figure 2.11, was developed for x-ray emission spectra above 10 keV. In this so-called "modified" DuMond geometry, a narrow slit (extended in the out-of-plane direction) is placed directly on circle with the target moved behind. With the slit on-circle resolution can be tuned by adjusting width as was the case for the von Hamos spectrometer in Section 2.5.1. Furthermore, this procedure prevents systematic changes in spectral line shape due to thermal deformation of the target.

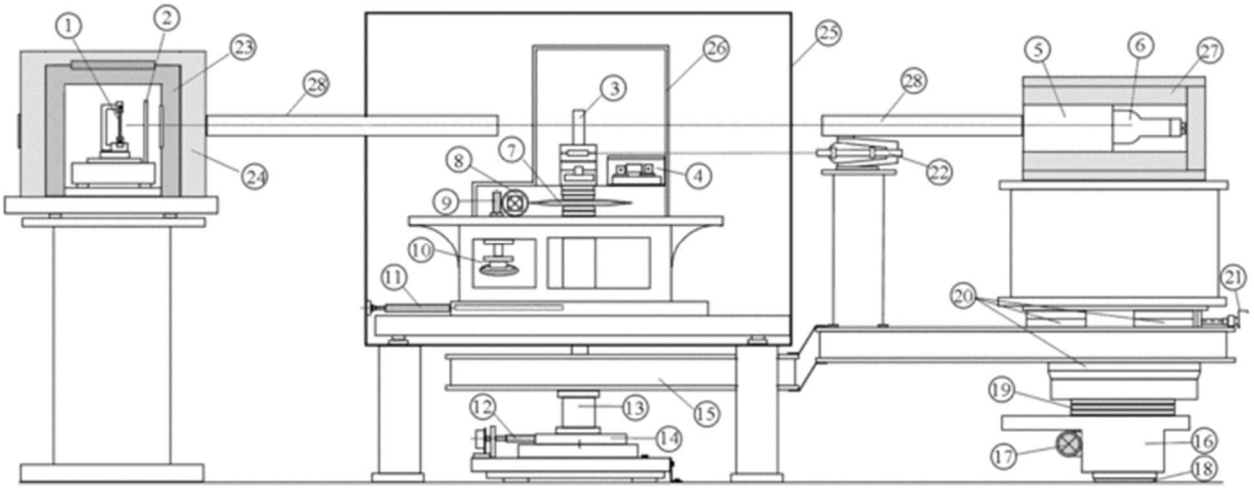

Figure 2.11. Side view of the modified-DuMond crystal spectrometer. The key components are: (1) target, (2) slit, (3) crystal, (4) optical laser interferometer, (5) Soller slit-collimator, (6) detector. A full description of all numbered parts can be found in the cited text. Reproduced from M. Szlachetko, M. Berset, J. C. Dousse, J. Hoszowska and J. Szlachetko, Review of Scientific Instruments 84 (9), 093104 (2013).[87]

As the source/target is held stationary the crystal and detector sit on θ and 2θ stages respectively to keep the components on the Rowland circle. Additionally the slit-to-crystal distance is motorized to keep on the focal circle. The Bragg angle is measured via optical laser interferometry with precision of several milli-arcsec. Quartz, silicon, or germanium single crystals are elastically deformed using a custom bending device. The resultant cylindrical bend is typically 315 cm in radius. A scintillation detector is equipped with collimating Soller slits to block the direct beam at small Bragg angles.

As before, instrumental resolution is determined primarily by the slit size and precision of crystal curvature. For a slit width of 0.10 mm a resolution of 2.8 eV was obtained for Mo $K\alpha_1$ emission (17.48 keV), which is well below the intrinsically core-hole limited resolution of 4.52 eV. At higher energies the bandwidth goes as E^2, increasing to 17.1 eV at Gd $K\alpha_1$ (42.99 keV).

As is the case with most focusing spectrometers, this instrument offers exceptional signal-to-background. As a fine test of performance the investigators measure the nominally dipole-forbidden $K\alpha_3$ peak in Gd. Despite falling on the tail of the $K\alpha_2$ line, which is more intense by $\sim 10^4$, they were able to clearly resolve the feature with an energy consistent with theory and previous experiment.

2.5.4 A DISPERSIVE LAUE EXAFS SPECTROMETER

For x-ray absorption measurements, it is possible to circumvent the issue of sample inhomogeneity discussed in Section 2.3.1 by instead dispersing via transmission through the crystal optic. An example of this method is shown in Figure 2.12.[85] Here Bragg diffraction occurs on lattice planes perpendicular to a thin crystal, causing the beam to refocus at a spot symmetrically opposite the point source.[83, 88] As the crystal is flat, each location corresponds to a different Bragg angle and therefore energy. The sample is placed at this convergence point ensuring that the same volume is probed regardless of incident energy. After transmission through the sample each ray diverges until hitting the face of a position sensitive detector. This location is uniquely determined by the diffraction angle and is therefore a function of x-ray energy.

The bandwidth of dispersed energies is tuned by varying the relative geometry between source and crystal. Note that both must be rotated in order to steer the diffracted radiation back onto the detector. The initial divergence is controlled by both Soller and horizontal slits. The detector sits on a linear translation stage allowing for tradeoff between solid-angle and resolution depending on the application.

While the spectrometer resolution (4.6 eV at 8980 eV) is too poor to resolve features in the XANES region, it performs well for EXAFS where the features are broad. The investigators

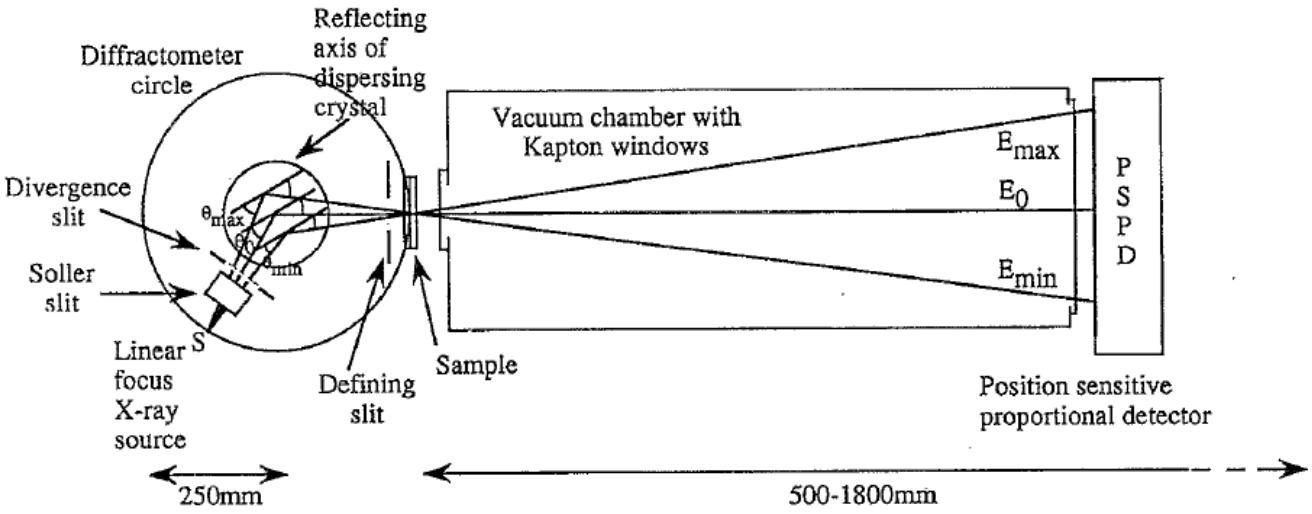

Figure 2.12. A transmission-mode laboratory EXAFS spectrometer based on a dispersive-Laue geometry. The x-ray source (S) illuminates a thin crystal which diffracts only a controlled range of x-ray energies. The diffracted beams refocus at the sample location before dispersing onto the position sensitive proportional detector (PSPD). Reproduced from P. Lecante, J. Jaud, A. Mosset, J. Galy and A. Burian, Review of Scientific Instruments 65 (4), 845-849 (1994).[85]

found excellent agreement with synchrotron data for a number of concentrated Cu and Zr samples, albeit at measurements times of ~24 hours. It was found that the limited flux of the x-ray tube necessitated that samples be kept to near a single penetration length to optimize signal. This constraint is not unique and is common to many laboratory-based x-ray absorption spectrometers.

Chapter 3. VALENCE-TO-CORE X-RAY EMISSION SPECTROSCOPY

In this chapter, I expound upon the subject of valence-to-core (VTC) emission spectroscopy discussed briefly in Section 1.4.3. I begin in Section 3.1 with an overview of the origins of various lines composing the VTC region and describe their chemical sensitivities. In Section 3.2, I present recent, representative studies in which VTC-XES was successfully employed to resolve lingering chemical questions. In Section 3.3, I detail the underlying theory of VTC emission and outline various computational models.

3.1 BACKGROUND

While valence-to-core (VTC) are the weakest of all emission lines, they are also the most sensitive to local chemical environment. VTC fluorescence arises from transitions from filled electronic states a few eV below the Fermi level to vacant core-levels (see Figure 1.2), thus providing a direct probe of valence electronic structure. In contrast to other analytical chemical methods (e.g., x-ray photoemission spectroscopy, nuclear magnetic resonance, Raman spectroscopy, *etc*.) hard x-ray VTC-XES is effective in complex sample environments and systems lacking long-range order or simple unit cells. In particular, VTC-XES is prized for its ability to interrogate ligands. In no small part due to these advantages, VTC-XES has in recent years received considerable attention as regards ligand chemistry in catalysis, bioscience, and environmental science (see Section 3.2).

The exact lines constituting VTC emission depend strongly on the species of the interrogated atom. In principle, an atom can have multiple classes of VTC emission corresponding to the subshell of the intermediate core-hole (K, L, etc.). For consistency and brevity, I will discuss

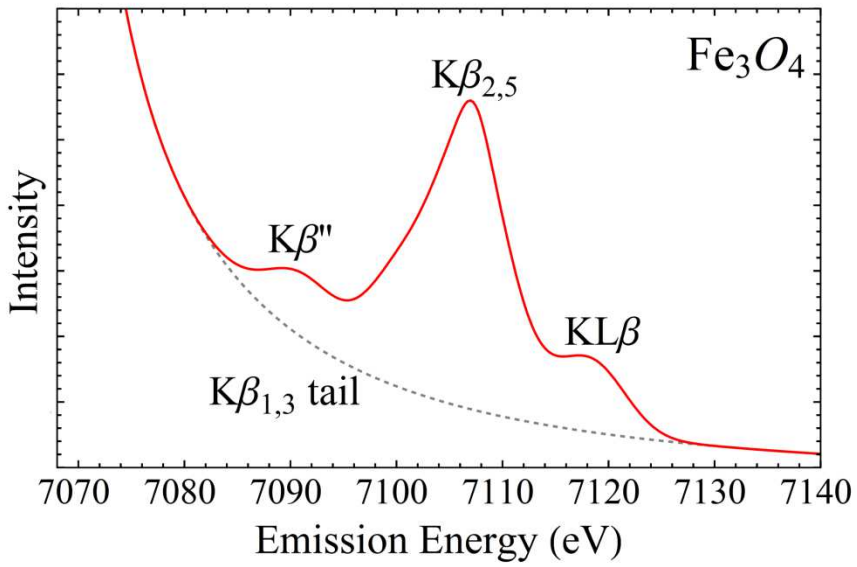

Figure 3.1. Fe K-shell valence-to-core emission in Fe_3O_4. The three major valence features are: $K\beta_{2,5}$ (ligand and metal *p* character to metal 1s), Kβ″ (ligand *s* to metal 1s) and KLβ (multi-excitation). These peaks typically sit atop the high-energy tail of the main $K\beta_{1,3}$ line (dashed-gray line).

only the most energetic VTC lines (i.e., valence to 1s transitions) of 3d-transition metal complexes. Details and applications on other systems, such as lanthanides, can be found elsewhere.[89-94]

The main features of the VTC region are summarized in Figure 3.1. The strongest valence line is the $K\beta_{2,5}$ which originates from valence orbitals with metal 4p character. There is also contribution from the dipole forbidden (in the centro-symmetric case) 3d-1s transitions,[29] the intensity of which scales with Z.[30] The location of the $K\beta_{2,5}$ peak changes with electronic screening and is therefore highly correlated to metal-oxidation state. At lower energies is the Kβ″, or cross-over peak, which is absent in pure metal samples. This feature is commonly contributed to transitions from ligand s orbitals;[37] however, recent results suggest it is instead

due to metal np → metal 1s transitions where the metal valence orbitals mix strongly with ligand 2s states.[40] In either case, the energy of emission depends on the ligand 2s binding energy[25, 39] which makes it an excellent fingerprint for ligand speciation and environment.[31, 33-37] In particular the Kβ″ is better at distinguishing ligands than EXAFS (see Chapter 1). Additionally, the integrated Kβ″ intensity relative to Kβ varies exponentially with metal-ligand distance yielding bond lengths accurate to within 0.1 Å.[31, 32, 38, 40]

Above the Fermi level is the so-called KLβ peak. This nomenclature arises from the assignment to a multi-electron excitation which can occur when the incident x-ray energy is above the K + L-edge binding energies.[95, 96] The exact mechanism for this type of event is not well understood especially as regards the timing of the hole creation (i.e., double photoionization vs. single ionization and subsequent shake effects). In some systems there are additional multiple-excitation features above the Fermi level corresponding to [1s2p], [1s3p], [1s3d], *etc*.[97, 98]

3.2 Recent applications

3.2.1 Catalysis

Catalysis is a broad chemical subject applicable to fields ranging from industrial to biological processes. In each of these applications, a keen understanding of the changing electronic landscape surrounding active reaction sites is of utmost importance. A number of analytic techniques are commonly employed in catalytic systems aimed at probing the geometric and valence electronic structure of active sites.[99-105] Among these, VTC-XES is emerging as an effective tool due to its ability to probe ligand species and its hard x-ray compatibility with *in situ* and *operando* conditions. Notably the ability of the Kβ″ feature to distinguish ligand

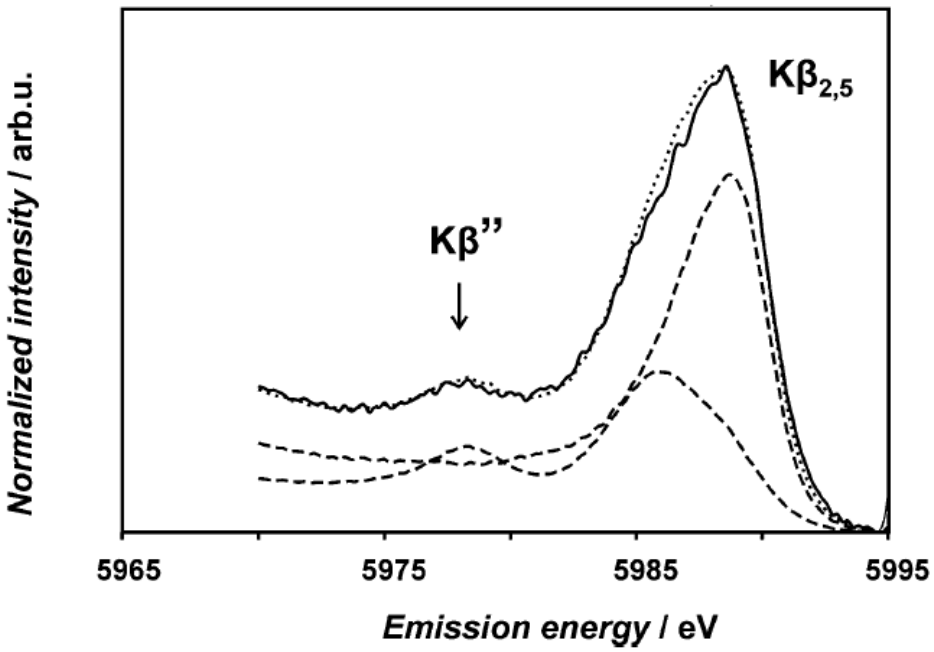

Figure 3.2. Valence-to-core emission of a Cr nanocrystal synthesized electrochemically from a solution containing formic acid additives (solid line). Shown is a fit (dotted line) from a linear combination of Cr metal and Cr_3C_2 reference standards (dashed lines). Reproduced from V. A. Safonov, *et al.*, Journal of Physical Chemistry B **110** (46), 23192-23196 (2006).[34]

species, ionization and protonation state and to do so element-specifically has proven to be of major benefit.[28, 33, 35, 106-110]

The first application of VTC-XES to a working (non-model) system concerned identifying Cr-bonding resulting in electrodeposited coatings.[34] Such coatings are common in manufacturing as a means to improve hardness and corrosion-resistance. Here V. Safonov, *et al.* investigated the composition of Cr deposits synthesized using organic additives (formic and oxalic acid). By utilizing a simple linear combination fit of the experimental data to several reference standards (see Figure 3.2) the investigators were able to determine the existence of Cr-Cr and and Cr-C

bonding with Cr-N and Cr-O being noticeably absent. These results helped shape understanding of the chemical processes driving deposition.

As a biological example, VTC-XES has famously been used to the study of oxygen or nitrogen ligation in the Mn_4Ca cluster of Photosystem II (PS-II). This protein, which is critical to photosynthesis, has been extensively studied via a number of optical and x-ray spectroscopies aimed at understanding metal-ligand interactions.[21, 22, 33, 111-115] In 2010, VTC-XES joined this long list of analytical tools as a means to directly probe the ligand chemistry.[116] Here Y. Pushkar, *et al.* examined the oxo bridging ligands of the Mn_4Ca complex which catalyzes water-oxidation. The important chemistry in this reaction hinges on the ligand O bonding with respect to the Mn metal-center. In particular bridging oxo groups have been suggested to be a mechanism for the formation of O-O during the oxidation reaction.[117]

As demonstrated above, this information can be accessed via Kβ″ emission. The weak intensity of VTC and the low Mn concentration in PS-II, however, makes this a difficult experiment in practice and was only achievable using high-brilliance synchrotron radiation coupled with a 14-analyzer spectrometer to increase solid angle capture (see Section 2.4.1). The results, shown in Figure 3.3, compare the PS-II protein to a number of oxo-bridged Mn-coordinated complexes. The relative sharpness and intensity of the PS-II Kβ″ as compared to the other samples is suggestive of several oxo bridged Mn-O in the S_1 state.

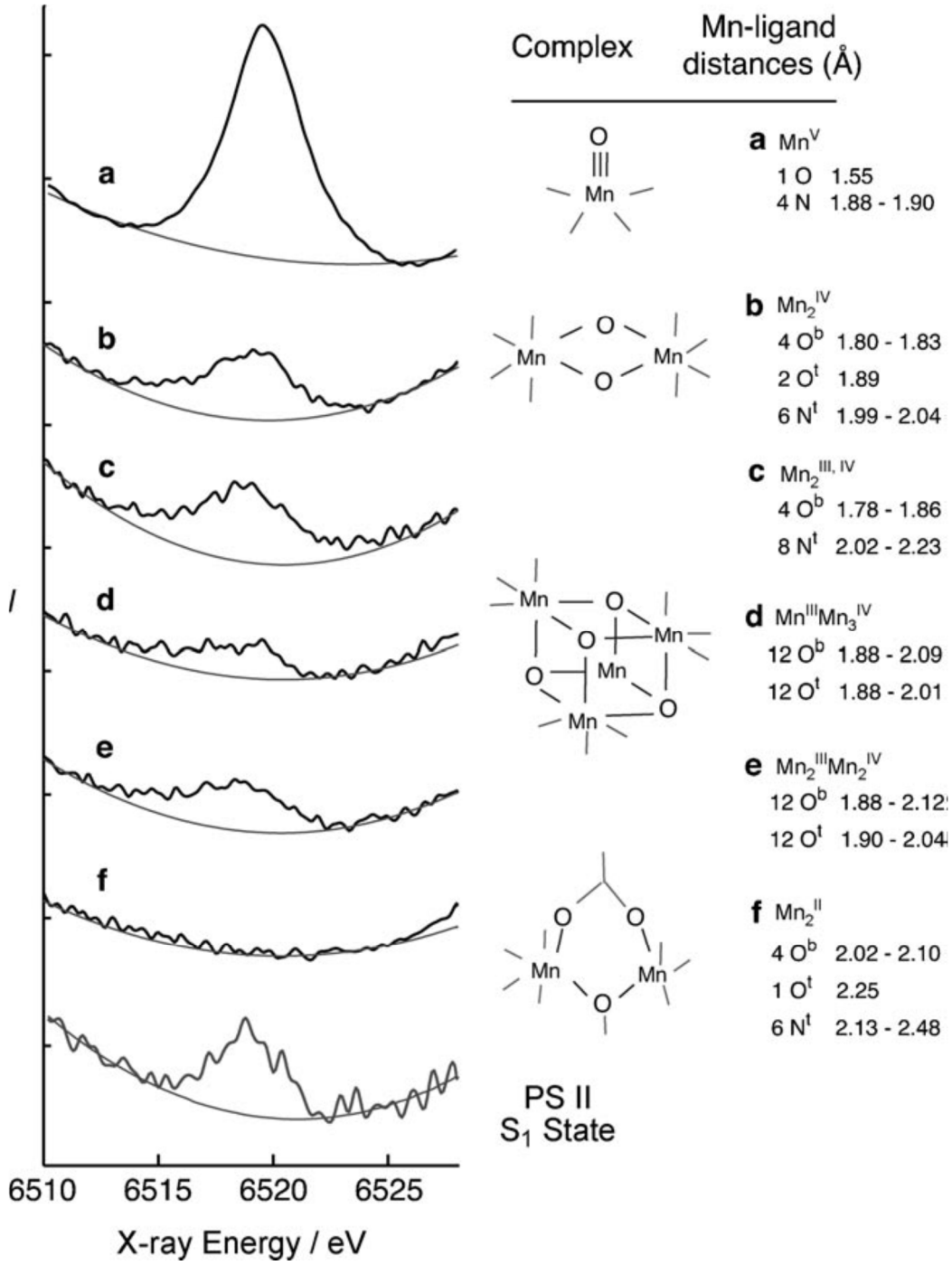

Figure 3.3. Mn Kβ″ emission from the PS-II protein in the S_1 state (bottom curve) compared to that of: a) Mn^{V} oxo; b) di-μ-oxo bridged $Mn_2^{III,IV}$; c) di-μ-oxo bridged Mn_2^{IV}; d) cubane-type $Mn_2^{III}Mn_2^{IV}$; e) cubane-type $Mn^{III}Mn_3^{IV}$; f) μ-alkoxide bridged Mn_2^{II}. Reproduced from Y. Pushkar, *et al.*, Angewandte Chemie-International Edition 49 (4), 800-803 (2010).[116]

3.2.2 ENVIRONMENTAL SCIENCE

Soil and water contamination is a subject of high environmental and social concern especially in urban areas where close proximity raises serious potential health hazards to a large population. Anthropogenic contaminants, arising largely from industrial and agricultural activities, are typically based in transition- and heavy-metal compounds. Investigation and remediation of soil hinges on identifying not just the presence, but the chemical state of these metal complexes in order to understand solubility and mobility. As the Kβ″ peak is strongly indexed to transition-metal coordination chemistry, VTC-XES is a prime candidate for addressing these questions.

As an example, we can consider Cr toxicity. Naturally occurring Cr exists primarily in the trivalent (Cr(III)) state and is safe and essential to human life. Hexavalent (Cr(VI)) compounds, however, are predominantly anthropogenic and highly toxic.[118-120] The ability to discern Cr valency, of which VTC-XES is uniquely suited to probe, is therefore of paramount importance to public safety.

In a 2008 study, S. Eeckhout, *et al.* used Kβ-VTC to examine Cr chemistry in a soil sample from Torino, Italy.[37] The elevated presence of Cr in the local environment was previously determined and had been attributed to sedimentary deposit from local rivers (Torino itself being located on an alluvial plain) based on geographical distributions.[121-123] Cr from this type of natural origin was suggested to be from serpentine minerals and chromite clay, both of which have Cr-O bonds.

To test this theory, S. Eeckhout, *et al.* carefully measured Cr VTC on a representative Torino soil sample and compared it to several reference materials. The results, reproduced in Figure 3.4, demonstrate that the VTC, in particular the Kβ″ cross-over peak, is inconsistent with Cr-O association. Instead the results are indicative of Cr bonding with P and/or C, with perhaps some

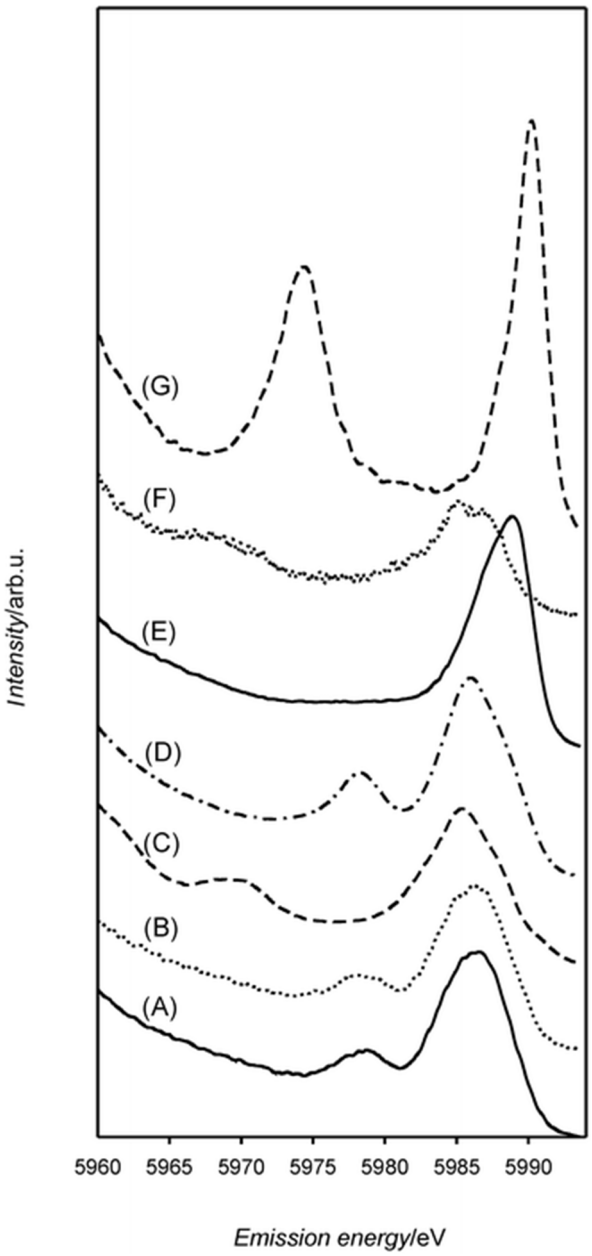

Figure 3.4. Cr valence-to-core emission for: (A) a Torino soil sample; (B) CrP; (C) Cr_2O_3; (D) Cr_3C_2; (E) Cr metal; (F) $FeCr_2O_4$; and (G) $K_2Cr_2O_7$. The location of the Kβ″ cross-over peak in the soil sample is inconsistent with Cr-O bonding and instead suggests the Cr in soil is associated with Cr, P, and/or C. Reproduced from S. G. Eeckhout, *et al.*, Journal of Analytical Atomic Spectrometry 24 (2), 215-223 (2009).[37]

contribution from pure metallic Cr. While this type of Cr chemistry is very unusual in nature, it is consistent with the local steel production in which C and P compounds are common. It is therefore suggestive that the Cr is due to human rather than natural activities.

3.3 THEORY

X-ray emission is an inherently many-body problem of coupling between a photon and a system of electrons. The effect of these interactions can be described via quantum mechanical perturbation theory. As emission follows the creation of a deep core-hole, the intermediate states are of intrinsic importance and the perturbation must be carried out to second order. This term, designated the Kramers-Heisenberg formula, gives the emission intensity I as:

$$I(\Omega,\omega) \propto \sum_{|f\rangle} \left| \sum_{|n\rangle} \frac{\langle f|T_2|n\rangle\langle n|T_1|g\rangle}{E_g - E_n + \hbar\Omega - i\Gamma_n} \right|^2 \times \delta\left(E_g + \hbar\Omega - E_f - \hbar\omega\right) \qquad (3.1)$$

where $\hbar\Omega$ is the energy of the incident photon, $\hbar\omega$ is the energy of the emitted photon, $|g\rangle$, $|n\rangle$ and $|f\rangle$ are the ground, intermediate and final states respectively with energies E_g, E_n and E_f, T is the relevant transition operator ($T_1 = T_2$ for photoexcitation) and Γ_n is the core-hole broadening of the intermediate state. The delta function ensures conservation of energy. The full derivation of this term, which originates from the vector potential of the quantized electromagnetic field, can be found in any number of advanced quantum mechanics textbooks.[124-126]

For practical purposes, equation (3.1) is simplified by several key approximations. First, to accommodate for the finite lifetime broadening of the final state, the delta function is replaced by a Lorentzian with full width at half maximum equal to Γ_f:

$$\delta\left(E_g + \hbar\Omega - E_f - \omega\right) \rightarrow \frac{\Gamma_f/2\pi}{\left(E_g + \hbar\Omega - E_f - \hbar\omega\right)^2 + \Gamma_f^2/4} \qquad (3.2)$$

Secondly, in the case of non-resonant XES where the photoelectron does not interact with the resulting ion, its wavefunction can be treated independently. The intermediate and final states then become:

$$|n\rangle = |\phi_\varepsilon\rangle|n'\rangle, \quad E_n = E_{n'} + \varepsilon \tag{3.3}$$

$$|f\rangle = |\phi_\varepsilon\rangle|f'\rangle, \quad E_f = E_{f'} + \varepsilon \tag{3.4}$$

where $|\phi_\varepsilon\rangle$ is the wavefunction of the photoelectron with energy ε, and $|n'\rangle$ and $|f'\rangle$ are respectively the intermediate and final states of the ion.

Substituting these approximations into equation (3.1) and integrating over the photoelectron density of states yields:

$$I(\Omega,\omega) \propto \sum_{|f'\rangle} \left| \sum_{|n'\rangle} \frac{\langle f'|T_2|n'\rangle\langle n'|a_c|g\rangle}{E_g - E_{n'} - \hbar\omega - i\Gamma_{n'}} \right|^2 \times L(\Gamma_n, \Gamma_f) \tag{3.5}$$

where a_c is the annihilation operator of the core electron and $L(\Gamma_n, \Gamma_f)$ is a Lorentzian convolution of intermediate and final state core-hole lifetimes.[127] The key result here is that equation (3.5) has removed all dependence of the spectral shape on the incident photon energy Ω. This approximation holds so long as the same intermediate states are achieved.[4, 127]

The application of equation (3.5) requires knowledge of the ground, intermediate and final wavefunctions in order to evaluate the transition matrix elements. The different theoretical approaches to modeling XES are therefore distinguished according to their method for calculating these states. These methods fall predominantly into two categories: ligand field multiplet theory (LMFT) and density functional theory (DFT). In simplest terms, the former is a semi-empirical, many-body atomic picture and the latter an *ab initio*, single-particle extended approach.

I will not discuss LMFT here other than to say that while it yields excellent results for core-to-core spectra, it is typically more problematic for VTC where the absence of a deep core-hole in the final state diminishes the importance of multiplet splitting. In these instances, DFT-based approaches have proven to be much more highly effective. More comprehensive reviews of LMFT can be found elsewhere.[128, 129]

In DFT, electronic structure is cast in terms of the ground state electronic charge density, $\rho(\boldsymbol{r})$. This method has a long history in condensed matter, the first such model being introduced in 1927 by Thomas and Fermi.[130, 131] Modern DFT can trace its roots to the framework established by the two Hohenberg-Kohn theorems; the first stating that all ground state properties are uniquely determined by $\rho(\boldsymbol{r})$ and the second demonstrating that the ground state energy expressed as a functional of $\rho(\boldsymbol{r})$ is minimized by the physically true ground state density.[132] In this formalism the total energy, E, of the absorbing atom is expressed as:

$$E[\rho(\boldsymbol{r})] = T[\rho(\boldsymbol{r})] + \int V_{ext}(\boldsymbol{r})\rho(\boldsymbol{r})d^3\boldsymbol{r} + \frac{1}{2}\int \frac{\rho(\boldsymbol{r})\rho(\boldsymbol{r}')}{|\boldsymbol{r}-\boldsymbol{r}'|} d^3\boldsymbol{r}d^3\boldsymbol{r}' + E_{xc}[\rho(\boldsymbol{r})] \quad (3.6)$$

This expression can be considered in parts. The first term, $T[\rho(\boldsymbol{r})]$, is the kinetic energy of a non-interacting electron system. Next is the potential energy originating from nuclear-electron attraction and nuclei-pair repulsion, $V_{ext}(\boldsymbol{r})$. Third is the so-called "classical" term which is the electron-electron potential absent any exchange or correlation effects. Lastly is the exchange-correlation term, $E_{xc}[\rho(\boldsymbol{r})]$, which simply put contains the remaining physics not captured by the previous terms. As the exchange-correlation term does not have a neat, closed form it is the main source of error in computation and is a topic of continuing research. The accuracy of DFT-based calculations all hinge on how well this term is modeled with different approximations forming the major distinction between various methods as will be discussed below.

Minimizing the functional in equation (3.6) leads to the Kohn-Sham equations:

$$\left(-\frac{1}{2}\nabla^2 + V_{KS}\right)\phi_i = \varepsilon_i\phi_i \tag{3.7}$$

$$V_{KS}(\boldsymbol{r}) = V_{ext}(\boldsymbol{r}) + \int \frac{\rho(\boldsymbol{r\prime})}{|\boldsymbol{r}-\boldsymbol{r\prime}|} d^3\boldsymbol{r}' + \frac{\boldsymbol{\delta}E_{xc}[\rho(\boldsymbol{r})]}{\boldsymbol{\delta}\rho(\boldsymbol{r})} \tag{3.8}$$

which are noninteracting, single-particle Schrödinger equations in a potential V_{KS}. It should be noted that the Kohn-Sham orbitals, ϕ_i, are not wavefunctions of the true system. They are meant only to serve as a reference-model which combine to form the correct ground state density:

$$\rho(\boldsymbol{r}) = \sum_i |\phi_i|^2 \tag{3.9}$$

It is important to note that the equivalence to the true, interacting system is often only in the region outside the ion-cores, especially when pseudo-potentials are employed. Once $\rho(\boldsymbol{r})$ is calculated the true ground state wavefunctions can be determined according to the first Hohenberg-Kohn theorem.

In addition to modeling of the exchange-correlation term, DFT methods can be further distinguished by their method of solving the Kohn-Sham equations. This can be done via a real space method over a cluster of atoms surrounding the absorbing site or in reciprocal space using periodic boundary conditions. Presently there exist a number of DFT-based electronic structure codes including: Quantum ESPRESSO,[133] GPAW,[134] ABINIT,[135-137] VASP[138] (projector augmented wave); WIENK2K[139, 140] (full-potential augmented plane waves); FEFF9,[141, 142] FDMNES[143], MXAN[144, 145] (multiple scattering); ORCA[146] and NWChem[147] (time-dependent DFT).

Chapter 4. A LABORATORY-BASED HARD X-RAY MONOCHROMATOR FOR HIGH-RESOLUTION X-RAY EMISSION SPECTROSCOPY AND X-RAY ABSORPTION NEAR EDGE STRUCTURE

Originally published as: G. T. Seidler, D. R. Mortensen, A. J. Remesnik, J. I. Pacold, N. A. Ball, N. Barry, M. Styczinski and O. R. Hoidn, Review of Scientific Instruments **85** (11), 12 (2014).

We report the development of a laboratory-based Rowland-circle monochromator that incorporates a low power x-ray (bremsstrahlung) tube source, a spherically-bent crystal analyzer (SBCA), and an energy-resolving solid-state detector. This relatively inexpensive, introductory level instrument achieves 1-eV energy resolution for photon energies of ~5 keV to ~10 keV while also demonstrating a net efficiency previously seen only in laboratory monochromators having much coarser energy resolution. Despite the use of only a compact, air-cooled 10 W x-ray tube, we find count rates for nonresonant x-ray emission spectroscopy (XES) comparable to those achieved at monochromatized spectroscopy beamlines at synchrotron light sources. For x-ray absorption near edge structure (XANES), the monochromatized flux is small (due to the use of a low-powered x-ray generator) but still useful for routine transmission-mode studies of concentrated samples. These results indicate that upgrading to a standard commercial high-power line-focused x-ray tube or rotating anode x-ray generator would result in monochromatized fluxes of order $10^6 – 10^7$ photons/s with no loss in energy resolution. This work establishes core technical capabilities for a rejuvenation of laboratory-based hard x-ray spectroscopies that could have special relevance for contemporary research

on catalytic or electrical energy storage systems using transition-metal, lanthanide or noble-metal active species.

4.1 INTRODUCTION

X-ray absorption fine structure (XAFS) spectroscopy[127, 148, 149] and related techniques, such as high-resolution x-ray emission spectroscopy (XES) and non-resonant and resonant inelastic x-ray scattering,[16, 125, 127] have an established and growing importance across multiple fields of science. Historically, these methods both helped motivate and also immensely benefitted from the progressive development of synchrotron x-ray light sources and, most recently, x-ray free electron lasers and table-top ultrafast x-ray sources. While the strength of the scientific case for sources with higher brilliance and finer time resolution is undeniable, it is important to recognize the large body of clearly meritorious, ongoing work using XAFS that does not benefit from such extreme source characteristics. These measurements require only bulk (non-imaging) hard x-ray XAFS that can in many cases even be performed in transmission mode, i.e., thus requiring none of fine focus, high flux, or substantial time resolution. Foremost among these problems in contemporary research are examples in energy sciences, including *in situ* characterization of electrical energy storage[150-171] and of catalysis.[172-192] However, even bulk-like, transmission mode XAFS is exclusively performed at synchrotron light sources; this is not because these studies need the full performance of the beamlines at these facilities, but is instead because of the absence of any alternative.

For the vast majority of other advanced materials and chemical characterization techniques there exists a continuum of instrumentation capabilities having an inverse relationship with their availability: those apparatus with the coarsest performance are inexpensive, widely distributed, and quite easily available for, e.g., teaching purposes or initial sample characterization, while

only the absolutely most advanced instruments exist as rare shared-user facilities or unique research instruments. By contrast, and with only rare exceptions in the last 20 years, 'routine' hard x-ray XAFS[77-82, 85, 193-201] and high-resolution XES[54, 55, 69, 86, 87, 202] can only be performed at the synchrotron light sources. The nearly complete restriction of high-resolution hard x-ray spectroscopies to major user facilities is an anomaly in current scientific practice.

The issue here is not just the adverse consequences of finite, infrequent synchrotron access on existing XAFS and XES research programs, but also that those same limitations necessarily exclude a large body of potentially important scientific or industrial work from even being considered. Hence, we propose that the range of applications of XAFS and high-resolution XES has been directly constrained by the limited, infrequent access to synchrotron x-ray facilities, by the technical and financial barriers to implementing the more complex *in situ* studies that are not easily made portable, by proprietary concerns, and also sometimes by system-specific considerations that inhibit sample transport to the light source, e.g., inherent sample fragility, extreme sensitivity to oxidation, or severe biological or radiological safety considerations. We further propose that the range of applications of these methods has been indirectly constrained in a more subtle way: the absence of any 'introductory level' apparatus poses an immense barrier to teaching these methods to the next generation of scientists and hence restricts the scientific diversity of the future synchrotron user community. These observations are not new. Very similar arguments were made in the early era of synchrotron facility development when XAFS beamlines and laboratory-based XAFS system coexisted, when beamline oversubscription was much less severe, and when each of the size and the scientific range of the XAFS community was much smaller.[72]

For the above reasons, we have begun a critical reinvestigation of conventional laboratory x-ray spectroscopies, i.e., those that do not require high beam brilliance or time resolution and that consequently can make use of conventional laboratory x-ray generators such as x-ray sealed tubes and rotating anode sources. Laboratory-based XAFS played an important role in the early development of the technique[72-76] but has seen only sporadic application in the last 20 years.[77-84, 193, 194, 199-201] More specifically, here we report on a research program aimed at developing a true 'introductory level' x-ray absorption near edge structure (XANES) and high-resolution XES capability. Our goal is to develop an instrument that can be relatively inexpensively assembled from existing, commercial low-maintenance components, that requires no special utilities for electricity or instrument cooling, and that is straightforward to calibrate and operate. We propose that this category of instrument will have application in problems, including electrical energy storage,[151, 153, 160, 162, 166, 167, 203-214] where the near-edge structure contains the necessary critical information about, e.g., oxidation state.[148] Furthermore, the flexibility to measure XANES and XES with the same instrument may provide interesting insight through the complementary information provided by the lowest-energy occupied states (such as pre-edge features in XANES) and the highest-energy unoccupied states (via the valence-level contribution to XES).[16, 28, 106, 107, 127]

Our approach gains some benefit and convenience from the use of current-generation solid-state detectors and the relatively recent development of inexpensive low-power x-ray tubes based on nanotube field emission electron sources,[215, 216] but we find that the largest advantage comes from our use of spherically-bent crystal analyzers (SBCAs) that are now commercially available but that did not exist when laboratory XAFS largely fell out of favor. We find that an SBCA-based scanning monochromator gives quite fine energy resolution while achieving net

monochromator efficiencies that were previously found in only the coarsest-resolution laboratory studies of extended XAFS. With this instrument we obtain excellent XANES spectra for concentrated samples in measurement times of several hours and, rather surprisingly, can also obtain synchrotron-quality (bulk-averaged) nonresonant XES in nearly synchrotron-level measurement times. These results establish groundwork for the broad dissemination of these techniques at the desired 'introductory' level, but also establish important performance milestones that can be extrapolated, in the case of XAFS, to the development of a mid-scale facility based on a more powerful conventional source. Such a facility would allow rapid transmission-mode XANES, and transmission-mode extended x-ray absorption fine structure (EXAFS) on useful time scales, while also opening the possibility of high-resolution fluorescence-mode XANES in the laboratory setting.

This manuscript continues as follows. In Section 4.2, we survey the prior work in laboratory-based x-ray spectroscopy and, *en route*, motivate the expected, substantial gains that come from the use of SBCA optics in such instruments. In Section 4.3 we present the design of the monochromator, and its configuration when used for XES or XANES. In Section 4.4, we present and discuss results for both of these techniques, and also provide considerations that encourage the further development and broad application of laboratory-based, high-resolution x-ray spectroscopies. In Section 4.5, we conclude.

4.2 Prior work in laboratory-based x-ray spectroscopy

4.2.1 X-ray Absorption Fine Structure

We present in Table 4.1 a summary of selected characteristics of many prior conventional laboratory XAFS systems and of the present spectrometer. All prior systems in Table 4.1 used a

Table 4.1. A comparison of laboratory XAFS systems using focusing analyzer optics on a Rowland circle, listed in order of improving energy resolution. The abbreviations used for analyzer type are: J = Johann, JS = Johansson, CBCA = cylindrically-bent crystal analyzer, SBCA = spherically-bent crystal analyzer. The overall monochromator efficiency is captured by the ratio of the measured flux to maximum electron beam power in the x-ray generator. Note that the present study achieves high monochromator efficiency at fine energy resolution through the use of SBCA optics.

	Flux in photons/s (energy in eV)	Max Power (kW)	Flux/Power (photons/ W s)	Energy resolution (eV)	Mono. Crystal	Analyzer type
Knapp, *et al.*, 1978.[217]	$\sim 1 \times 10^6$	1.2	800	14	Ge (220)	JS, CBCA
Cohen, *et al.*, 1979.[218]	5×10^7 (8980)	12	4000	10	LiF (220)	JS, CBCA
Georgopoulos and Knapp, 1981.[219]	4×10^7 (7000-10000)	15	2700	6	Si 400	J, CBCA
Tohji, *et al.* 1983.[220]	3×10^5 (8980)	12	25	5-10	LiF (220)	JS, CBCA
Stern, *et al.*, 1980[76]	5×10^5 (8980)	1.2	400	5	Si 400	J, CBCA
Yuryev, *et al.*, 2007.[82]	2.5×10^5 (8980)	12	20	5	Ge (311)	J, CBCA
Yuryev, *et al.*, 2007.[82]	5×10^4 (8980)	12	4	3	Ge (311)	J, CBCA
Thulke, *et al.*, 1983.[221]	5×10^4 (8980)	12	4	2	Si (111) Si (311) Ge (311)	JS, CBCA
Williams, 1982.[222]	3.7×10^5 (8980)	2	190	2	Ge (333)	JS, CBCA
Present	2×10^4 (8000)	0.01	2000	1	Si (444)	J, SBCA
Present	8×10^3 (7100)	0.01	800	1	Ge (620)	J, SBCA
Present	6×10^3 (7700)	0.01	600	1	Ge (333)	J, SBCA

Rowland circle monochromator based on cylindrically-bent crystal analyzers (CBCA's) to implement an energy-scanning monochromator. We restrict ourselves to focusing (rather than dispersive) spectrometers that operate in the hard energy range most relevant for energy science applications, i.e., 5-10 keV. Note that Table 4.1 is not organized chronologically but is instead ordered from coarsest to finest energy resolution. A strict instrument-to-instrument comparison is made more difficult by the use of different source characteristics, by the different limitations on source operation that followed from the various detectors used, and by the presence of a wide range of analyzer properties such as integral reflectivity, collection solid angle, and simple analyzer curvature (Johann) versus analyzer curvature with surface grinding (Johansson), etc. However, a pragmatic measure of their relative demonstrated efficiencies is given by the monochromatized flux per unit power of their respective x-ray sources, presented in the fourth column of Table 4.1. This efficiency parameter, while imperfect, captures much of the monochromator-to-monochromator variation while also being clearly important for future design consideration, i.e., cost-benefit analysis.

The monochromatized flux per unit generating power in Table 4.1 is nonmonotonic but still illustrates one important, general trend in prior work. Although the obtained energy resolutions are always much coarser than any theoretical limit imposed by the integral reflectivity of the analyzer materials, finer energy resolution is typically associated with greatly decreased monochromator efficiency. This effect was well known and had been carefully explained in the associated literature: finer energy resolution when using a CBCA requires collimation out of the Rowland plane with consequent loss in the effective collection solid angle of the monochromator.[72, 76] The exception to the general trend toward poorer efficiency at higher resolution, that of the study of Williams[222], comes mostly from the use of a particularly favorable

Johansson-style CBCA having a considerably larger collection solid angle than the optics used in many of the other entries for prior work in Table 4.1. The present study was significantly motivated by the observation that modern, *spherically*-bent crystal analyzers (SBCAs) regularly obtain energy resolution below 1 eV while also having larger collection solid angles than the older CBCA's, especially when compared to CBCA's that have been collimated in the non-dispersive direction to obtain fine energy resolution. This expectation is validated by the final few entries in Table 4.1, which we will present and discuss in Section 4.4, below.

4.2.2 X-RAY EMISSION SPECTROSCOPY

The recent history of high-resolution laboratory-based x-ray emission spectroscopy (XES) is rather different than that of XAFS. The information from XES at hard x-ray energies is more restricted and consequently XES has not seen as explosive a growth as synchrotron facilities have proliferated and their brilliance steadily increased. That being said, XES and related techniques do provide crucial information for problems across many fields[16, 24, 66, 116, 223-226], and there has been a steady presence of laboratory-based high-resolution (nonresonant) XES, often using portable instruments that shared time at the synchrotron and in the laboratory. This has been especially true after the development and commercial availability of CCD-based x-ray detectors allowed the highly productive implementation of von Hamos style, wavelength dispersive spectrometers.[54, 55, 69, 86, 87, 202] Laboratory-based work using SBCAs is less common, but includes comparative studies of x-ray emission from direct x-ray excitation as opposed to from K-capture.[18, 223]

4.3 MONOCHROMATOR DESIGN

Unlike in prior laboratory XAFS[75, 77-85, 193, 196, 218, 220-222, 227-233], as we discuss below, our x-ray source and detector are quite compact and low weight. This suggested to us a novel implementation of the Rowland circle geometry that avoids changing the delicate angular-orientation of the SBCA when energy scanning. The general principles of our implementation of the Rowland circle are shown in Figure 4.1. Energy scanning is then achieved by symmetrically scanning the source and detector while synchronously making small adjustments to the location of the SBCA so as to track the moving Rowland circle. Schematic representations of XES and XANES measurements using this general approach are presented in Figure 4.2 and Figure 4.3, respectively; they are distinguished only by changing the sample position, the x-ray tube orientation, and the definition of what constitutes the 'source' in Figure 4.1. The general mechanism and specific implementation of energy scanning is identical in both cases: our instrument is fundamentally a monochromator.

Next, computer-aided design (CAD) renderings of the monochromator, when configured for XES studies, are shown in Figure 4.4 and Figure 4.5; see the figure captions for an initial discussion of the components therein. In the design of any conventional laboratory XAFS instrument, a basic choice must be made concerning which components may, or must, be held stationary and which components must change position or orientation to enable energy scanning. In the common practice[75, 77, 78, 80-85, 193, 196, 218, 220-222, 227-233] of prior work for conventional laboratory XAFS, the x-ray source was kept stationary as matter of great technical simplification: the high-powered x-ray tubes and rotating anodes that were employed had large mass and required high voltage cables and cooling lines that complicated their motion. This led

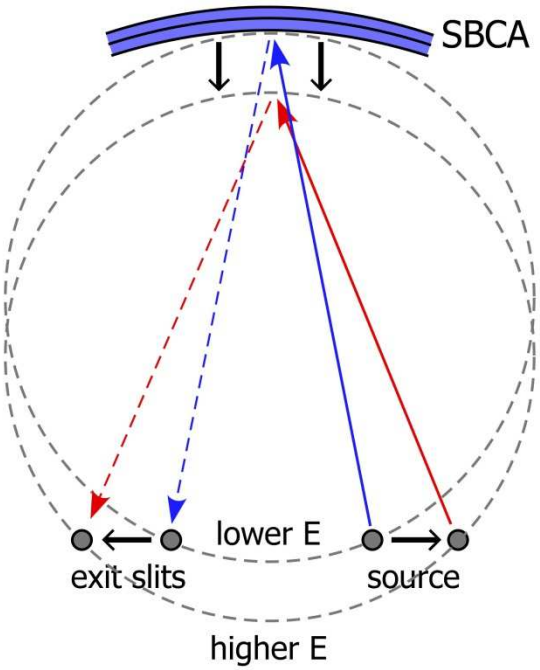

Figure 4.1. Energy scanning of the laboratory x-ray monochromator by synchronized linear motion of the source, the exit slits (and detector), and the spherically-bent crystal analyzer (SBCA). Note the overall symmetry of the configuration and also the simple translation of the Rowland circle.

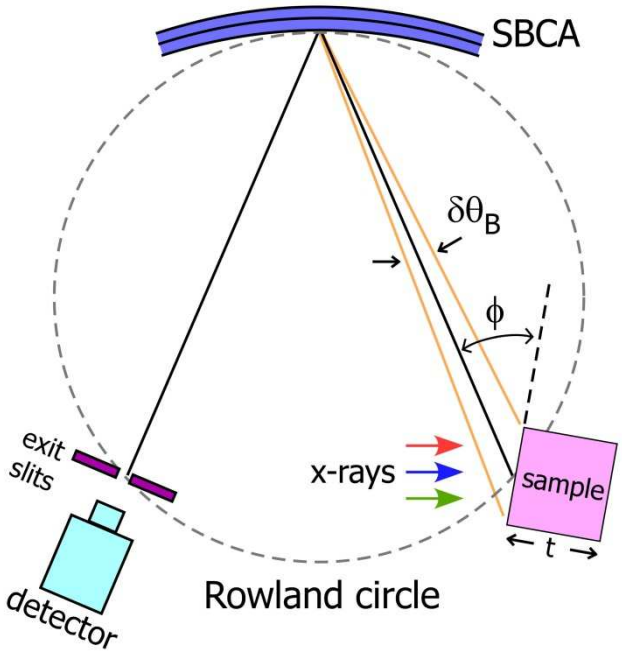

Figure 4.2. The general instrumental configuration for nonresonant x-ray emission spectroscopy with the laboratory monochromator. Broad-band illumination from the x-ray tube source is incident on the face of the idealized sample of thickness *t*. The resulting nonresonant x-ray emission is the analyzed by the spherically-bent crystal analyzer (SBCA) and refocused at the detector. Energy scanning is then implemented as per Figure 4.1.

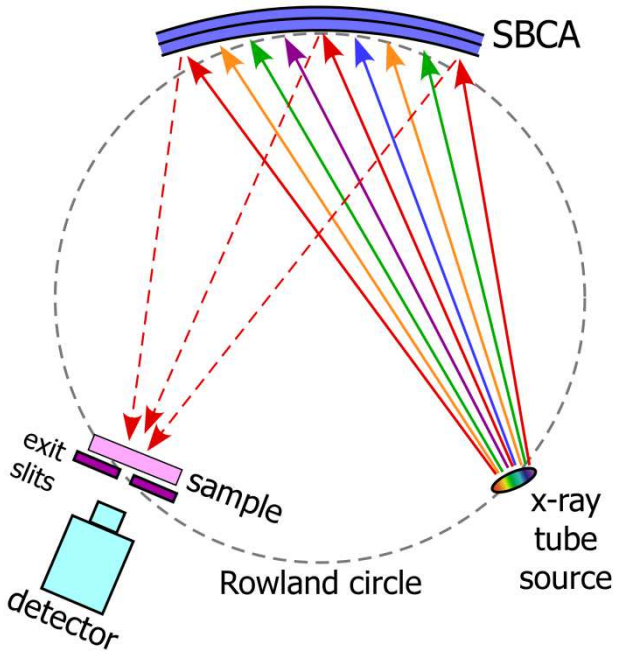

Figure 4.3. The general instrumental configuration for x-ray absorption near edge structure (XANES) studies using the laboratory monochromator. The broadband x-ray radiation from the x-ray tube source directly illuminates the spherically-bent crystal analyzer (SBCA) which monochromatizes and refocuses the radiation onto the sample and the exit slits. The detector measures the transmission through the sample. Energy scanning is then implemented as per Figure 4.1. The energy-dependence of the incident flux is characterized by removing the sample from the beampath and repeating the energy scan.

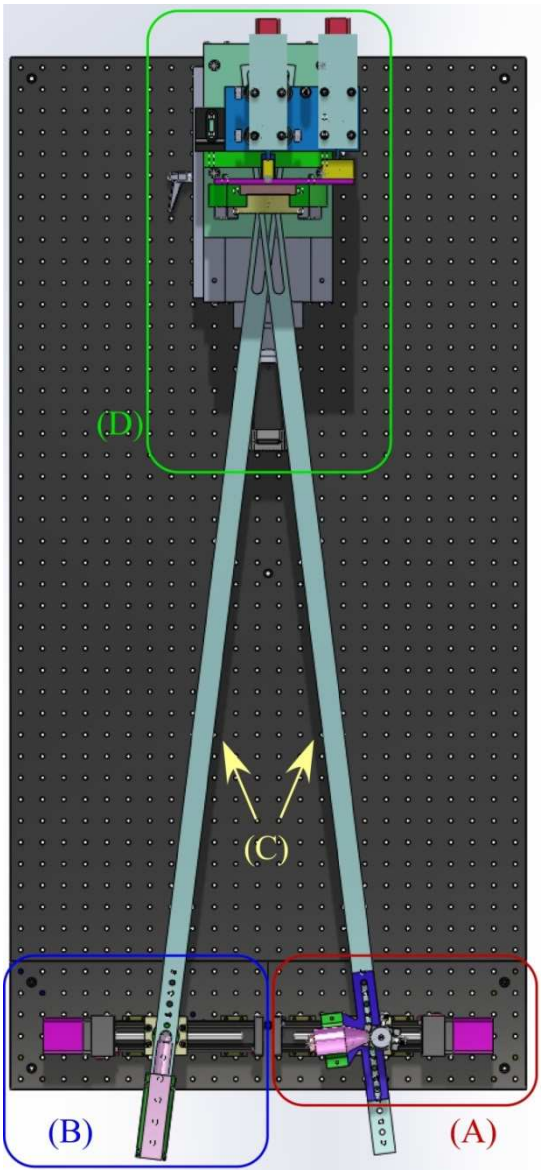

Figure 4.4. Top-view rendering of the Rowland circle monochromator configured for XES measurements. For scale, the spacing of tapped holes in the standard optical breadboard is 25.4 mm. (A): x-ray tube source, sample, manual sample positioner, motorized source-assembly translator; (B): detector, motorized detector translator; (C): steering bars to enforce correct orientation of the source assembly and the detector with respect to the center of the spherically-bent crystal analyzer; (D): two-axis tilt stage, spherically bent crystal analyzer, motorized positioner for linear motion (down the page) of the entire tilt assembly.

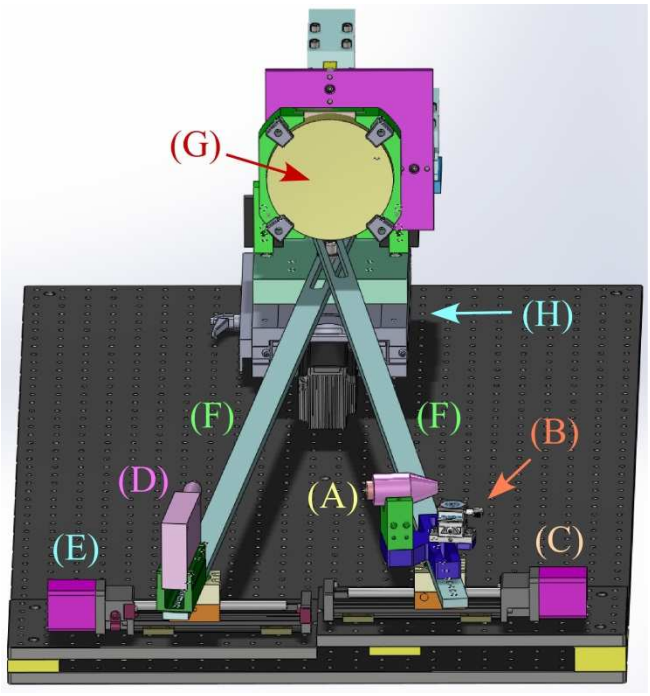

Figure 4.5. Perspective-view rendering of the Rowland circle monochromator configured for XES measurements. For scale, the spacing of tapped holes in the standard optical table is 25.4 mm. (A): x-ray tube source; (B): manual sample positioner; (C): source assembly positioner; (D) detector; (E): detector positioner; (F): steering bars to enforce correct orientation of the source assembly and the detector with respect to the center of the spherically-bent crystal analyzer; (G): spherically-bent crystal analyzer mounted on a two-axis tilt stage; (H): motorized positioner for linear motion (down the page) of the entire tilt assembly.

to the development of the so-called 'linear XAFS spectrometer'.[72, 76] In rare cases where *in situ* studies in extreme environments were needed, the detector was instead kept stationary at fixed orientation and significant effort and engineering creativity was brought to bear on instead scanning the other components.[79]

Here, on the other hand, each of the x-ray tube source and the detector weigh only a few hundred grams; this allows a particularly convenient implementation using just three linear motion stages after an initial tilt-alignment of the SBCA is performed, i.e., the energy scanning model from Figure 4.1. Proper alignment of the source and detector with respect to the center of the SBCA is ensured by the 'steering bars' in Figure 4.3 and Figure 4.4. These rectangular cross-section Al-alloy bars pivot immediately at the source and detector (or exit slit) location on the Rowland circle and also at a pin directly underneath the center of the SBCA. Long slots in the steering bars accommodate the changing chord lengths from source or detector to the SBCA upon energy scanning. We emphasize that this configuration is unique in that the orientation of the SBCA in the laboratory frame does not change; all changes in Bragg angle during energy scanning are due to motion of the linear translation stage, resulting in better than 10-μrad resolution and reproducibility in the Bragg angle of the SBCA.

For clarity of presentation, we have omitted a rendering of either our welded He flight path or the radiation enclosure. The He flight path encompasses ~80% of the total linear travel from source to SBCA to detector. The radiation enclosure is fabricated from lead-lined plywood and includes safety interlock switches that are interfaced with the x-ray source controller. The total external dimensions of the radiation enclosure are 170 cm long, 81 cm wide and 61 cm tall. The spectrometer is in the horizontal plane, on the internal floor of the radiation enclosure. Hinged doors on the top face of the radiation enclosure allow access for sample exchange and instrument

maintenance. The achievable range of Bragg angles is 74 to 87 degrees and is constrained by the internal dimensions of the radiation enclosure together with the range of motion and placements of the linear stages under the source and detector.

For XES (see Figure 4.2), we elaborate that the idealized plane-slab sample has its surface illuminated by the x-ray tube source and rotated by an angle ϕ with respect to the line-of-sight to the center of the SBCA; this serves to decrease the apparent angular width in scattering angle $\delta\theta_B$, thus improving energy resolution while retaining a high rate of x-ray fluorescence generation. Photometric calculations based on this geometry are presented in Section 4.4, below.

With this overview complete, we now present details on the specific components used. While the instrument can be readily reconfigured for different SBCA radii of curvature, it is designed under the assumption that the most common implementation will be for SBCA having a 1-m radius of curvature, i.e., the most commonly available optic. We have used commercial SBCAs (NJ-XRS Tech) and also several made by colleagues at the Advanced Photon Source or in our own lab; all have proven to be acceptable for XANES and XES in our system. To optimize energy resolution and weaken tolerances for component alignment we operate relatively close to backscatter, a condition that usually requires the acquisition or development of a different analyzer for, e.g., each transition metal *K*-edge of interest. This is a logistical, and to some extent financial, disadvantage compared to the older CBCA-based systems which sacrificed energy resolution partially for the convenience of being able to use a single optic over an extremely wide energy range. That being said, a growing variety of SBCA are being fabricated commercially and in numerous research groups, and recent work summarizes multiple possible crystal materials and orientations suitable for each edge or emission line of interest for the hard x-ray regime.[234] Hence the SBCA-availability bottleneck, if it even still exists, is rapidly

disappearing. Switching between different SBCAs is not challenging: a laser diode with a weakly diverging beam is placed at the source location and its refocused reflection from the SBCA is used for prealignment. Once the source is replaced and activated we are able to find the optimum SBCA tilt angles and recover the full Rowland geometry in less than one hour.

The x-ray source is a small, air-cooled tube source with an Au anode (Moxtek, Inc.). The source spot size is ~0.4 mm x 0.4 mm and the maximum accelerating potential and electron current are 50 kV and 0.2 mA, respectively, for a peak power of 0.01 kW. By comparison, the tube and rotating anode x-ray generators used in past conventional laboratory XAFS systems typically had 1 kW to as much as 20 kW total power at similar accelerating potentials.[78] The tube source used here has a transmission geometry wherein the Au film anode is deposited on the inner wall of the thin Be vacuum window; this allows the sample to be placed a few mm away from the anode, resulting in a surprisingly high rate of generation of core-holes and hence of resulting x-ray emission, as we discuss in Section 4.4.

The detector is a silicon drift detector (SDD) having a 25-mm^2 active area and integrated signal processing electronics (Amptek, Inc.). The energy resolution of the SDD is safely better than 200 eV, thus strongly rejecting several backgrounds including fluorescence from the instrument shielding, stray scatter, and the analyzer harmonic content of the analyzed signal from the SBCA. This simplifies shielding considerations and allows us to always use the highest accelerating potential and thus highest generating power from the tube source. The signal within a several-hundred eV band surrounding the energy region of interest for a particular study is integrated for each data point. As shown in Section 4.4, the resulting backgrounds are safely below the level of even valence-level XES upon *K*-shell excitation for 3*d* transition metal species.

Repositioning of the detector and source, as needed for energy scanning (see Figure 4.1), is accomplished by a pair of dovetail linear stages (Velmex, Inc.) whose ~1-mm pitch lead screws are driven by NEMA-17 stepper motors enabled by integrated controllers (Arcus Technology). The overall approach to tilt-alignment of the SBCA closely follows our group's prior experience with nonresonant inelastic x-ray scattering instrumentation used at synchrotron light sources.[235] The SBCA is mounted to an aluminum plate that is supported by a rod-end bearing and is held by springs against the micrometer tips at the vertical and horizontal tangent points of the optic. SBCA tilt alignment is achieved by high-resolution ball-end micrometers (OptoSigma) that have been modified for stepper motor control. The NEMA-11 stepper motors that drive the micrometers use integrated motor controllers (Arcus Technology). The theoretical resolution of the tilt stage is ~50 nrad per micrometer step. While the achieved accuracy is certainly not at this level, we do find that this system easily enables reproducible, stable alignment to safely better than the expected intrinsic rocking curve widths of ~100 μrad. The tilt stage described above is translated via a heavy-duty crossed-roller bearing linear stage (Parker Motion Control Systems) that is driven by a NEMA-23 motor (Arcus Technologies) having, again, an integral motor controller. Motion control and data collection are performed in the LabView environment using RS-485 and USB communications, respectively.

In Figure 4.6, we show $I_{source}(E)$, the spectral intensity of the tube source normalized per unit energy bandwidth and sample solid angle, extrapolated to its maximum power setting. The raw data used for this figure was measured at the lowest tube current of 0.4 μA with the detector 70 cm away to avoid saturation of the SDD. The accelerating potential was 50 kV and the spectrum

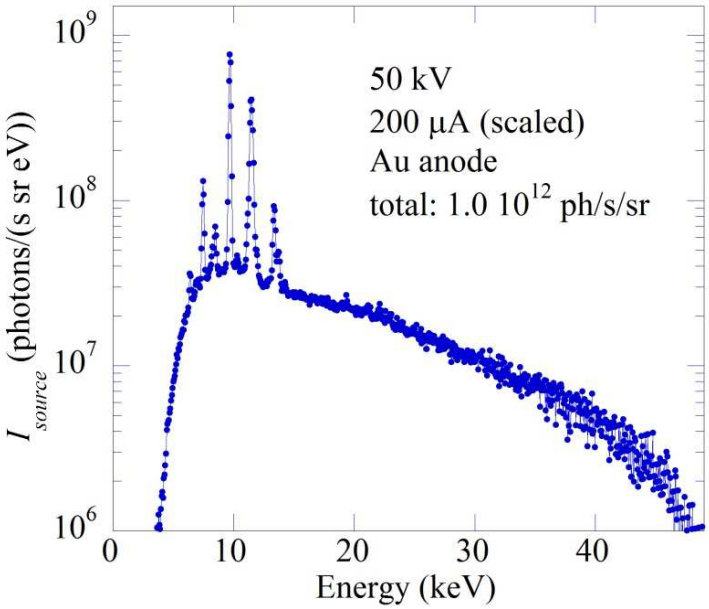

Figure 4.6. The measured spectrum for the x-ray tube source at 50 kV accelerating potential, scaled to the full rated current of 200 μA. Note that the various fluorescence lines are much sharper than shown; the energy resolution of the detector is degraded in this measurement by short shaping times to avoid saturation.

has been corrected for the energy-dependence of the SDD response and for geometric effects to achieve the desired units of photons/(eV s sr). We estimate 40% systematic uncertainty in the overall level of this spectrum and the relative intensity of the high-energy tail to the main ~10 keV region due to uncertainties in the SDD response function, absorption corrections, and other experimental artifacts. The several sharp emission lines are from elemental x-ray emission from the Au thin-film target and a few weaker Pb lines from the collimators used in this measurement. The low-energy cut-off of the bremsstrahlung spectrum is due to the transmission geometry of the anode.

4.4 Results and Discussion

We present below in Sections 4.4.1 and 4.4.2 results and discussion for XANES and XES using the laboratory monochromator. In each case, we both provide representative results and also detailed discussion of photometrics, both as further explanation of the present instrument design and performance and also as guidelines for future improvements in this type of laboratory-based apparatus.

4.4.1 Laboratory XANES

For XANES, it is useful to begin with photometrics and then present and discuss the experimental results. Unlike nonresonant XES, where a large portion of the broadband flux from the x-ray source is useful, XANES specifically requires excitation in a narrow energy range. Consequently, no laboratory system using a bremsstrahlung source will compete on the basis of flux, brilliance, or any other fine technical metric with the regularly attained performance at hard x-ray synchrotron beamlines. That being said, it is important to note that the flux needed for high-quality XANES measurements is rather modest for the special case of transmission-mode, nonimaging studies of a sample with suitable edge-step magnitude. By means of example, consider the calculations presented in Figure 4.7 for the contribution of the 1*s* shell to the x-ray absorption (μ_{1s}) of Co metal with a modeled thickness of 4 μm, chosen to be the same as the commercially-available reference sample used in the measurement below. For these simulations, we begin with a linear background subtraction from a high-quality transmission-mode study of a Co metal foil from the XAFS Model Compounds database[236] to obtain a model for $\mu_{1s}(E)$. We then continue by simulating the transmission of the indicated *average* number of photons, subject to Poisson statistics, through the sample. The resulting $\mu_{1s}(E)$ for each indicated level of

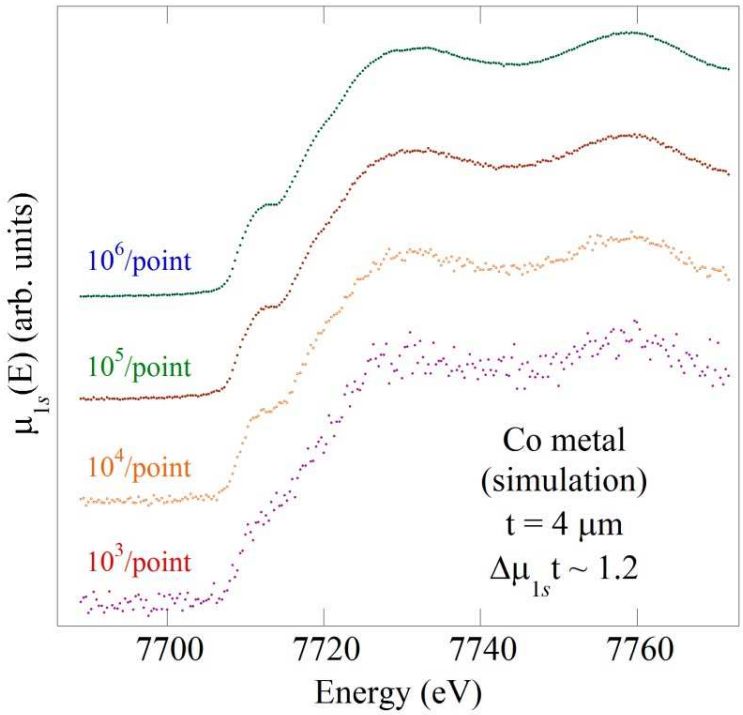

Figure 4.7. Simulated, transmission-mode $\mu_{1s}(E)$ for different numbers of incident photons per data points (as indicated). It is assumed that the Co sample thickness *t* for the simulation is 4 μm so that $\Delta\mu_{1s} \cdot t \sim 1.2$ upon crossing the absorption edge. The simulation is based on a Co metal foil reference spectrum that was taken in transmission mode at a synchrotron light source.[236]

incident average flux per data point is then recovered via Beer's law. As explained below, for the best coordination with present experiment we do not include Poisson statistics for a simulated measurement of the point-by-point incident flux $I_0(E)$. The effects of the exact incident beam spectra on the reference data or on the simulated transmission measurement have not been included.[237] We assess that 10^5 incident photons per measurement point is publication-quality, but 10^6 photons per point will be needed to cleanly resolve subtle pre-edge features and higher exposures would be needed as one moves farther away from the absorption edge, into the extended x-ray absorption fine structure (EXAFS) range.

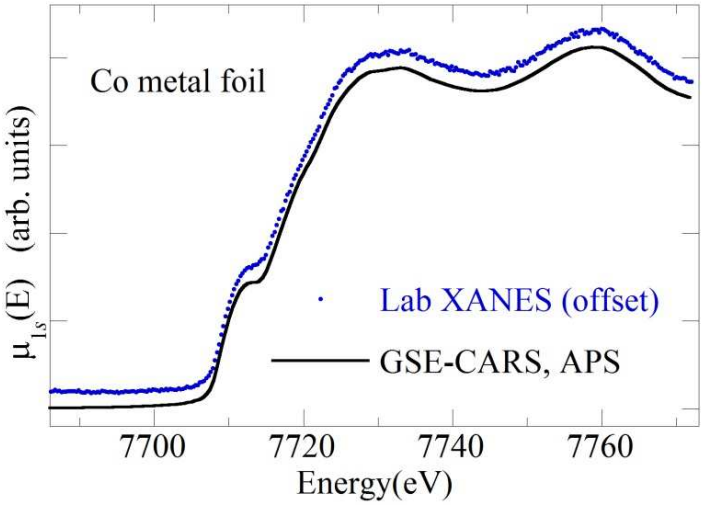

Figure 4.8. XANES for a Co metal foil. For the laboratory XANES data the x-ray tube settings are 50 kV and 200 μA with a brass filter in front of the tube to prevent detector saturation from an Au fluorescence line coincident with a higher Bragg harmonic on the Ge (111) analyzer. Due to the ~3x attenuation of the brass filter, the average incident flux was 2000 photons/s and the integration time for the laboratory XANES data was 80 s per data point. The reference spectrum was taken in transmission mode at a synchrotron light source.[236]

With this context established, we present in Figure 4.8 a comparison between the XANES for a 4-μm thick commercial Co metal reference sample (Exafs Materials) measured with the laboratory monochromator and the synchrotron-based Co reference data used above. The SBCA is a commercial Ge(111) analyzer (NJXRS Tech) where we use a few-hundred eV wide band on the SDD to select the (444) harmonic. The range of Bragg angles is 77.6 to 81.5 degrees. The energy step is 0.3 eV which corresponds to incremental changes of the source and detector positions that vary from 0.15 to 0.24 mm. The consequent incremental motions of the SBCA are 0.073 to 0.077 mm. Fine positioning of the SBCA was not critical; errors of 5 mm had only a small influence on the apparent energy resolution of the resulting XANES scan.

The tube power was set to its maximum value but the flux was attenuated ~3x by a brass filter to prevent detector saturation from an Au fluorescence line that inconveniently reflects from a higher harmonic of the Ge(111) SBCA in the middle of the Bragg angle range for this study. The resulting attenuated flux on the sample is ~2000 photons/s and the transmitted signal $I_T(E)$ was measured with an integration time of 80 s/point. The detector exit slit was 5 mm, i.e., it provided only some shielding from stray radiation but otherwise gave no particular contribution to the final energy resolution. The incident flux $I_0(E)$ was measured by removing the sample and repeating the same energy scan with an integration time of only 10 s/point; the resulting data set was then fit to a low-order polynomial and that resulting smooth function, i.e., not having Poisson noise, is used for normalization. The absorption coefficient is determined by Beer's law, $\mu(E) = -\ln(I_T(E)/I_0(E))$. Possible systematic errors from irreproducibility between the transmission scan and the $I_0(E)$ scan can be minimized by a future improvement to monitor the overall x-ray tube output flux on a point-by-point basis with any detector outside of the line of sight to the SBCA. That being said, manufacturer specifications for essentially all modern x-ray tube sources indicate fluctuations and drifts in tube power that are well below the level needed to influence our study.

The two XANES spectra in Figure 4.8 are in excellent agreement, with only some weak rounding of the mid-edge shoulder at 7712 eV in the laboratory system that is consistent with the consequences of Poisson noise for the incident flux, see Figure 4.7. This suggests that the lab monochromator is performing at an energy resolution that is at least not much coarser than the 1.1-eV resolution expected for the double crystal Si (111) monochromator used for the synchrotron reference study. That being said, it is important to realize the inherent difficulty in directly evaluating energy resolution in a laboratory-source system, whether in terms of its full-

width half maximum or a complete characterization of the energy spectrum. Some progress on this issue may be possible following the methods of de Jonge, et al.[238] where source bandwidth information is extracted from measurements of reference samples of different thicknesses, but it is clear that a broad comparison of lab-based XANES using the methods here and usual synchrotron-based XANES is needed in the long-term, much as has been required for beamline-to-beamline comparisons in the synchrotron community.[239]

Returning now to Table 4.1, we have included several entries for the monochromatized flux in our SBCA-based system. The obtained monochromatized fluxes per unit source power are higher, and in most cases much higher, than seen in all of the older CBCA-based instruments. Based on these results, we anticipate monochromatized fluxes of 10^6 photons/s to 10^7 photons/s if a similar apparatus is constructed using a standard 2 kW line-focus x-ray tube source or a high-powered rotating anode source, respectively. As the ~100-μm source size in the dispersive direction for a standard few-kW line-focus x-ray tube is smaller than that for our present low-powered source, the energy resolution will not degrade and may improve; the use of a line-focus (rather than a point focus) leads to some lost efficiency but is not expected to significantly impact energy resolution, even for wider Bragg angle ranges needed to extend the energy range far enough to penetrate at least somewhat into the extended x-ray absorption fine structure (EXAFS) regime. Such an instrument could serve as a mid-scale user facility, capable of rapid screening of large numbers of ambient samples or, *in situ* electrochemical cells in transmission mode and also capable of fluorescence-mode studies for a useful subset of materials synthesis problems.

The only engineering barrier to implementing such a higher-powered system comes from the larger scale of the x-ray generator itself. This can be addressed in two ways. First, if the intent is

to build quite directly on the present mechanical system, one may note that high-powered x-ray generators are typically available in formats where the final source, whether it is a line-focus glass or ceramic diffraction tube in a tower housing or a rotating anode head, is detachable with long cables for electrical power and cooling water. The engineering for mechanical translation of the x-ray head and associated cables is nontrivial but certainly soluble, as was shown with the much larger rotating anode heads used in earlier lab XAFS systems based on the linear XAFS spectrometer mechanical configuration and CBCA optics.[79, 81] Second, it is important to recognize that the present work contains two significant technical results: the simpler implementation of lab-based spectroscopy using the mechanical configuration of Figures 4 and 5 and also the important observation that modern SBCA are vastly superior to CBCA, as per the flux per unit power metric Table 4.1. Hence, the projected flux levels in Table 4.1 are independent of the choice of mechanical implementation of the Rowland circle, they are a consequence of the higher efficiency of the modern analyzer optic.

4.4.2 LABORATORY NONRESONANT XES

In Figure 4.9 we present the measured XES from a 1-mm thick CoO pressed powder pellet (powder source: Alfa Aesar, 90%). The sample area facing the source is a 1-cm diameter disk, the total offset from the face-center of the sample to the anode is ~3 mm, and the angle ϕ of the sample face to the SBCA is ~15°. The SBCA is the same Ge(111) SBCA and same (444) harmonic as used in the XANES study, above, and a few-hundred eV wide acceptance window is again set on the SDD output. The range of Bragg angles is 79.4 to 85.3 degrees. The energy step is 0.25 eV which corresponds to incremental changes of the source and detector positions that vary from 0.15 to 0.35 mm. The consequent incremental motions of the SBCA are 0.064 to 0.066 mm.

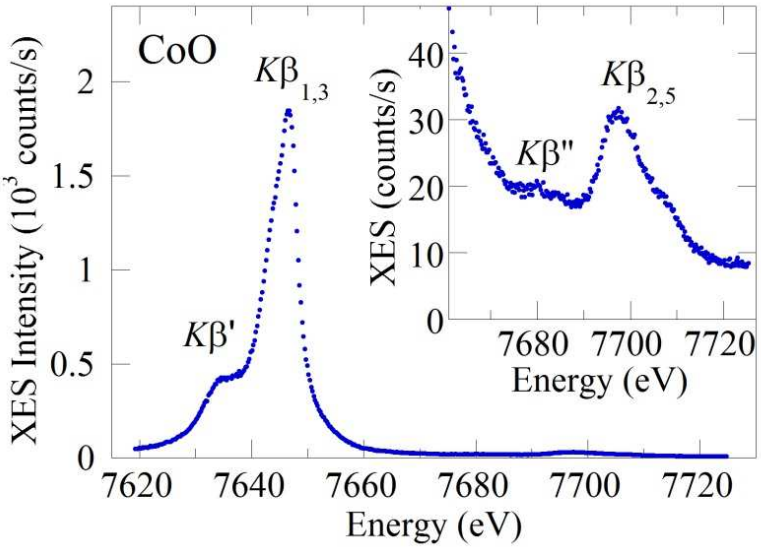

Figure 4.9. Nonresonant XES from a CoO powder sample. The x-ray tube settings were 50 kV and 200 μA. The integration time was 20 s/point in the main *K*β energy range and 80 s/point in the valence region.

Exact positioning of the SBCA with respect to overall offsets of a few mm was, again, not critical.

The data is collected with the maximum tube output. The integration times are 20 s for the main *K*β energy range and 80 s for the valence region. The data cleanly demonstrate all expected features over the entire energy range, including the weak $K\beta''$ peak due to electron transfer from a ligand semicore shell to the 1*s* core-hole on the Co.[16, 107] We emphasize that no background subtraction has been performed. All stray scatter, shielding fluorescence, harmonic signals from the SBCA, and other backgrounds are efficiently rejected by choosing a ~300-eV wide acceptance window on the SDD. This ability to filter backgrounds using the SDD energy resolution is a considerable instrumental advantage in that it reduces the need for all but the most obvious internal shielding, i.e., immediately around the detector and its electronics.

The demonstrated count rates are impressively high. While raw count rates are seldom reported for concentrated systems in synchrotron XES studies, our prior experience with such measurements at monochromatized synchrotron beamlines finds only 10 times larger count rates for an insertion-device beamline operating at 10^{12} photons/s.[70] Consequently, we now move to discuss photometrics for XES. Any effective system for measurement of x-ray emission spectroscopy (XES) must attain a suitable product of fluorescence stimulation rate and net detection efficiency. As the general optical configuration for the lab spectrometer is extremely similar to that used for most XES and other inelastic x-ray scattering methods at synchrotron beamlines,[62, 125, 235, 240-247] we focus here on the useful rate of core-hole creation at the sample by the x-ray tube source. This is the critical parameter that can be used, for example, to predict the relative measurement times for XES with the laboratory spectrometer and with a synchrotron beamline (having known flux and consequent core-hole generation rate).

Consider an x-ray source having a power spectrum $I_{source}(E)$, where $I_{source}(E)$ is normalized by bandwidth and solid angle, i.e., its units are photons/(eV s sr). Assume that this source illuminates a flat sample of thickness t at roughly normal incidence. The rate of core-hole creation in a shell α is then

$$\dot{N}_{core-hole} = \Omega_{sample} \int_0^\infty \frac{I_{source}(E)\, \mu_\alpha(E)}{\mu(E)} (1 - Exp[-\mu(E)t])\, dE \qquad (4.1)$$

where the sample surface subtends a solid angle Ω_{sample} as viewed from the source and where $\mu(E)$ is the absorption coefficient from all processes at energy E but $\mu_\alpha(E)$ is the absorption coefficient for only the shell α at energy E, e.g., the absorption coefficient for 1s ionization of a transition metal species. It is useful to put this into context. A special feature of the low-power tube source used here is the very close approach of samples to the anode, with Ω_{sample} being as large as 1 sr for favorable cases. Making use of the measured $I_{source}(E)$ (see Figure 4.6), we

then estimate $\dot{N}_{core-hole} \sim 8 \times 10^{11}/\mathrm{s}$ for thick, concentrated samples of transition metal species; this estimate has ~40% error due to uncertainties in I_{source} and will be further modified by the exact sample chemistry.

Continuing to the next step in the photometrics, the broadband nature of the excitation from the tube source causes a large fraction of the stimulated x-ray emission to occur so deep in the sample as to be strongly absorbed before escaping. To quantify this issue, we next calculate the rate of x-ray fluorescence escape from the face of the sample in the general direction of the SBCA,

$$\dot{N}_{\alpha\to\beta} = \Omega_{sample} B_{\alpha\to\beta} \int_0^{\infty} \frac{I_{source}(E)\,\mu_{\alpha}(E)}{\mu(E)+(\mu_{\beta}/sin\phi)} \left(1 - Exp[-\left(\mu(E) + \left(\frac{\mu_{\beta}}{sin\phi}\right)\right)t]\right) dE \quad (4.5)$$

In Eq. (4.5), the emission channel is denoted by β, the escape angle from the sample toward the SBCA by ϕ (see Figure 4.2), μ_{β} is the absorption coefficient of the sample at the energy of the emission channel β, and $B_{\alpha\to\beta}$ is the branching ratio into emission in channel β given that an ionization event has occurred in the shell α. The experimentally-useful rate of core-hole generation, $\dot{N}_{\alpha\to\beta}/B_{\alpha\to\beta}$, at $\phi = 15°$ is then estimated to be $\sim 2 \times 10^{11}/\mathrm{s}$ for thick, concentrated samples of transition metal species with, again, ~40% errors due to systematic uncertainties in $I_{source}(E)$.

It is important to note that the above estimate is surprisingly large, given that we are using only an inexpensive, very low-power commercial x-ray tube source. By comparison, at the Advanced Photon Source the flux of a typical (monochromatized) XAS beamline falls into the range $\sim 2 \times 10^{10}/\mathrm{s}$ to $\sim 10^{11}/\mathrm{s}$ for bending magnet beamlines, depending on upstream concentration optics, and is in the range $\sim 1 \times 10^{12}/\mathrm{s}$ to $\sim 5 \times 10^{13}/\mathrm{s}$ for insertion device or wiggler beamlines. These fluxes should be decreased somewhat by sample geometry effects for a strict comparison

to the above estimate of $\dot{N}_{\alpha\to\beta}/B_{\alpha\to\beta}$ and alternatively could be increased by a large factor through the less-common use of broadband monochromators, such as is most important when studying very dilute samples.[225] That being said, a key observation remains that is in agreement with the above experimental results: many nonresonant XES studies of concentrated samples can be performed with our laboratory instrument without incurring heroic integration times, and often with measurement times quite comparable to those at synchrotron beamlines.

Finally, given the above results and considerations, it is reasonable to ask whether the use of a more powerful x-ray source could give added benefits for lab-based XES. Somewhat counterintuitively, such an upgrade yields strong advantage in only certain cases. In Table 4.2, we present several relevant characteristics of conventional x-ray generators for the hard x-ray region. While cross-apparatus comparisons are certainly influenced by some fine design details, all such systems can use the same target (anode) materials and typically operate at the same accelerating potentials (~50 kV) and the emitted flux per unit solid angle for each source is therefore roughly proportional to the total electron beam power *P*. For the focusing-geometry monochromator used here, the area of the sample facing the SBCA is independent of the choice of source (it is set by the Bragg angle and the desired energy resolution), and consequently the rate of core-hole generation for any sample is proportional to P/x^2, where x is the distance from the anode to the sample. The final two columns in Table 4.2 provide this metric for the case where the sample is at the closest approach (d) to the anode, as can be achieved for ambient samples, and at closest approach plus 20 mm, as would be needed for samples in special environments such as cryostats, furnaces, or chemical reactors. For ambient samples, P/d^2 has only modest benefits when upgrading from the present 10 W tube source to a ~20 kW rotating anode, despite the ~30x higher cost for the more intense source. This is due to the much larger

Table 4.2. For various laboratory x-ray generators, a comparison of the broadband flux (including both fluorescence lines and bremsstrahlung) per unit sample face area available at the exit window and also recessed by 20 mm, to allow for environmental apparatus. As the target materials and accelerating potentials are similar for all such generators, the total fluxes are roughly proportional to the total electron beam power. See the text for discussion of the P/d^2 and $P/(d + 20\text{mm})^2$ metrics.

X-ray generator	Electron beam power, P (W)	Sample closest approach, d (mm)	P/d^2 (W/mm^2)	$P/(d + 20\text{mm})^2$ (W/mm^2)
Rotating anode	20×10^3	~100	2.0	1.4
High-power tube	3×10^3	40	1.9	0.8
Mid-power tube	300	15	1.3	0.24
Low-power tube	10	3	1.1	0.02

distance from the source anode to the Be vacuum window, a fact mandated by the higher IR heat load on the Be window. For systems in special environments, on the other hand, any substantial offset of the sample itself from the exit window of the x-ray source results in strongly decreased efficiency for the low-power tube source but has less impact on the higher powered sources.

4.5 CONCLUSIONS

In summary, we report the development and performance of a modern, 'introductory level' instrument for laboratory based studies of x-ray absorption near edge structure (XANES) and high-resolution x-ray emission spectroscopy (XES) in the energy range ~5 keV to ~10 keV. Unlike the earlier generation of Rowland-circle based focusing monochromators for laboratory XAFS, we use a modern spherically-bent crystal analyzer as the Bragg analyzer, thus obtaining

much improved efficiency at ~1-eV energy resolution. For transmission-mode XANES of concentrated samples, a few hours measurement time yields relatively quiet data that is in excellent agreement with synchrotron studies. For XES, we find a surprisingly effective system capable of synchrotron-quality results in nearly synchrotron-level measurement times for ambient samples. Given the accessible cost and easy assembly and operations of the present instrument, we believe that this low-performance, high-access approach can have a significant scientific and technical impact in the existing synchrotron x-ray spectroscopy community and also as a low-barrier entry path for new users and their instruction. Furthermore, the demonstrated monochromatic flux and energy resolution serves as proof of principle for the technical viability of a mid-scale XAFS user facility employing a standard few-kW line-focus tube source or higher-powered rotating anode x-ray generator.

Chapter 5. BENCHTOP NONRESONANT X-RAY EMISSION SPECTROSCOPY

Originally published as: D. R. Mortensen, G. T. Seidler, A. S. Ditter and P. Glatzel, Journal of Physics: Conference Series **712** (1), 012036 (2016).

Recently developed instrumentation at the University of Washington has allowed for nonresonant x-ray emission spectra (XES) to be measured in a laboratory-setting with an inexpensive, easily operated system. We present a critical evaluation of this equipment by means of Kβ and valence-level XES measurements for several Co compounds. We find peak count rates of ~5000/s for concentrated samples and a robust relative energy scale with reproducibility of 25 meV or better. We furthermore find excellent agreement with synchrotron measurements with only modest loss in energy resolution. Instruments such as ours, based on only conventional sources that are widely sold for elemental analysis by x-ray fluorescence, can fill an important role to diversify the research applications of XES both by their presence in non-synchrotron laboratories and by their use in conjunction with XAFS beamlines where the complementarity of XAFS and XES holds high scientific potential.

5.1 INTRODUCTION

Nonresonant x-ray emission spectroscopy (XES), while far less common as ubiquitous as x-ray absorption spectroscopy (XAS), has seen steady growth in a number of fields over the past several decades. In particular, Kβ (3p→1s) and valence-level XES has seen extensive use in determining spin state, oxidation state, and ligand speciation in 3d transition-metal materials.[16, 24, 248] Because this technique probes the emissions resulting from the filling of core-holes, it

provides complementary information to XAS and combination of the two spectroscopies is a natural and powerful extension.

Unfortunately the infrastructure for XES has lagged considerably behind that for XAS with only a handful of synchrotron end stations dedicated to such measurements.[63, 64, 245, 249] This access scarcity has significantly hampered the further development of XES as a routine complement to XAS. We have recently demonstrated, however, that benchtop instrumentation based on high-resolution spherically-bent crystal analyzers (SBCAs) can in many cases provide synchrotron-quality XES measurements.[250] Here we explore the capability and limitations of this laboratory-based equipment via a direct comparison to synchrotron data and we also report on an instrumental improvement that helps to finely anchor the accuracy of the energy scale.

5.2 Experimental Details

Laboratory spectra were recorded using a Rowland-circle monochromator recently developed at the University of Washington,[250] see Figure 5.1. X rays are generated by a conventional tube source (Moxtek) with an Au anode operated at 40 kV bias and 200 μA current, i.e., only 8 W total electron beam power. As has been emphasized elsewhere,[250] the small anode-to-sample distance possible with this type of source allows the sample to subtend a very large solid angle, giving highly efficient excitation that can reach rates intermediate between those typical for a monochromatized bending magnet and insertion device at a third-generation synchrotron. The sample fluorescence was analyzed and refocused at the detector position by a 1-m radius of curvature Ge (444) SBCA (XRS Tech). A geometric correction, based on ray-tracing calculations (see Section 6.5), is applied to compensate for the Bragg angle dependence of the height of the refocused spot at the finite-height (5-mm) detector.

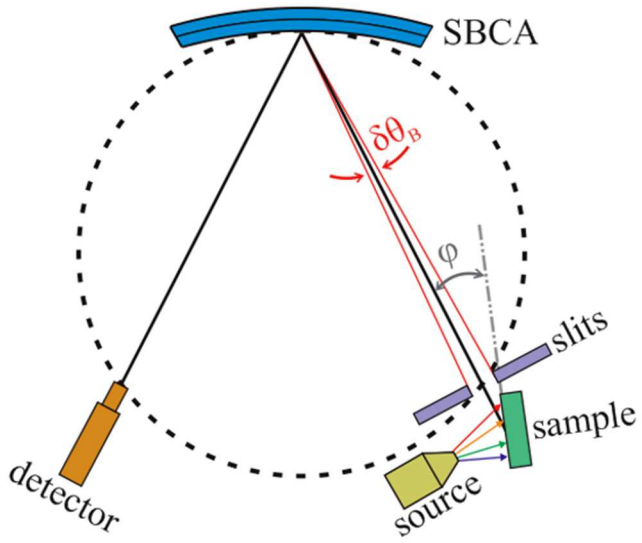

Figure 5.1. The lab-based Rowland-circle spectrometer.[250] The slits in front of the sample constrain the angular width ($\delta\theta_B$) probed by the analyzer which improves energy resolution and reproducibility. The sample is slightly rotated (φ) to allow improved line-of-sight to the SBCA.

The sample is rotated slightly (~15°) to provide improved line-of-sight to the analyzer for the fluorescence while still allowing for minimal offset from the x-ray tube anode (~3 mm). Most recently, instead of placing the sample directly on the Rowland geometry we use a narrow entrance slit on the Rowland circle and move the sample + source subassembly ~10 mm behind the slit. The purpose of this slit is two-fold. First, the dominant limit on energy resolution is the apparent angular width of the illuminated sample area as seen by the SBCA. The entrance slit gives some ability to tune the resolution by adjusting its width. Higher resolution of course comes at the cost of lower count rates and the optimal tradeoff is determined on a case-by-case basis. For this study a slit width of 0.5 mm was selected. This corresponds to an angular width of 0.03° (0.48 eV) at 82.93° Bragg angle (7650 eV).

The second purpose of the entrance slit is more subtle and involves the difficulty of reproducing exact sample position. Since the relative energy scale is determined geometrically, a small lateral misalignment of the sample will register as an incorrect energy shift in the resulting spectrum. This ambiguity presents a significant barrier to cross-comparisons between different samples, which is especially pressing in the case of Kβ XES from 3d transition metal compounds where shifts in the $K\beta_{1,3}$ peak can indicate changes in spin state and other local electronic properties.[16] With the slit constraining the angular range being sampled by the SBCA, however, this becomes a minor issue; a misalignment large enough to meaningfully shift the energy scale will fall outside of the sampled range, resulting in an obviously reduced signal. For means of example, we measured CoO $K\beta_{1,3}$ at several lateral sample positions as well as a spectrum where the sample was removed, replaced, and realigned – see Figure 5.2. These results demonstrate a highly robust energy scale that is insensitive to exact sample position. The inset of Figure 5.2 shows that shifts in the energy scale as small as ~25 meV are accompanied by factor of 2 decreases in overall intensity. Simple optimization of signal intensity with respect to the sample position behind the entrance slit therefore ensures outstanding consistency of energy scale between different measurements.

For the study below, synchrotron measurements were performed at beamline ID26 of the European Synchrotron Radiation Facility (ESRF). The incident energy was tuned to 7.8 keV using a double Si (111) monochromator. The total incident flux was ~ 2 x 10^{13} photons/s. Samples were oriented at 45° in the scattering plane, resulting in a beamsize of 0.5 mm in-plane and 1 mm out-of-plane. The resulting fluorescence was analyzed by an array of five Ge (444) SBCAs in a 1-m Rowland circle geometry. The energy resolution, which varies slightly between SBCAs, is ~1.1 eV as determined from the FWHM of elastic scatter lines.

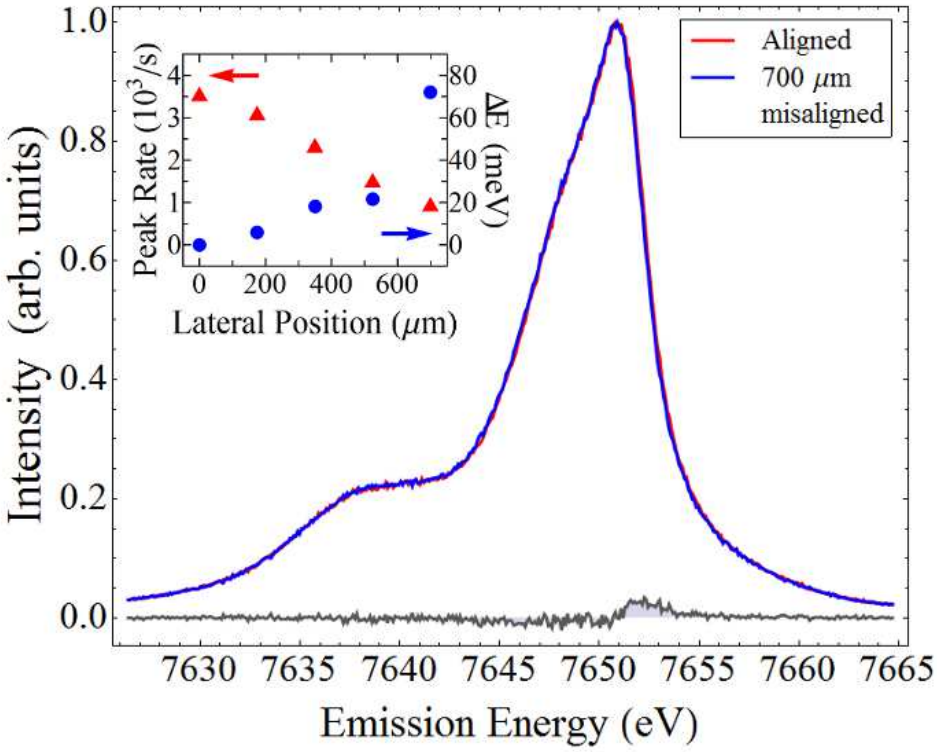

Figure 5.2. Peak-intensity normalized CoO Kβ spectra measured at the aligned and the extreme misaligned location. The gray curve shows the residual between the two spectra. Inset: the peak count rate and energy shift as a function of lateral sample position.

Samples were prepared from high purity powder (99.99% Co3O4; 99.5% LiCoO2) from Alfa Aesar. The same samples were measured at both the University of Washington lab and the ESRF, thus eliminating possible systematic effects due to variations in sample preparation.

5.3 Results and Discussion

In Figure 5.3 we present a laboratory/synchrotron comparison of Kβ XES for Co_3O_4 and $LiCoO_2$. To better overlay with the laboratory data the ESRF spectra have been additionally broadened by convolving with a Gaussian of FWHM = 0.8 eV. This is larger broadening than

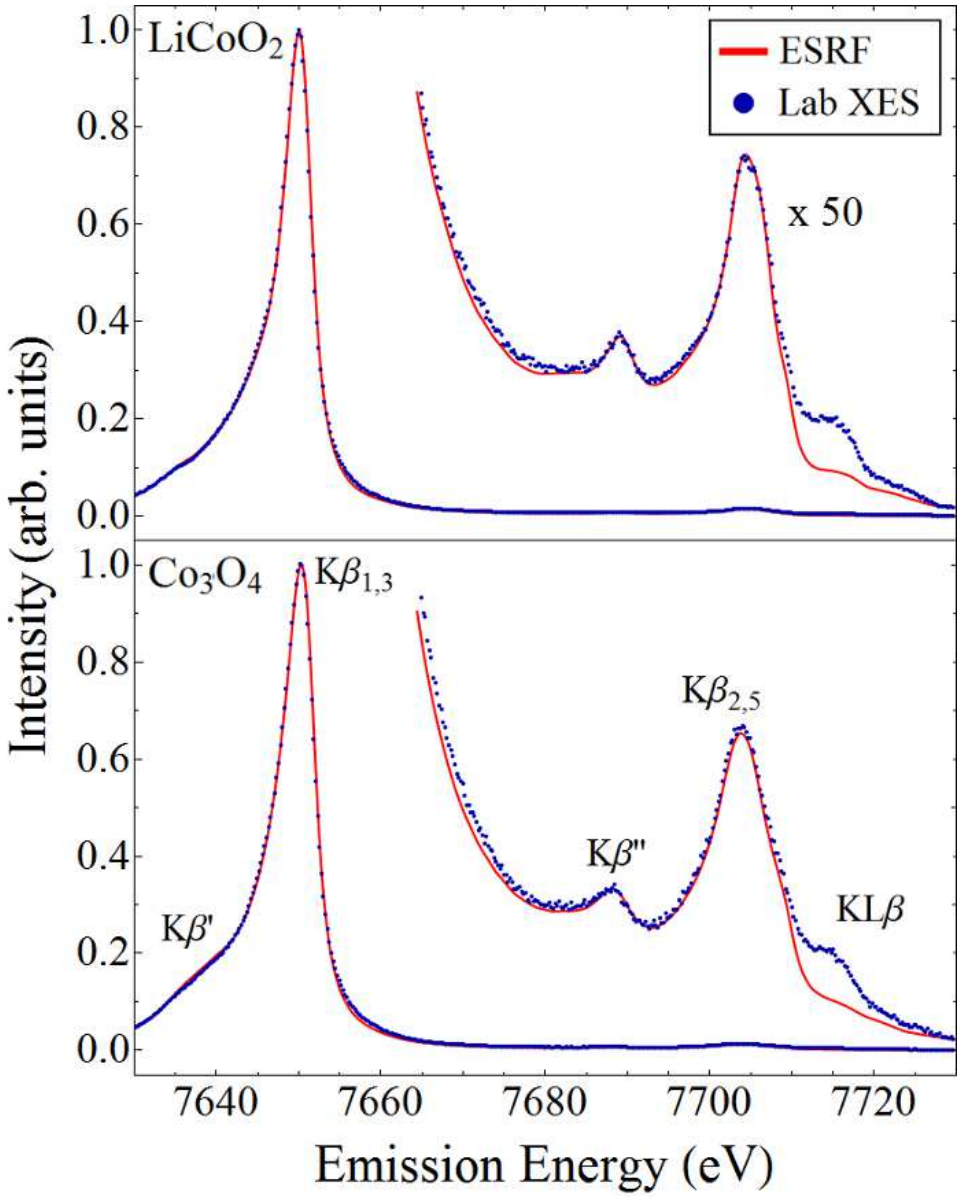

Figure 5.3. Kβ XES for $LiCoO_2$ and Co_3O_4 powder samples. The red curve shows spectra collected as ESRF; blue dots show data taken using the laboratory-based instrument described in the text. All spectra have been normalized to peak intensity. For ease of presentation, the valence-to-core emission is shown amplified 50x. The ESRF results have been broadened by 0.8 eV to match the slightly poorer energy resolution of the lab XES results; see the text for discussion.

expected from the finite size of the entrance slit discussed above and is mostly likely due to the SBCA being slightly off circle in the laboratory system. Nonetheless the net effective energy resolution of ~1.4 eV is more than sufficient to resolve the key XES features without loss in scientific merit.

The two datasets are in excellent agreement for both the main Kβ ($K\beta_{1,3}$ and Kβ′) and valence-to-core ($K\beta_{2,5}$ and Kβ″) emission lines. The only discrepancy is the KLβ feature present only in the laboratory data. This emission is the result of a multi-electron excitation[95] and therefore exhibits a threshold behavior at roughly the K + L-edge binding energies. The excitation energy for the ESRF data (7.8 keV) is well below this threshold. The broadband tube source in the laboratory setup, however, emits x rays with energies up to 40 keV resulting in sizeable KLβ emission.

Despite the low-powered x-ray tube used here, the peak count rates at $K\beta_{1,3}$ are ~5 x 10^3/s, allowing high quality spectra in very useful measurement times. The measurement time for the main Kβ XES was less than one hour while the valence XES required ~6 hours of data collection for cleanest statistics. Count-rate improvement of up to 100x could be realized by upgrading the x-ray source to a kW-level commercial tube of the type used commonly in fluorescence studies for elemental analysis. For comparison the ESRF measurements averaged ~2 x 10^6/s/SBCA at peak.

5.4 Conclusion

We have demonstrated the effectiveness of inexpensive, easily assembled and operated benchtop equipment using only low-powered, conventional x-ray sources for high-resolution XES measurements. We find easy measurement of even the lowest-intensity valence-level

emission lines for concentrated samples and also find excellent agreement with synchrotron-based studies. This versatile instrument design could have significant application in many fields where transition-metal and lanthanide compounds are of central importance, including electrical energy storage, f-electron chemistry, catalysis, and environmental chemistry. In addition to extending routine XES beyond the confines of synchrotron light sources, we propose that this type of user-friendly spectrometer could be used as an on-site supplement to XAFS beamlines allowing XES measurements without using synchrotron beamtime.

Chapter 6. ROBUST OPTIC ALIGNMENT IN A TILT-FREE IMPLEMENTATION OF THE ROWLAND CIRCLE SPECTROMETER

In preparation for publication: D. R. Mortensen and G. T. Seidler, Nuclear Instruments and Methods in Physics Research Section B: Beam Interactions with Materials and Atoms, (2016).

Spherically bent crystal analyzers (SBCAs) are important components in both synchrotron- and lab-based x-ray emission spectrometers and also in lab-based monochromators for x-ray absorption fine structure. The imperfect parallelness between the desired crystal plane and the wafer surface, usually called "wafer miscut", introduces an ambiguous re-focusing error which has commonly led to the use of a two-axis tilt for fine alignment of the optic onto the Rowland circle configuration. This imposes additional cost and complexity for each of instrument construction, maintenance, and operation. The low brilliance of laboratory x-ray source in particular can make alignment onerous in applications lacking a broad, strong signal line. Here a new method is presented for characterizing and orienting SBCA miscut to eliminate such fine-tilt adjustment requirements. This result is implemented and shown to greatly simplify SBCA initial alignment while also providing rapid, extremely reproducible re-insertion of any aligned SBCA, i.e., without the need for any subsequent recalibration. These improvements come without sacrifice in spectrometer performance.

6.1 INTRODUCTION

One of the most important advances in hard x-ray spectroscopy has been the development and proliferation of spherically bent crystal analyzers (SBCAs). When employed in the Rowland circle geometry [47, 48], these x-ray optics monochromatize and refocus point-source input via Bragg reflection. The intrinsically narrow bandpasses of the perfect crystals used in construction result in resolutions of ~1-eV for the simplest applications to as little as a few-meV for diced analyzers in near-backscatter geometries [251-253]. Such qualities make SBCAs an integral component in both synchrotron- and laboratory-based instrumentation [16, 60, 62-64, 223, 250, 254-259].

SBCAs are manufactured by bonding or gluing flat Si or Ge wafers to a shaped surface, usually a concave glass lens [44-46], so that the resulting crystal surface achieves the desired radius of curvature, i.e., equal to the Rowland circle diameter. However, due to limitations imposed during wafer slicing from large single-crystal boules and subsequent polishing, the underlying crystal planes typically have so-called miscut angles of 0.1 – 0.5° with respect to the crystal surface. While this fabrication error generally does not significantly degrade the performance of the optic, as we will discuss in Section 6.5, it complicates the implementation of any Rowland circle spectrometer, previously leading to the use of a two-axis tilt for fine alignment of the SBCA as a compensation for wafer miscut even in the hypothetical absence of other positional or alignment errors. These fine alignment requirements increase instrument complexity and cost in each of design, construction, operations and maintenance.

Here we demonstrate that careful consideration of the orientation of the miscut-error with respect to the symmetry axis of the SBCA has dramatic consequences for spectrometer design and operations. In particular, we demonstrate that the two-axis tilt can be removed from a

Rowland circle SBCA spectrometer without loss of performance and, in fact, with considerable simplification in instrument design and ease of use (US Provisional Patent 62/271,992).

This paper continues as follows. In Section 6.2, we introduce general considerations of wafer miscut and Rowland circle operations. In Section 6.3, we demonstrate the expected sensitivity of SBCA alignment to both the magnitude of the miscut and also its orientation with respect to the Rowland circle, all when using a conventional spectrometer that includes the two-axis tilt, i.e., in the usual ”symmetric Rowland” configuration. In Section 6.4, we instead introduce the “asymmetric Rowland” configuration and provide the major results of this paper. We find that alignment of the miscut into the Rowland plane allows full compensation with a detector offset, enabling complete removal of the two-axis tilt behind the SBCA. In this configuration, we find easy initial SBCA alignment which is then permanent, in that an aligned SBCA can be removed and then later reinstalled with no loss of performance and with strongly, immediately reproducible energy scales. In Section 6.5 we provide additional results in support of these assertions, including especially ray-tracing results for the focal errors induced by our approach. Finally, in Section 6.6 we summarize and conclude.

6.2 COMPENSATING FOR WAFER MISCUT IN SBCA ALIGNMENT

The effect of wafer miscut is illustrated in Figure 6.1. A miscut crystal has a tilt in its reciprocal lattice vector, $\vec{G}$, (i.e., the vector perpendicular to desired crystal plane) with respect to the surface normal, $\vec{n}$, at every point on the wafer and hence also on the curved optic. This introduces a serious hurdle to SBCA alignment. In standard practice, an SBCA is prealigned using optical reflection of a diverging laser. In this specular reflection the refocusing geometry is determined by the surface normal, $\vec{n}$. X-ray scatter, however, occurs in the crystal bulk and its reflection is wholly dependent on $\vec{G}$. The result of miscut is therefore an ambiguous deviation in

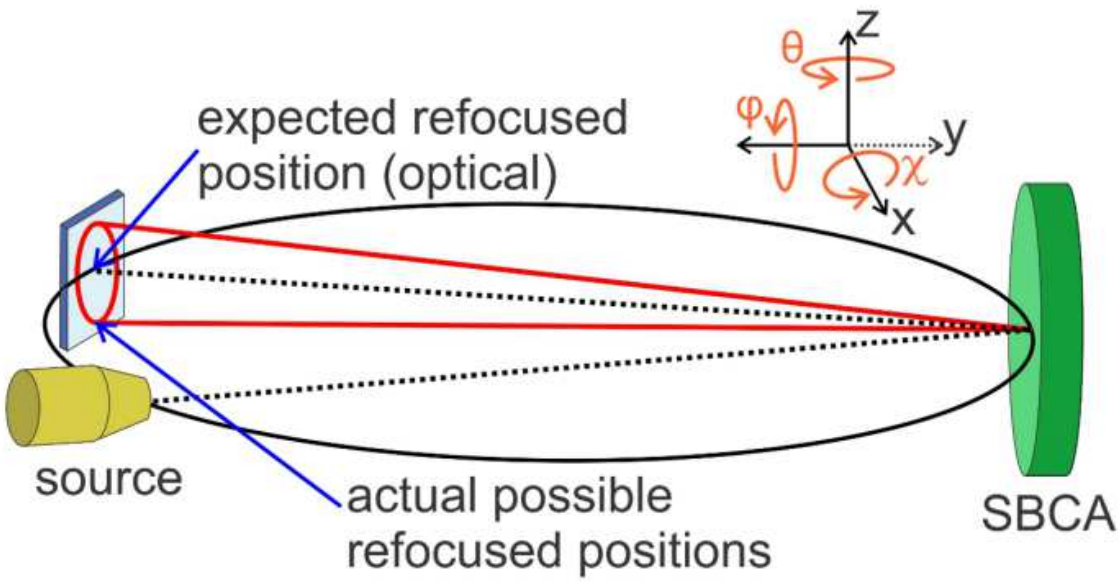

Figure 6.1. The effect of crystal miscut on the refocused position of the monochromatized beam. Due to the symmetry–breaking of the miscut the azimuthal, or "clock", angle (φ) becomes a relevant parameter directly affecting the reflection geometry. The yaw (θ) and pitch (χ) of the SBCA are typically adjusted to steer the refocused beam back onto the expected focal location on the Rowland circle.

the x-ray reflection away from the optical light used in alignment (i.e., the expected geometry in the absence of wafer miscut).

The ambiguity, as encompassed by a circle of possible refocus positions shown in Figure 6.1, is due to the new degree of freedom introduced into the system by the symmetry-breaking of the wafer miscut: the azimuthal, or "clock" angle (φ) of the SBCA is now relevant and couples directly to the orientation of $\vec{G}$ and thus to the re-focus position. The miscut is not known a priori, and consequently even the most carefully engineered instruments require a means for compensation.

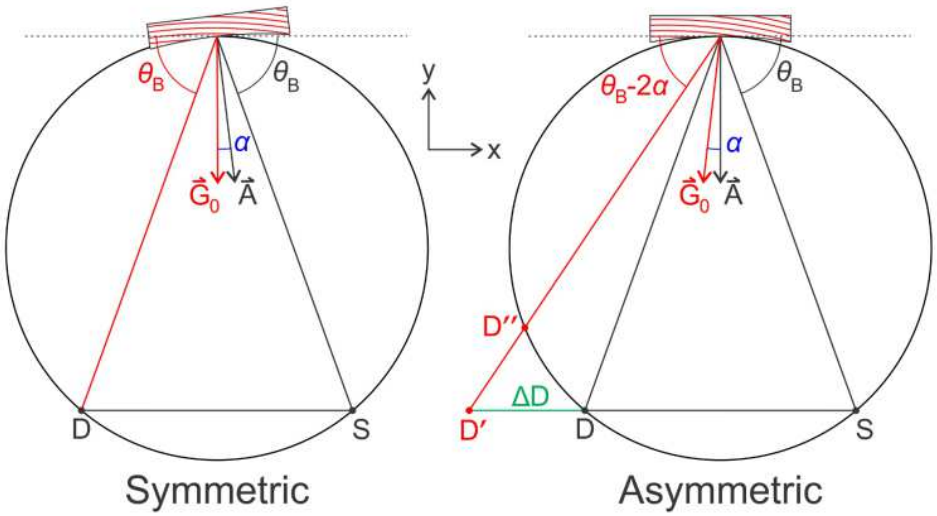

Figure 6.2. Two methods of correcting for a wafer miscut of magnitude α. Here the clock angle can be thought of as a rotation of $\vec{G}_0$ about the SBCA symmetry axis $\vec{A}$. (Left) The symmetric Rowland case where θ and χ tilts are adjusted to steer the reflected beam (red line) back onto the expected detector position (D). Note that such an adjustment means the SBCA is no longer tangent to the Rowland circle. (Right) The asymmetric Rowland configuration where the SBCA is held fixed and the detector is moved to find the monochromatized beam. The simplest scheme offsets the detector by ΔD along the x-axis of the source (S) to an off-circle location (D'). Alternatively, the detector could be moved back on-circle (D'').

The canonical solution has been to use a two-axis (θ, χ) tilt on each SBCA to steer the monochromatized beam back to the optically-determined, symmetric detector position. This places the reciprocal lattice vector at the center of the SBCA, $\vec{G}_0$, at the high-symmetry bisector of source and detector. This is shown schematically as the "symmetric Rowland" configuration in Figure 6.2.

This alignment process, while often tedious, is technically straightforward at synchrotron light-sources: the excellent tunability ensures that an elastic scatter line can always be obtained at the

desired alignment energy. Furthermore, due to the high brilliance, the initial alignment can be off appreciably with the tails of the scatter line still being strong enough to generate a tune-up signal on the detector. Nonetheless, such a scheme requires realignment each time the optic is installed.

Two-tilt alignment is more arduous for laboratory-based spectrometers which employ low-brilliance, bremsstrahlung tube sources. In particular, emission spectrometers often lack strong signal except at certain, narrow Bragg angles (*i.e.*, the exact parameter unknown until post-alignment). In some cases, such as low concentrations or weak valence-to-core lines, an appropriate alignment signal is absent altogether. While highly dependent on each specific system and optic, these situations can frequently result in alignment times of order one hour or more.

In this work we propose an alternative correction scheme in which the SBCA tilts are held fixed at $\theta = \chi \cong 0°$ as a consequence of two changes in operation: (1) the optic clock angle φ is chosen such that $\vec{G}_0$ is rotated into the Rowland plane; and (2) the detector position is offset to the actual refocused path. This is shown in Figure 6.2 as the "asymmetric Rowland" configuration. The remainder of this paper looks at how the miscut can be determined for instruments in the symmetric or asymmetric configuration, and, more importantly, demonstrates substantial simplification and improved ease of operation for the latter design. We furthermore demonstrate how the asymmetric configuration requires an SBCA to be aligned only a single time, allowing for "plug and play" operation upon subsequent use.

6.3 SYMMETRIC ROWLAND CONFIGURATION

It has previously been shown that SBCA miscut can be accurately determined through careful optical alignment and subsequent collimated-beam x-ray diffraction measurements from the

analyzer center [260]. Here we demonstrate an alternative method that is useful for illustrating the consequences of the conical locus of possible refocus positions discussed above (Figure 6.1).

This method uses only the equipment already standard for symmetric Rowland circle spectrometers, namely a two-axis tilt. The first step of this procedure is the same as for any alignment: the optic is mounted and its yaw (θ) and pitch (χ) are adjusted to maximize detected signal. The clock angle (φ) is then rotated by a known amount and the above step is repeated. When this procedure is carefully carried out through a full 360° revolution the optimized θ and χ tilts trace out a circle, corresponding to the rotation of $\vec{G}$ at the SBCA center, $\vec{G}_0$, about the optic symmetry axis, $\vec{A}$. While the spatial map of $\vec{G}$ as a function of position along the spherically curved surface is indeed more complex, one must remember the key point of Rowland circle operation is that, absent the well-known inherent geometric errors of Johann-typed SBCAs, the angle of incidence of the x-rays from a point source is the same at every point on the SBCA surface. Note that the angular radius of the circle traced in θ and χ is equal to twice the miscut angle, α.

To test this premise we performed the above procedure on two Si 111 and one Si 551 SBCAs (all from XRS Tech), each having 100-mm wafer diameter and 1-m radius of curvature. Data for this study was collected using a laboratory-based spectrometer recently developed at the University of Washington [250, 258, 259]. X rays were generated by emission from Cu or Ni foils excited by bremsstrahlung output from a conventional tube source (Moxtek) with an Au anode operated at 35 kV and 200 μA. The Cu and Ni emission lines were used to provide strong, narrow signals for accurate calibration and for fine tests of changes in spectrometer alignment, resolution and energy scale upon removing and re-installing the corresponding SBCA. The

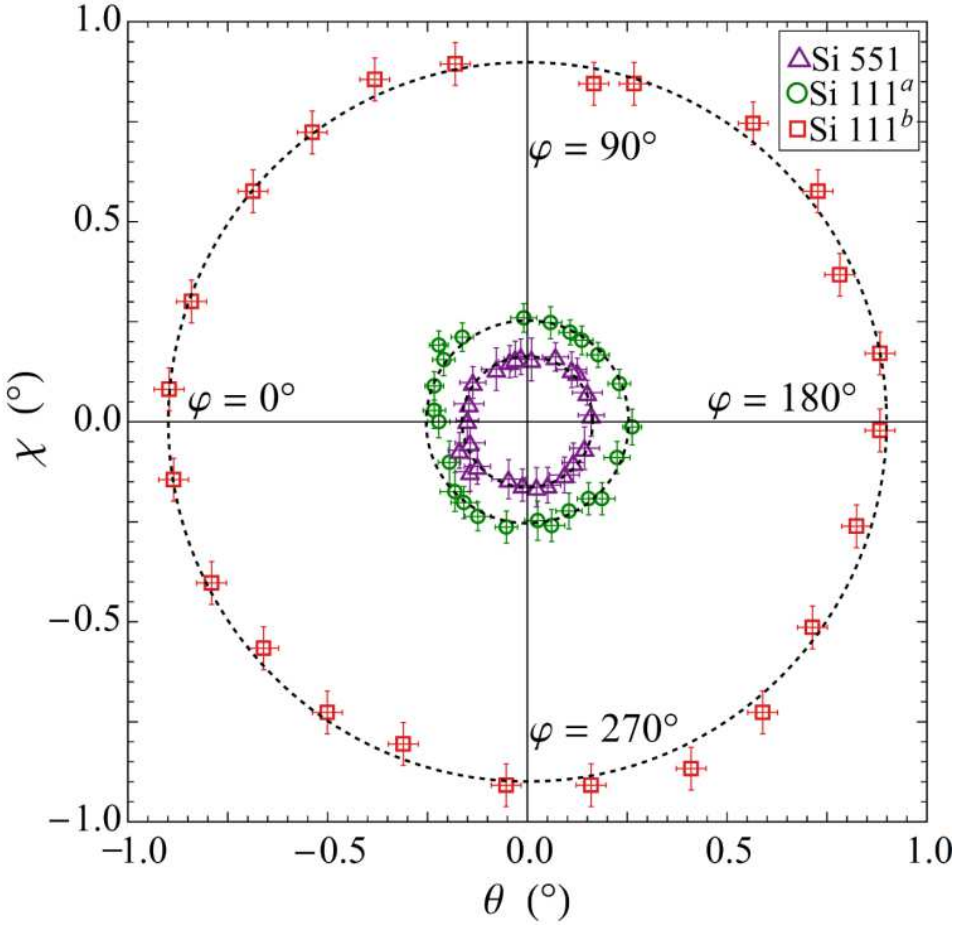

Figure 6.3. The θ and χ tilts of the refocused x-ray beam relative to the expected (optical) position. Tilts were determined by maximizing the Cu $K\alpha_2$ (Ni $K\beta_{1,3}$) signal for a Si 111 (Si 551) SBCA operating in the symmetric Rowland configuration. Data points were taken every 15° in φ. A clock angle, $\varphi = 0°$ corresponds to $\vec{G}_0$ oriented in the Rowland-plane tilted towards the source-side of the circle, 90° corresponds to $\vec{G}_0$ tilted out-of-plane upwards, etc. The black dotted lines show a circular fit to each dataset, revealing miscuts of 0.45 +/- 0.01°, 0.13 +/- 0.01°, and 0.081 +/- 0.002° accordingly.

detector is a solid-state Si drift detector (Amptek XR-123SDD) with a 5-mm diameter active area. The region of interest was set appropriately to reduce background signal.

The results are shown in Figure 6.3. Data were taken in incremental steps $\Delta\varphi = 15°$ with fiducial markings insuring accuracy to within +/- 1°. For this study the rotation was applied manually, though this could easily be replaced with a motorized stage if desired. For the Si 111 optics, the Cu $K\alpha_2$ line was used for alignment (80.1° Bragg angle at 444 reflection) while for Si 551, the Ni $K\beta_{1,3}$ emission (80.5° Bragg angle) was used. The data shows excellent agreement to the expected circular shape with extracted miscut values of 0.45 +/- 0.01°, 0.13 +/- 0.01°, and 0.081 +/- 0.002° accordingly.

In addition to the magnitude of the miscuts, their orientations are obtained by careful note of the clock angle associated with each set of (θ, χ) values. The convention for clock angle is as follows: 0° corresponds to $\vec{G}_0$ in the Rowland-plane and tilted towards the source-side of the circle; 90° corresponds to $\vec{G}_0$ tilted out-of-plane upwards, etc. (see Figure 6.3).

In Figure 6.4 we test the consequence of the SBCAs clock angle φ on the measured non-resonant Kβ emission spectrum of Ni metal. In each case the tilts have been adjusted as described above. All spectra presented in this study were collected at 15 seconds of integration per point in 0.1 eV steps. Here the resolution is dominated by the K-shell core-hole lifetime (1.44 eV) and we expect the difference between orthogonal orientations to be indistinguishable. Indeed the peak-normalized spectra are identical to within statistical noise. Furthermore, the count rates agree favorably with peak rates of 4270/s and 3990/s for in-plane ($\varphi = 0°$) and out-of-plane ($\varphi = 90°$) orientations respectively. These results indicate that for experiments that are intrinsically limited by core-hole broadening to ~1-eV or coarser resolution the SBCA performance after conventional alignment with a two-axis tilt is independent of clock angle.

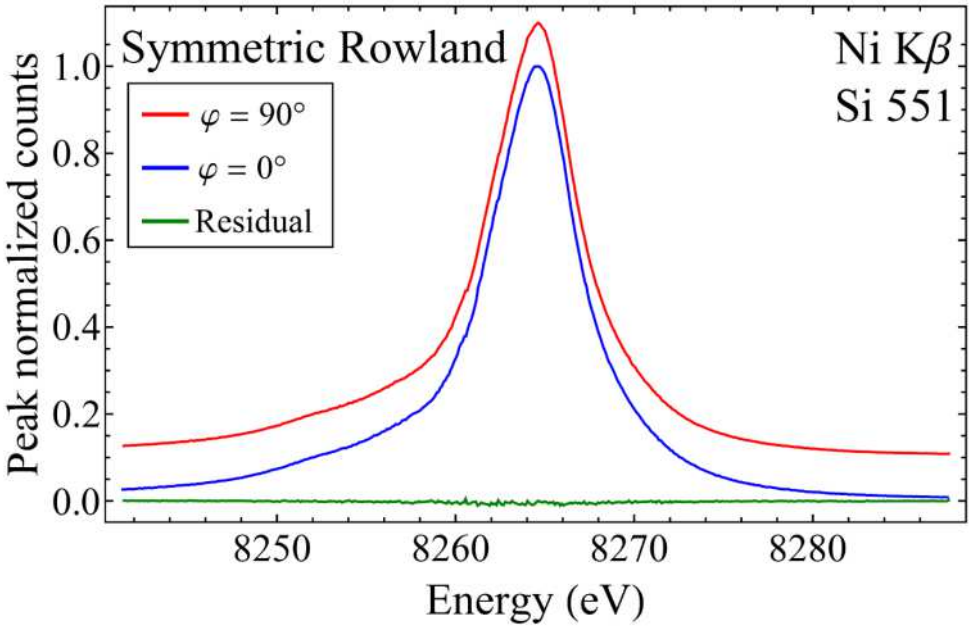

Figure 6.4. Peak normalized Ni Kβ spectra for an in-plane (φ = 0°) and out-of-plane (φ = 90°) orientation of $\vec{G}_0$ in the symmetric Rowland configuration. For clarity of presentation the first spectra has been offset as indicated. Unnormalized count rates were 4270/s and 3990/s at peak for 0° and 90° clock angle respectively. The two datasets agree so well as to be nearly indistinguishable – the green curve shows the residual between the two normalized spectra. Both spectra were collected at 15 seconds of integration per point in 0.1 eV steps.

Further investigation is required to determine if this advantage extends to ultra-high resolution (<100 meV) applications such as inelastic scattering experiments.

6.4 Asymmetric Rowland configuration

Armed with the above knowledge, we now investigate how the careful selection of the orientation of $\vec{G}_0$ can simplify overall instrument alignment and operations. As a first scenario, in the symmetric Rowland geometry the miscut can be chosen to be rotated either into or out of the

Rowland plane. Doing so removes the need for either, but not both of, the χ or θ adjustment, effectively reducing the required motorized degrees of freedom to a 1-D tilt, with obvious saving in both instrument cost and alignment time.

A second, more aggressive, approach is to eliminate two-axis fine tilt adjustments entirely. This can be realized by rotating $\vec{G}_0$ into the Rowland plane and offsetting the detector position to position D' as shown in the asymmetric Rowland configuration in Figure 6.2. The magnitude of the offset, ΔD, is determined geometrically to be

$$\Delta D = R \sin^2(\theta_B) \left[\cot(\theta_B - 2\alpha) - \cot(\theta_B)\right] \tag{6.2}$$

where R is the SBCA radius of curvature, θ_B is the expected Bragg angle absent any miscut, and α is the crystal miscut. In principle the detector offset is a function of $\theta_B$which is the exact parameter altered during an energy scan. However, for $\alpha/\theta_B \ll 1$, which is true for typically modest miscut and operation close to backscatter, eq. (6.2) reduces to

$$\Delta D \cong 2R\alpha + \mathcal{O}(\alpha/\theta_B)^2 \tag{6.3}$$

which is independent of θ_B. This constant offset approximation holds quite well over a wide range of Bragg angles. For example, for a 1-m curvature SBCA having 0.5° miscut the optimal detector offset as determined by eq. (6.2) is 17.5 mm at perfect backscatter and 17.6 mm at $\theta_B = 70°$. Thus any reasonably sized detector can be used in an energy scan without modifying the detector offset. While this approach will alter the energy calibration with respect to the perfectly symmetric case, this issue is addressed pragmatically by, e.g., measurement of reference standards, just as would be done with the usual experimental configuration.

This method, of course, hinges on orienting $\vec{G}_0$ into the Rowland plane which requires prior knowledge of the SBCA miscut. While the analyzer could first be characterized in a symmetric Rowland instrument with a two-axis tilt and then transferred to the fixed, asymmetric design, this

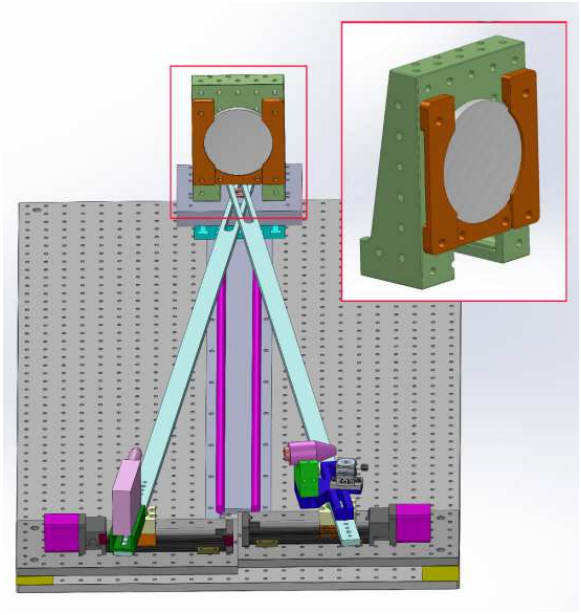

Figure 6.5. A perspective rendering of the University of Washington instrument modified to work in the asymmetric Rowland configuration. Inset: The new SBCA module where the two-axis tilt has been replaced with a rigid, right-angle bracket. The flat back of the SBCA lens is clamped flush to the bracket surface.

negates much of the intended benefits. We have therefore identified a related procedure for optimizing the orientation of the SBCA miscut entirely within an asymmetric Rowland geometry.

This is accomplished by measuring the count rate of a reference signal as a function of φ. Any out-of-plane tilt in $\vec{G}_0$ deflects the reflected beam out of the Rowland plane shown in Figure 6.2 and cannot be compensated for by the simple 1-D detector offset. For a finite sized detector, or a large detector constrained by appropriately sized entrance slits, the count rate will therefore be maximized when $\vec{G}_0$ is oriented in the Rowland plane. Once the maximum signal is found, a simple fiducial mark on the cylindrical exterior of the SBCAs lens-support allows for easy reproducibility, as we show below.

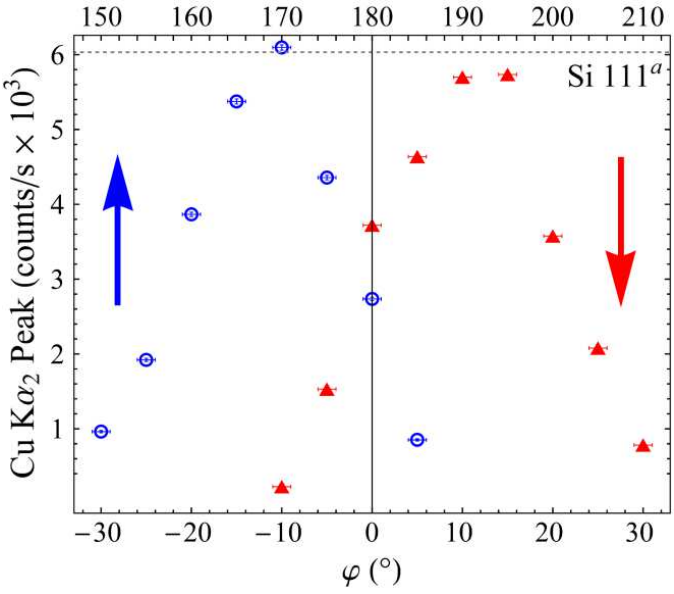

Figure 6.6. Maximum count rate as a function of clock angle for the asymmetric Rowland geometry. Cu Kα$_2$ emission was used as the reference signal measured by a 0.45°-miscut Si 111 (444 reflection) SBCA. Count rates are given as absolute peak counts/second. The horizontal dashed line indicates the counting rate achieved when employing the same analyzer in the symmetric Rowland configuration. The shift in the shape when the clock angle is rotated by 180° indicates a small error in the spectrometer design with the detector sitting slightly below the Rowland plane.

To test the efficacy of this proposed method, we modified the University of Washington instrument described in Section 6.3 (see Figure 6.5). Specifically we removed the two-axis tilt module and in its place installed a simple, rigid right-angle bracket, aligned and shimmed a single time with assistance of a laser and flat mirror to ensure correct placement with respect to the Rowland circle. The flat back of the SBCA lens-support is simply clamped flush to the face of this bracket as shown in the inset in Figure 6.5. The alignment procedure was carried out using the 0.45°-miscut Si 111 analyzer and Cu foil from Section 6.3. At each φ the detector

offset was scanned to find the maximum Cu $K\alpha_2$ signal as indicated in Figure 6.6. The shift in the shape when φ is rotated by 180° indicates a small error in our geometry with the detector sitting slightly below the Rowland plane. This, however, does not affect the maximum count rate, compared to the symmetric Rowland geometry, nor does it significantly degrade resolution as will be discussed in Section 6.5.

In addition to the reduction of mechanical components, this fixed bracket design allows for remounting of SBCAs with only minor irreproducibility in their position. Realignment is not needed. The proof of this claim is demonstrated in Figure 6.7. For each sample the SBCA miscut was rotated in-plane as discussed above. An initial detector scan (< 5 min) was performed to find the optimal offset and a spectrum was recorded. The sample and optic were then entirely removed. After performing other measurements with the spectrometer we then reinstalled the same sample/SBCA combinations and repeated the spectral scans using the same detector offsets and SBCA clock angles found previously (i.e., without any re-optimization scans). The agreement is excellent with only minor changes in the peak count rate (13600/s vs. 13400/s for Cu and 3200/s vs. 3920/s for Ni). The small discrepancy in intensity is most likely due to degradation of the He space over time. We stress that no relative shift has been applied between the initial and revisited spectra thus demonstrating a reproducible energy scale to ~50 meV without recalibration.

These demonstrated consequences of our implementation of the asymmetric Rowland configuration form the major results of this paper. Our design successfully removes all motorized tilt degrees of freedom, substantially easing instrument design and construction without degrading spectrometer performance (US Provisional Patent 62/271,992). Furthermore, the simplified alignment and robust reproducibility upon reinstalling SBCAs offers obvious benefits

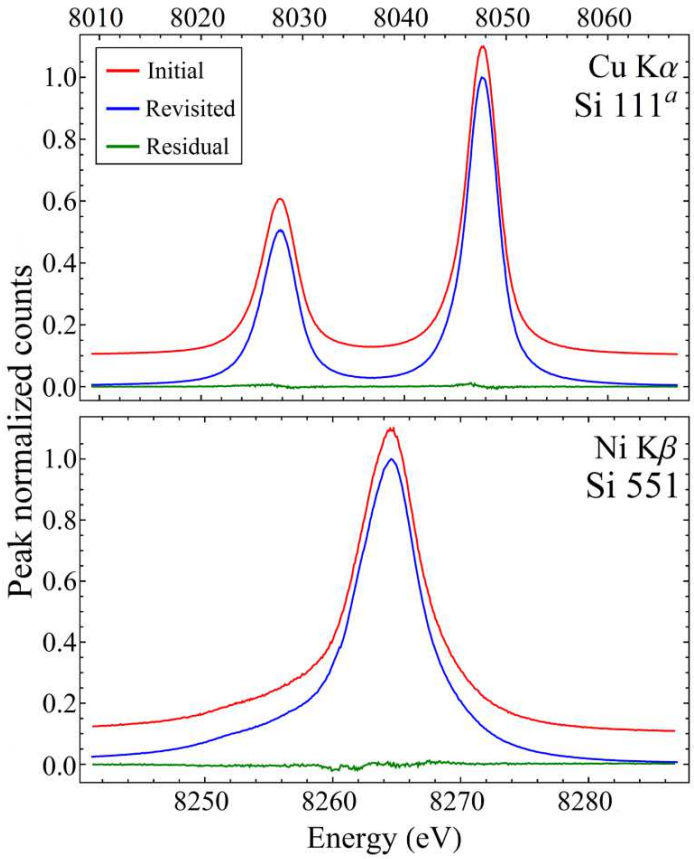

Figure 6.7. Peak normalized Cu Kα and Ni Kβ spectra recorded using the previously characterized Si 111 and Si 551 SBCAs in an asymmetric Rowland geometry. All spectra were collected at 15 seconds of integration per point in 0.1 eV steps. Spectra have been vertically offset for clarity. For each analyzer the clock angle was set at 180° to orient $\vec{G}_0$ into the Rowland plane. An initial detector scan was performed to find the optimal detector offset and a spectrum was recorded. The same sample/SBCA combinations were later revisited and spectral scans were rerecorded using the same clock angles and detector offsets found previously (i.e., without a re-optimization scan). The agreement is excellent with only small changes in the peak count rate (13600/s vs. 13400/s for Cu and 3200/s vs. 3920/s for Ni). No relative shift has been applied to the energy scales, which reproduce to within ~50 meV without recalibration.

in user operations and towards the study of dilute samples and/or weak emission lines where direct alignment is impractical due to lack of a strong signal. While the results have only addressed x-ray emission spectroscopy, they more broadly apply to any operation of a Rowland circle spectrometer using SBCAs, including when used as a monochromator for laboratory-based x-ray absorption fine structure (XAFS) [250, 258].

While the asymmetric Rowland configuration is most clearly applicable in single-SBCA systems, the pre-orientation of optics could also be useful in multi-analyzer spectrometers. Even when these designs require the use of one or more tilt axis, such as for direct energy scanning with theta, we have found that pre-determination of the clock angle of the miscut can greatly streamline SBCA alignment.

6.5 THE EFFECT OF WAFER MISCUT ON SBCA PERFORMANCE

Having established the importance of careful control of the orientation of the wafer miscut, before concluding we examine how the relative orientation of $\vec{G}$ affects overall instrument performance. We begin by addressing energy resolution. The factors limiting resolution of spherical analyzers fall into four main categories [261]: (1) intrinsic contributions from the crystal Darwin width and strains induced during the bending process; (2) the finite angular size of the source (or sample) as seen by the SBCA; (3) Johann errors due to only the center of the SBCA being on the Rowland circle; and (4) axially aberrations caused by the out-of-plane spherical bending being correct only at perfect backscatter. These factors are taken to be independent and therefore combine in quadrature to give the final instrument resolution. The latter three categories are purely geometric aspects and all affect energy resolution as $\cot(\theta_B)$. For this reason instruments requiring highest possible resolution are always designed to work at extreme backscatter geometries.

Of the factors listed above, Johann and axial errors are clearly the most sensitive to crystal miscut. Both are due to variation across the face of the analyzer in the angle between incident radiation and $\vec{G}$, i.e., the complementary Bragg angle. These geometric aberrations have long been understood and are well documented [52, 53]. Crystal miscut directly influences the direction of $\vec{G}$ and therefore requires a direct assessment in the context of Johann error.

Here we implement a method for calculating the combined Johann and miscut errors using ray tracing code in *Mathematica*. As the performance of SBCAs working in the symmetric Rowland configuration has been well-established experimentally, for brevity we present only results for the asymmetric geometry. This code calculates $\vec{G}$ at all points on the SBCA by first applying the miscut rotation to the lattice planes of a flat crystal and then bending its surface onto the partial analyzer "sphere". The incident Bragg angle is then mapped across the analyzer surface for a given source location. This gives the added functionality of being able to fold in the effects of finite source size so as to account for all the geometric factors limiting resolution. We do not consider the finite penetration of the x rays into the crystal bulk. While this is a primary energy-broadening mechanism far from backscatter, it is a minor effect for the angle ranges presented in this study. We furthermore consider the misorientation of $\vec{G}$ with respect to $\vec{n}$ to be coherent at every point, in that we ignore solid mechanics effects such as have been discussed in detail by Honkanen, et al. [262]

We emphasize that this ray tracing considers only geometric effects assuming perfect Bragg surfaces. In practice the elastic bending of flat wafers introduces crystals strains. These defects, which vary from optic to optic, are non-trivial and can modify the rocking curve and refocused shape significantly. Nonetheless, such strain-induced effects are independent of $\vec{G}$ orientation and the following discussion gives valuable insight into the effects of crystal miscut.

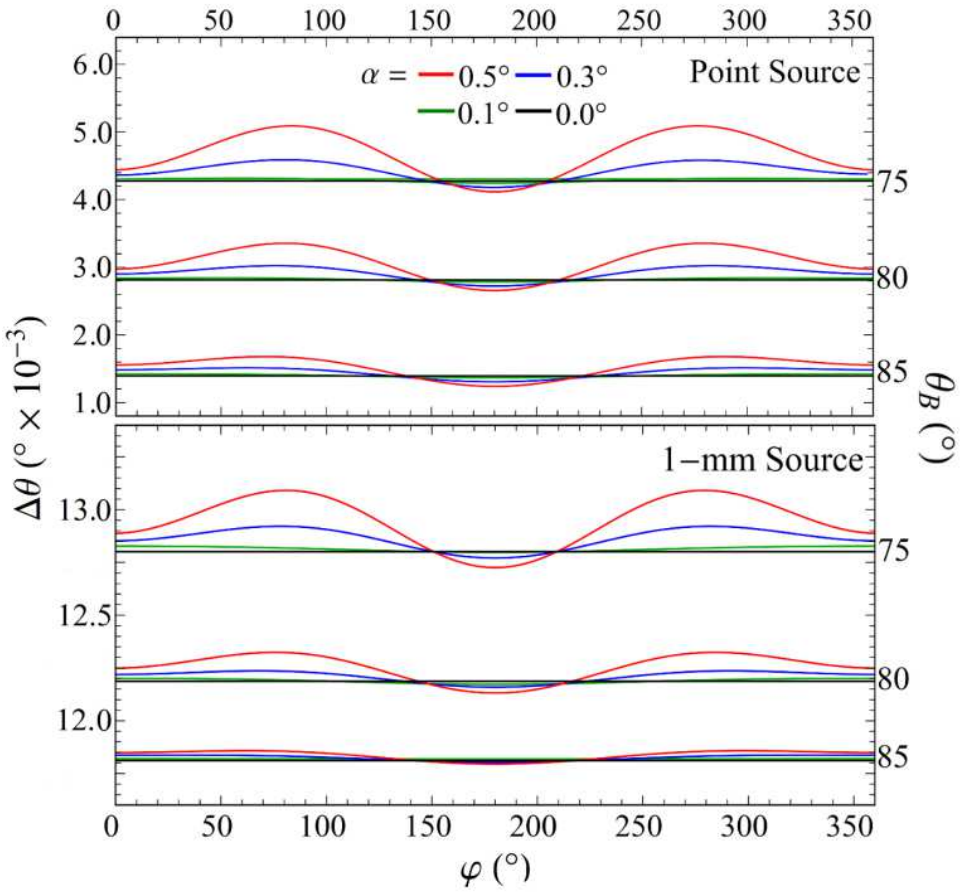

Figure 6.8. The angular spread due to combined geometric errors for both a point (top) and 1-mm diameter (bottom) source size as a function of clock angle for several miscut magnitudes. The analyzer is taken to be a 100-mm diameter SBCA with 1-m radius of curvature. A clock angle of 0° corresponds to $\vec{G}_0$ oriented in the Rowland-plane tilted towards the source-side of the circle, 90° corresponds to $\vec{G}_0$ tilted out-of-plane upwards, etc. A clock angle of φ = 180° is shown to minimize $\Delta\theta$ at all θ_B and miscut magnitudes α.

Calculations were run at several Bragg angles and miscut magnitudes for both a point source and 1-mm diameter source size. When introducing miscut, the central source location is adjusted along the Rowland circle such that the Bragg angle at the SBCA center is constant, allowing for a functionally correct assessment of the consequences of miscut. To ensure reasonable

computation times we employ a stochastic approach where an x-ray generated from a random point in the source area strikes a random point on the SBCA. This process is repeated many thousands of times.

The effective angular spread of the incident rays on the SBCA is shown in Figure 6.8, where we have assumed the standard 100-mm diameter wafer bent to 1-m radius of curvature. Calculations were also run for the pristine case (i.e., zero miscut) in order to provide a fair distinction between contributing errors. We have defined the figure of merit, $\Delta\theta$, to be the root mean square deviation from the desired θ_B of the actual incident Bragg angles across the SBCA surface.

As expected, the effect of crystal miscut varies with φ and becomes more severe when θ_B is further from backscatter. For modest miscuts and Bragg angles close to backscattering, the magnitude of this modulation is at most a factor of ~0.25 compared to the other geometric effects and occurs when $\vec{G}_0$ is oriented out-of-plane. Most importantly, our calculations show that the contribution from crystal miscut can be negated by proper choice of φ. Interestingly, we find that for $\varphi = 180°$ ($\vec{G}_0$ in-plane slanted towards the detector) the angular spread is actually improved upon by the addition of miscut. This is somewhat unexpected but is due to our allowance for movement in source position. At $\varphi = 180°$ the source location required to achieve an equivalent Bragg angle is closer to the nominal backscatter location which in part lessens the geometric aberrations discussed above.

One of the major benefits of SBCAs is their ability to refocus the analyzed radiation onto a small spot, allowing for the use of smaller-area detectors and also providing outstanding geometric rejection of stray scatter, hence it is important to determine the influence of wafer miscut on the SBCA exit focus . We again use the ray-tracing code discussed above. With $\vec{G}$

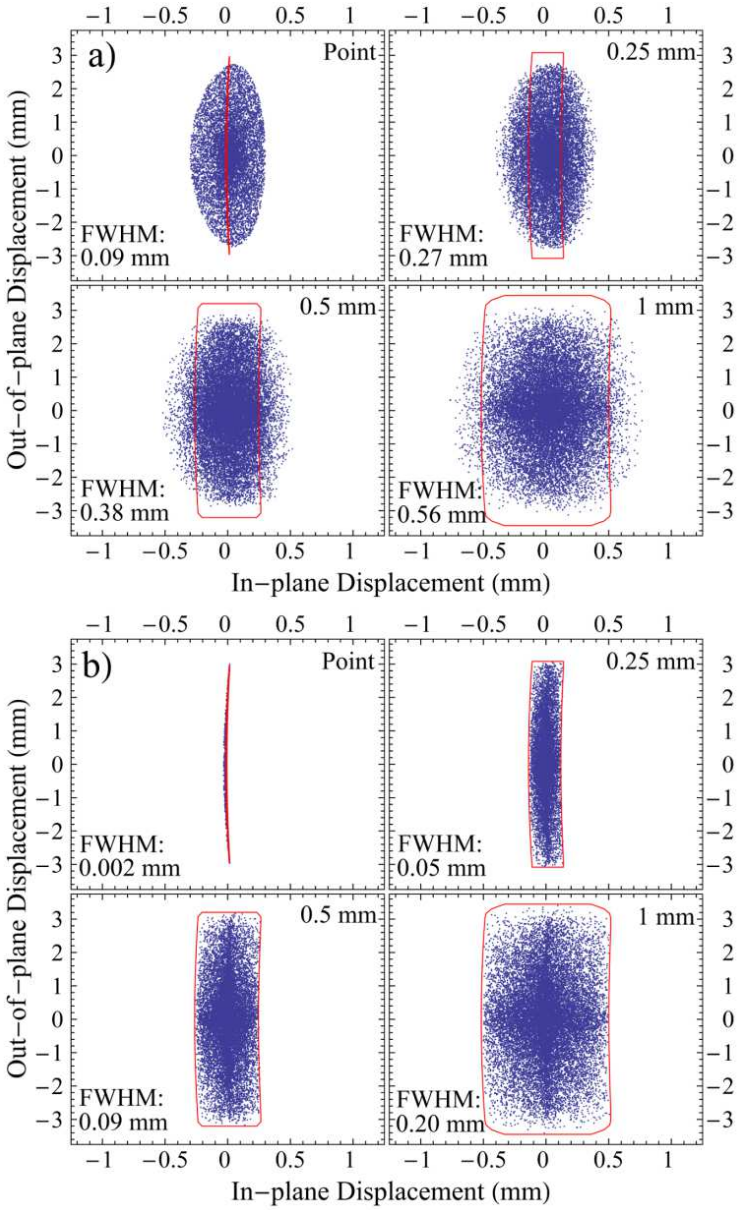

Figure 6.9. The relative refocused positions on the detector face for randomly generated rays. A 100-mm diameter SBCA with 1-m radius of curvature and 0.5° miscut, oriented at $\varphi = 180°$, working at 80° Bragg angle was assumed. Results are shown for several different source-size diameters at two different detector constraints: a) the center of the detector lies on the line determined by the x-axis of the source/sample (D' in Figure 6.2); b) the detector face is tangent to the Rowland circle (D'' in Figure 6.2). In either case the out-of-plane spread is dominate and comparable to the zero-miscut results (shown in red).

being known across the analyzer surface the reflected ray is determined and traced back to a specified detector plane. Again the penetration of x rays into the crystal before reflection is not accounted for. These penetration depths, however, are small on the scale of the total travel distance and thus do not significantly affect the refocused position.

In Figure 6.9 we present ray tracing results for several source-size diameters. A 100-mm diameter SBCA with 1-m radius of curvature and 0.5° miscut, oriented at 180° clock-angle, working at 80° Bragg angle was assumed. Results are shown for two different detector constraints. In Figure 6.9a the detector center is constrained to lie along the x-axis of the source (position D' in Figure 6.2). We also present the case in Figure 6.9b where the detector face lies tangent to the Rowland circle (position D'') to demonstrate that focusing is recovered.

For comparison we overlay the shape of the full refocused beam for a pristine analyzer (red line). From these plots we see that in-plane focusing is strongly influenced by miscut orientation. The same is not true of the out-of-plane displacement where the increase from the pristine case, in which the spread is due to approximated spherical bending, is minimal. The out-of-plane spread, however, is dominant in magnitude compared to the in-plane direction even when working at the slightly off-circle position. The same considerations for detector size are thus clearly present regardless of miscut.

As a final test of spectrometer performance in the asymmetric Rowland configuration we present in Figure 6.10 a comparison of a Ni Kβ emission spectrum taken in the asymmetric configuration without a two-axis tilt to a Ni Kβ emission spectrum instead recorded in the symmetric Rowland geometry which incorporates the two-axis tilt. After correcting for the energy shift caused by detector offset, the two setups produce nearly identical resolutions and count rates (4270/s for the symmetric configuration and 3920/s for the asymmetric). This result,

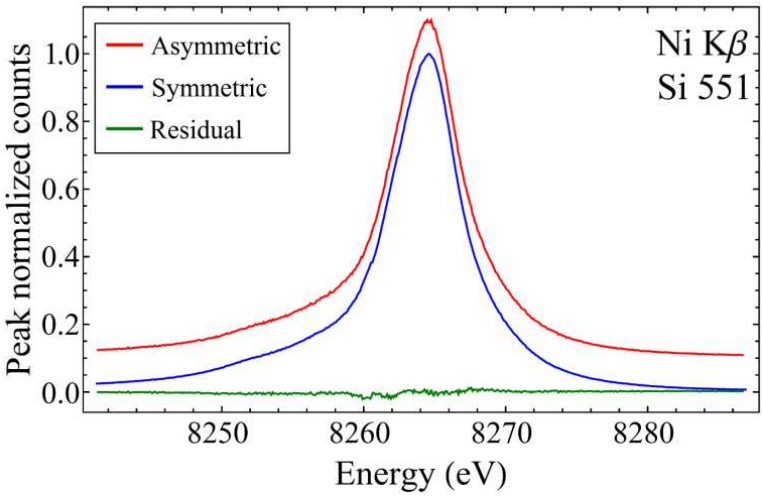

Figure 6.10. A comparison of peak normalized Ni Kβ spectra collected with both symmetric and asymmetric correction Rowland geometries. For clarity of presentation the second spectra has been offset as indicated. The two datasets show near perfect agreement. The green curve shows the residual between the normalized spectra. Absolute peak count rates are 4270/s for the symmetric configuration and 3920/s for the asymmetric. Both spectra were collected at 15 seconds of integration per point in 0.1 eV steps.

combined with the analysis above, validates the asymmetric design by showing that the motorized tilt degrees of freedom can be removed without detriment to data quality for nonresonant XES using SBCAs relatively near to backscatter.

6.6 Conclusion

In summary, we propose and demonstrate that the ubiquitous two-axis tilt assembly used to align SBCAs can be eliminated by careful orientation of wafer miscut in an asymmetric Rowland geometry. This scheme delivers equivalent performance to the typical symmetric Rowland configuration when working near backscatter while providing clear benefits to instrument design,

maintenance, and operations. We show that this design simplifies SBCA initial alignment while also providing extremely reproducible positioning upon reinstallation. We hope that the streamlined and singly-required alignment procedure of the asymmetric Rowland configuration lower the technical barrier to further implementations of lab-based advanced x-ray spectroscopy using SBCAs.

Chapter 7. VALENCE-TO-CORE X-RAY EMISSION: PAST LESSONS AND FUTURE DIRECTIONS

7.1 THE HISTORY OF X-RAY ABSORPTION SPECTROSCOPY

In the current landscape, the field of x-ray absorption spectroscopy (XAS) occupies a position of broad scientific scope and technological importance. This footing, however, was not easily achieved. While the roots of XAS extend back to the first observations by de Broglie in 1913,[263] the first 60 years of its life was spent as a topic of fundamental research with limited opportunity for application. It was not until the 1970s, with the establishment of several electron storage rings for dedicated synchrotron radiation experiments,[264-266] that XAS became a methodology with steadily growing reliability, availability and, especially, breadth of impact. Since that time a tremendous amount of work and resources have gone into building synchrotron lightsources, and more recently x-ray free electron lasers, around the world.[267-269]

The theoretical understanding of XAS has been similarly fraught. Settling the central conceptual issue of the *locality* of the interrogated density of states was a nearly 50 year battle.[270] The discovery of the 'EXAFS equation',[271] effectively casting the extended absorption oscillations as a single- or few-scattering process, was merely the first shot which launched several decades of work in finding optimal descriptions of the phase shifts due to atomic and inter-atomic potentials.[272-281] The establishment of reliable theoretical predictions and interpretations for oscillations in the main body of the near-edge fine structure required, first, a simplified computational framework for the influence of full-multiple scattering and, second, a careful treatment of core-hole effects.[270] While a number of these issues have been settled, others are still matters of contemporary research. Chief among these is the interpretation of pre-edge

features, especially those coupled to charge-transfer effects or other dynamical rearrangement of charge density that go beyond 'typical' excitonic effects induced by the core-hole potential.[282-288]

The history of XAS hence represents a clear example of a reoccurring lesson in science: the growth of any analytical method requires parallel development in each of instrument technology, cross-technique validation, and theory. Indeed, due to the lack in each of the prior three criteria, few could have seriously imagined in the early 1970s that XAS would evolve to the point where it is now routinely used to solve forefront problems in metallorganic chemistry or that it would become a work-horse for industrial and fundamental research in catalysis[172-192, 289-297] and electrical energy storage,[150-171, 198-201, 203-206, 209-214, 298-302] to name only a few prominent examples.

7.2 THE PRESENT STATE OF X-RAY EMISSION SPECTROSCOPY

Following in the technical and, to a growing extent, historical footsteps of XAS, x-ray emission spectroscopy (XES) has over the past few years emerged as an important new spectroscopic tool, spreading from the realm of fundamental condensed matter science to, e.g., applications in catalysis,[28, 106-110, 296] electrochemistry,[303-305] biological sciences.[21-24, 33, 35, 116] While the semi-core and deeper core transitions involved in XES are often reasonably well described by atomic multiplet approaches due to the extreme localization of the atomic-like initial and final states, the situation is markedly less clear for those transitions involving valence electron density of the host species or ligands.

As the name suggests, this valence-to-core (VTC) x-ray emission involves the filling of a deep core-hole via de-excitation of valence-level electronic states. The valence orbitals, with energies within a few eV of the Fermi level, are the most sensitive to the chemical environment and therefore VTC-XES has much greater sensitivity to local coordination effects than do diagram

lines involving only deeper core shells. While there are various other chemical spectroscopy techniques (e.g., x-ray photoemission, x-ray absorption, Raman, *etc.*), there exist a number of fine issues of local structure that are best addressed through VTC-XES. A recent, well-known example is the identification the central atom in the nitrogenase iron-molybdenum cofactor central dinitrogen reduction in biological and industrial catalysis.[110] From the most general perspective, VTC-XES should be viewed as a natural complement to the pre-edge and white-line regions of XAS, in that VTC-XES is sensitive to the occupied, rather than unoccupied, states. At the same time, VTC-XES comes with a certain advantage in that, due to the final-state rule, theoretical treatment of VTC-XES may be somewhat simplified because of the absence of a core hole after emission.

Again, following the developmental history of XAFS, and all other modern spectroscopies, when the applications and demands of VTC-XES expand, so too must the supporting infrastructure in experimental apparatus and methodology and *validation* of theory. While the early stages of growth in XES have benefitted from the pioneering work conducted at several synchrotron end-stations,[23, 24, 32, 63, 64, 245, 249] the relative scarcity of these dedicated beamlines is a serious hurdle to routine application. In Chapters 4-6 of this dissertation, we have documented progress made in the development and refinement of laboratory-based instruments for XES studies. Here, using this equipment at the University of Washington, we present a high-quality VTC dataset of several inorganic Fe and Zn compounds. These compounds provide an interesting range of local electronic and atomic structure while retaining sufficient structural simplicity such that theoretical treatment should not, *a priori*, be challenged by material complexity.

To date, the most successful models are those based on density functional theory (DFT). Different implementations, however, often differ in significant ways (treatment of electron exchange-correlation, basis sets, real vs. reciprocal space, inclusion of relativistic effects, etc.). We therefore present a critical assessment of several state-of-the-art DFT-based electronic structure codes in the context of this new experimental dataset. Though the proper choice of theoretical method may vary from application to application, the present investigation will establish a base-level identification of strengths and limitations of the various approaches.

We note that we are not the first to seek a better understanding of the validity of theory in order to expand the range of application of VTC-XES. In recent years, the DeBeer group and collaborators have embarked upon a course of study aimed at establishing the information content available in VTC-XES of complex molecular inorganic systems.[28, 35, 106-110] Here the ultimate goal has been the use of DFT to develop an understanding of chemical information in a molecular orbital framework. In Section 7.6.3, we compare and contrast this theoretical work to our own conducted in the present study.

7.3 Laboratory-based VTC-XES

Although VTC features were first observed in the laboratory as early as the mid-1930s,[306-308] it is only in recent years that laboratory-based equipment has been employed in chemical studies.[86] Here we employed a Rowland-circle spectrometer developed at the University of Washington.[250, 258, 259] Despite using at most only 10 W of total electron beam power in the x-ray tube, this instrument achieves count rates and resolutions comparable to those of monochromatized bending magnet beamlines at third-generation synchrotrons. This impressive performance is due to the fact that non-resonant XES does not require monochromatic input; at energies sufficiently above the binding edge, the spectral shape is independent of the exciting energy.[127] As such, each

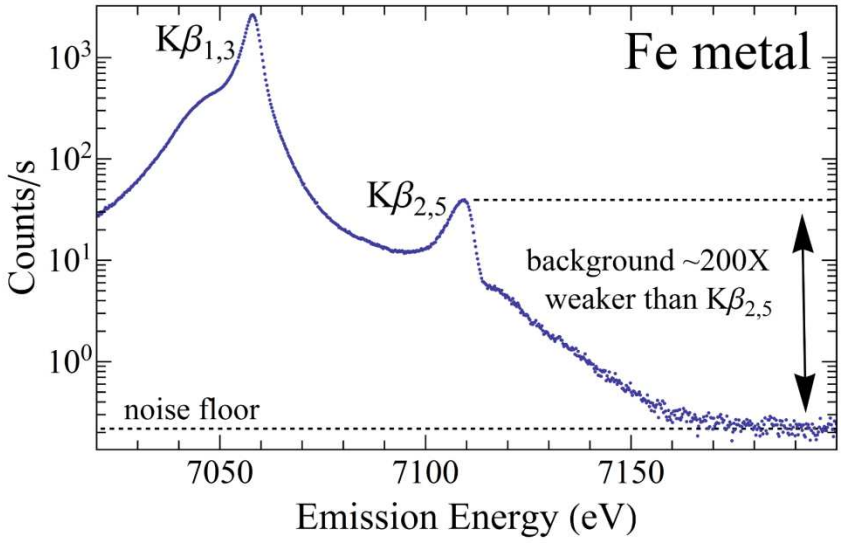

Figure 7.1. A representative Kβ spectrum for Fe metal. Data is extended well above the Fe K-edge (7112 eV) to identify the noise floor. From these measurements we see the background counts (~0.2/s) are 200 x times below than the weak $K\beta_{2,5}$ VTC feature.

fluorescence or bremsstrahlung x-ray photon having energy above the desired core-electron binding energy can stimulate emission.

In addition to excellent count rate, this instrument has several key features advantageous in recording high-quality XES data. First, as has been emphasized elsewhere,[250] the small sample-to-anode distance (~3 mm) results in high solid angle collection while maintaining a small illuminated sample area such as is important for preserving energy resolution. Consequently, a very high flux is achieved even for modest beam power.

Second, the refocusing Johann geometry[47] combined with an energy-resolving, solid-state detector for rejection of harmonics results in ultra-low backgrounds. For example, in Figure 7.1 we demonstrate that the noise floor is a factor of ~200 below the very weak VTC $K\beta_{2,5}$ line in metallic Fe.

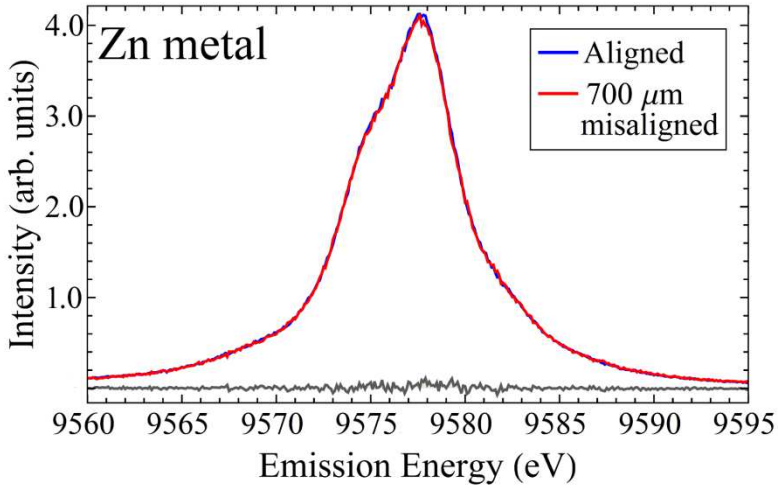

Figure 7.2. Normalized Zn $K\beta_{1,3}$ spectra at the optimal and an extreme misaligned (700 μm) sample location. Also shown is the residual intensity between the two curves (gray line). In this absence of the on-circle, 0.5-mm wide entrance slit, this misalignment would correspond to a relative shift of ~900 meV. Here, the two spectra agree so well as to be nearly indistinguishable.

Third, this instrumentation has demonstrated very high precision in the reproducibility of energy scale between samples, see Figure 7.2. As small shifts in the location of emission features is indicative of changes in chemical state, this robust energy scale is of critical importance to the theoretical comparison presented later in this chapter. This is accomplished by constraining line-of-sight between sample and analyzer with a fixed, on-circle entrance slit (0.5 mm width). This addition removes the sensitivity of the energy scale to small, lateral shifts in the sample location, such as is practically unavoidable when switching between samples. The full details of this method can be read elsewhere,[259] including Chapter 5 of this dissertation. Based on those methods, we estimate a consistent to within 25 meV for all spectra in the present study.

7.4 EXPERIMENTAL DETAILS

All samples for this study were prepared from high purity powders (99.9% or better) from Sigma Aldrich or Alfa Aesar, the exception being the Zn and Fe metal samples which were foils (99.9%) from ESPI Metals. The XES spectrometer has been discussed in detail elsewhere.[250, 259] Briefly, sample fluorescence was stimulated sample via output from an Au-anode, commercial x-ray tube (MOXTEK, Inc.) operated at 40 kV bias and 200 μA current. Sample fluorescence was analyzed using 10-cm diameter, spherically bent Ge (555) and Ge (620) crystals for Zn and Fe respectively, each with a 1-m radius of curvature (XRS Tech, LLC). Analyzed x-rays are detected with a silicon drift detector (Amptek, Inc.), and a region of interest of a few hundred eV was set to strongly reject background signal. Data was recorded in 0.25-eV steps with 30-50 s of integration per point in the $K\beta_{1,3}$ region and 100-160 s/point for the VTC.

We note that the spectral resolution is poorer for the Fe compounds than it is for Zn (where it is close to core-hole limited). We believe this result stems from defects in the Ge (620) optic leading to increased bandwidth. Nonetheless, the performance is sufficient to cleanly resolve key features in the VTC spectra.

As DFT can be ill-equipped to model the core-to-core $K\beta_{1,3}$ emission, due to difficulties in correctly estimate 3p-3d splitting, the intensity contribution of these lines are typically subtracted out in the valence region for comparison of theory to experiment. To this end, each full spectrum was fit to a series of pseudo-Voigt functions and a constant background using the *Blueprint XAS* package.[309, 310] In addition to the main $K\beta_{1,3}$ and valence features, we include extra curves to model the multi-electron excitation peaks (KLβ) above the Fermi-level[96-98] and the radiative Auger satellites[98] in the intermediate area as such features are not accounted for in the base theories. For the Zn spectra an additional pseudo-Voigt function is included to model the

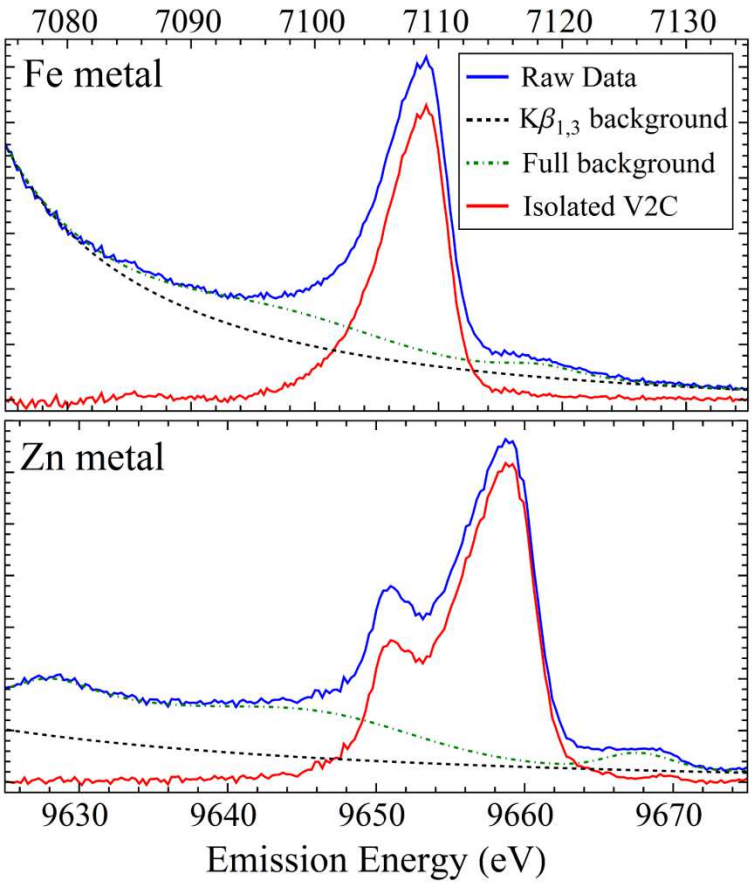

Figure 7.3. The raw (blue) and isolated (red) spectra for Fe and Zn metal VTC spectra. Each full Kβ spectra is fit to a series of pseudo-Voigt functions and the contributions from the $K\beta_{1,3}$ lines (dashed black), elastic scatter, radiative Auger emission, and multi-electron excitations are removed to isolate the VTC features. These background contributions are shown collectively as the dashed-green lines.

elastically scattered Au $L\alpha_2$ line originating from the tube anode. The width and position of this curve was constrained to be consistent across all samples. To emphasize the valence region in fitting, it was assigned a weighting of 6:1 relative to the $K\beta_{1,3}$. Representative results of this procedure are shown for Fe and Zn metals in Figure 7.3.

7.5 THEORETICAL DETAILS

We perform calculations using three state-of-the-art, *ab intio* electronic structure packages: Quantum ESPRESSO,[133] FEFF,[141] and NWChem.[147] At the time of publishing this dissertation, NWChem calculations have been performed only for the Zn samples. While each of these codes has a basis in DFT, they are built around distinct treatments leading to unique calculations as we will discuss in Section 7.6. We briefly discuss the methodology for each implementation below.

7.5.1 QUANTUM ESPRESSO

Calculations were performed within the generalized gradient approximation-DFT framework using ultra-soft pseudo potential with 125 Ry energy cutoff implemented in the Quantum ESPRESSO (QE) package with adequate k-point sampling for convergence with the PBE correlation and exchange.[133, 311] We calculate the off-resonant SXE spectrum assuming the 'final-state rule' which assumes a filled core-hole and a screened valence-hole. The spectra calculated here consider only dipole contributions to the transitions and are thus due to p-type projection of the density of states (DOS). To simulate the natural core-hole lifetime broadening and experimental resolution, the calculated stick spectra were Lorentzian broadened by 6.0 eV and 2.5 eV for Fe and Zn respectively. Each spectrum was then shifted independently in energy to align with experiment. It should be noted that the calculated spectral widths tend to be unphysically compressed due to the well-known problem of DFT underestimating the band gap.[312]

7.5.2 FEFF

Theoretical spectra were simulated using a full multiple scattering method implemented within the FEFF 9.6 code.[141, 313] The potentials were calculated self-consistently using a 5.0 Å cluster.

The spectra were calculated using a full multiple scattering radius of 6.0 Å. The initial core-state energy levels were calculated using the final self-consistent potential. This modification is intended to provide more accurate relative chemical shifts, although the results were somewhat inconsistent as we will discuss in Section 7.6. Here, both electric dipole and quadrupole transitions were included. Following the standard practice for XES, these calculations were performed with no core-hole. For comparison to experiment, these results were convolved with a Lorentzian (4.5 eV for Fe and 0.5 eV for Zn) and shifted independently in energy to match experiment. FEFF also includes calculations for the main $K\beta_{1,3}$ lines, but these contributions have been removed for the sake of comparison.

7.5.3 NWCHEM

The VTC-XES approach in NWChem is based on linear-response time-dependent density functional theory (LR-TDDFT).[314] First a neutral ground state calculation is performed, a full core hole (FCH) ionized state is then obtained self-consistently where the 1s core orbital of the transition metal (TM) absorption center is swapped with a virtual orbital combined with the maximum overlap constraint to prevent core hole collapse. A LR-TDDFT calculation, within the Tamm-Dancoff approximation (TDA), is then performed with the FCH reference state to simulate the VTC emission process. This approach allows one to go beyond the single-particle picture as all orbital pairs with significant contributions to the emission process are included naturally. To describe excitations beyond the dipole approximation, higher-order contributions are included in the calculation of the oscillator strengths.

All systems were represented with finite clusters constructed from crystal structures obtained from experiment. The Los Alamos effective core potential (LANL2DZ)[315-318] and associated basis sets were used for all the atoms (Zn, Cl, S, O) except the Zn absorbing center in each

system which was represented with the Sapporo-TZP-2012[319] full potential all electron basis set. The PBE0 exchange-correlation functional[320] was used for all calculations. For comparison to experiment, each calculated spectrum was convolved with a 2.0 eV Lorentzian and energy shifted. We note that, in contrast to the QE and FEFF results, this shift was constant across all samples indicating an accurate accounting for chemical shifts.

7.6 RESULTS AND DISCUSSION

Before we delve into a comparison of the various theories in great detail, it is important to note the existence of self-absorption effects in the experimental data. As shown in Figure 7.4, the $K\beta_{2,5}$ emission peak often straddles the rising K-edge. This creates an important systematic effect in thick samples; fluorescence above the absorption edge is preferentially quenched when escaping outward from the sample bulk. Due to the fine structure modulations in absorption, and in some cases strong pre-edge features, this effect often distorts spectral shape in significant ways. As an example, self-absorption causes the apparent asymmetry in the $K\beta_{2,5}$ peak of Fe shown in Figure 7.4.

In principle, sample self-absorption is correctable if the absorption coefficient, as measured in x-ray absorption spectroscopy, and sample thickness are known. An accurate correction, however, requires high precision in the relative energy scale between emission and absorption measurements. This is highly nontrivial as different instrumental setups are required for each type of measurement, and we do not attempt a correction for the data presented in this study. As such, we only consider the performance of our calculations only below the nominal edge energies (7112 eV for Fe and 9659 eV for Zn).

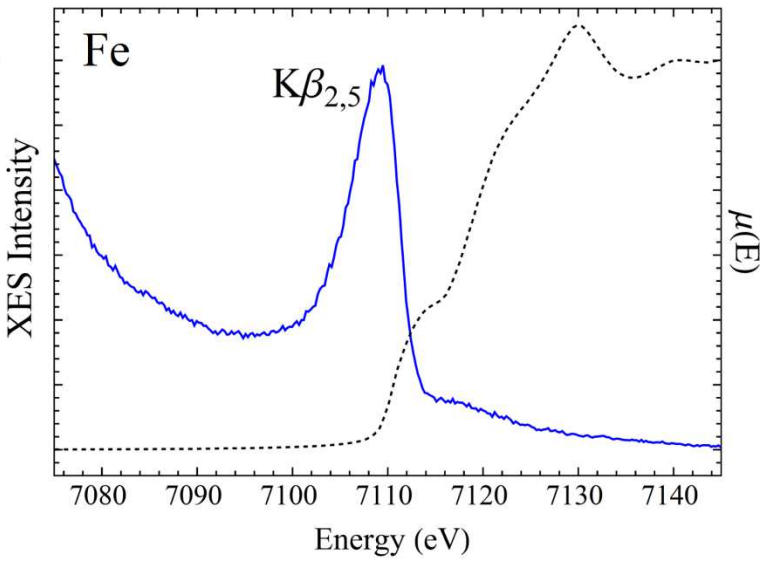

Figure 7.4. The VTC emission (solid, blue) and absorption coefficient (dashed, black), $\mu(E)$, of metallic Fe. Here the $K\beta_{2,5}$ emission feature straddles the rising K-edge absorption resulting in distortions in the spectral shape.

7.6.1 IRON-RICH SAMPLES

With this in mind we present the results for several Fe-rich samples in Figure 7.5. Overall, we see good reproduction of the experiment by both theories. We note that the QE and FEFF calculations produce similar spectra with nearly identical splitting between the $K\beta_{2,5}$ and $K\beta''$ peaks, the latter being a cross-over feature originating from ligand orbital with metal-p character. The magnitude of this splitting, however, appears to be slightly underestimated especially in the case of Fe_2O_3 and Fe_3O_4. Such a compression is a well-known problem in DFT, arising from difficulties in correctly predicting the band gap.[312] In the case of FeS, QE misses the cross-over peak entirely, which we believe to be an issue of the DFT misidentifying the character of the

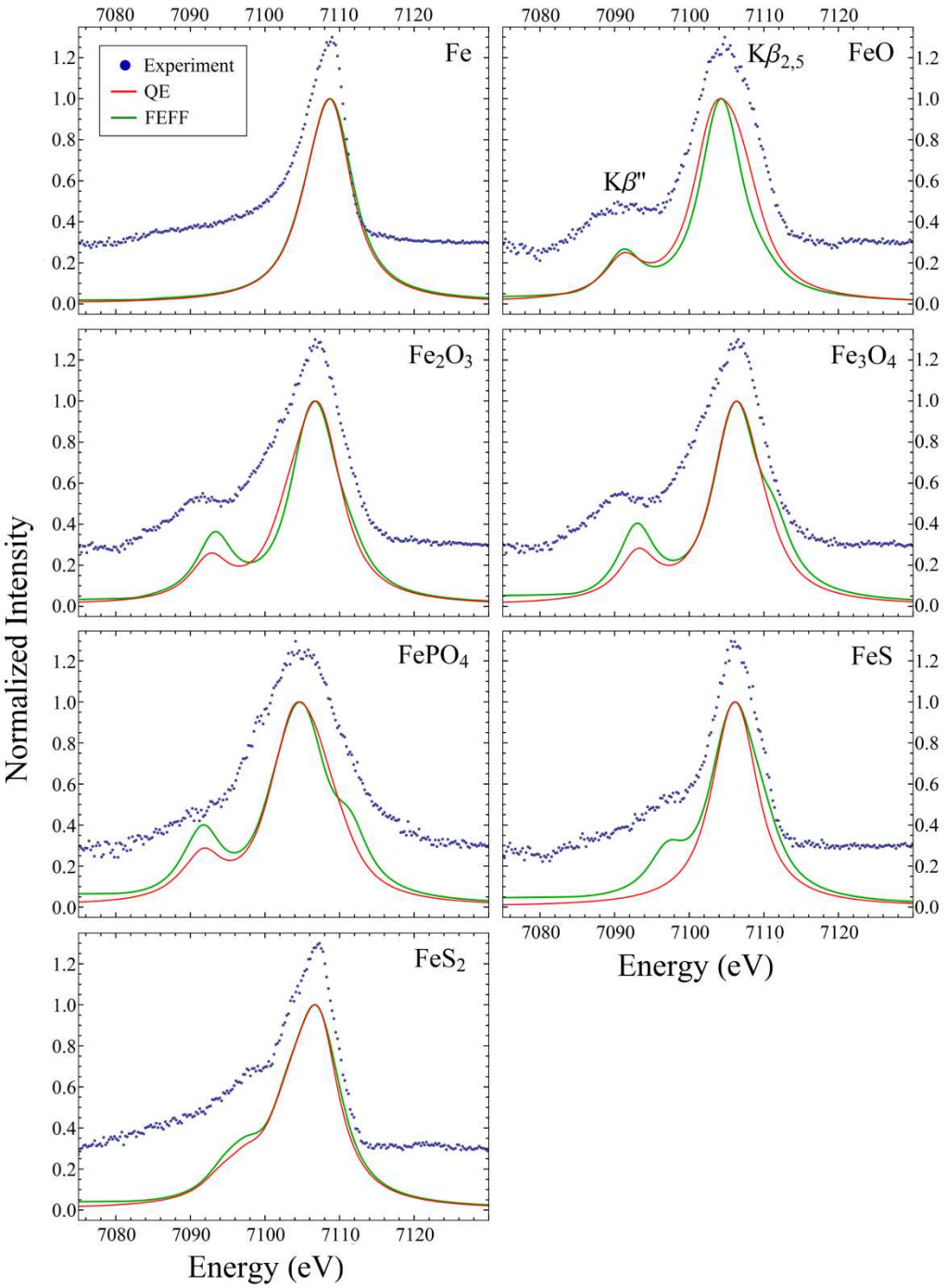

Figure 7.5. Experimental (blue dots) and calculated Quantum ESPRESSO (red) and FEFF (green) valence-to-core spectra for various Fe compounds. For comparison, the theoretical results have been broadened as described in the text and shifted to align with the main peak. Experimental data has been offset as indicated.

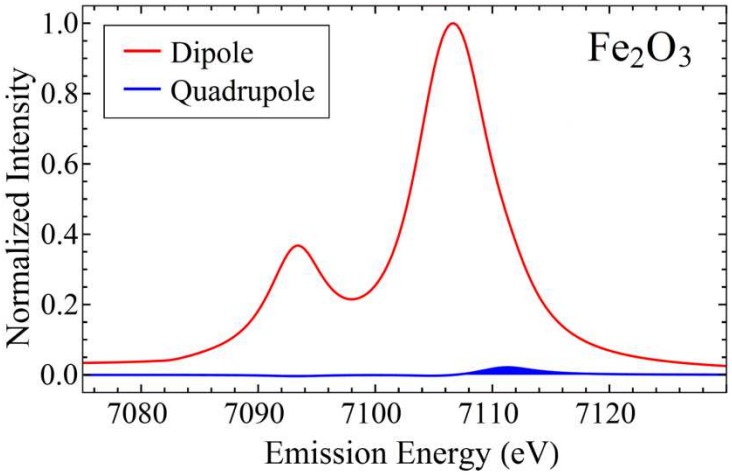

Figure 7.6. The dipole (red) and quadrupole (blue) contributions to the FEFF calculation for Fe_2O_3. For emphasis, the quadrupole term is shown with filling to the axis.

state. In general the intensity of this feature tends to be under-predicted with respect to FEFF.

As FEFF contains electric dipole and quadrupole terms in calculation, its close agreement with QE is suggestive of only very weak quadrupole contributions. In Figure 7.6, we present a separation of each term in the FEFF output for Fe_2O_3, confirming this assertion. The intensity of the quadrupole features is similarly negligible across all Fe-rich samples. As we will discuss in Section 7.6.2, for some compounds the quadrupole term can be quite significant and therefore the determination of which terms to include in calculation must be considered on a sample-to-sample basis.

Again, we stress that the required energies shifts to align calculation with experiment are inconsistent across samples, with a relative spread 3.5 eV and 10.6 eV for QE and FEFF respectively. As seen from this dataset the relative positioning of VTC features is not fixed, with real, physical shifts occurring due to changes in chemical state, particularly oxidation. This

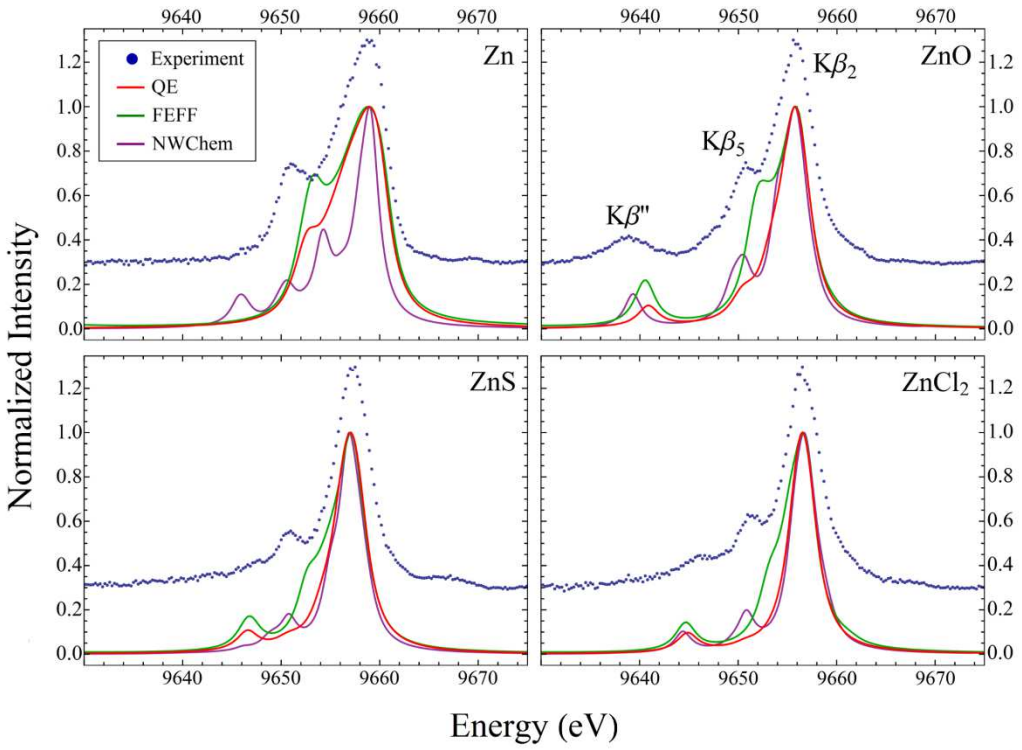

Figure 7.7. Experimental (blue dots) and calculated Quantum ESPRESSO (red), FEFF (green), and NWChem (purple) valence-to-core spectra for various Zn compounds. For comparison, the theoretical results have been broadened as described in the text and shifted to align with the main peak. Experimental data has been offset as indicated.

deficiency is therefore a topic that must be addressed in order to establish a robust, *ab initio* interpretation of experimental spectra.

7.6.2 Zn-rich samples

The Zn compound results are shown in Figure 7.7. We see that the VTC region differs from that of the Fe samples in significant ways, chief of which is a now resolvable splitting between the $K\beta_2$ and $K\beta_5$ lines. In Fe, and indeed most 3d-transition metals, these two features are indistinct due to core hole broadening and are thus referred to together as $K\beta_{2,5}$. The origins of

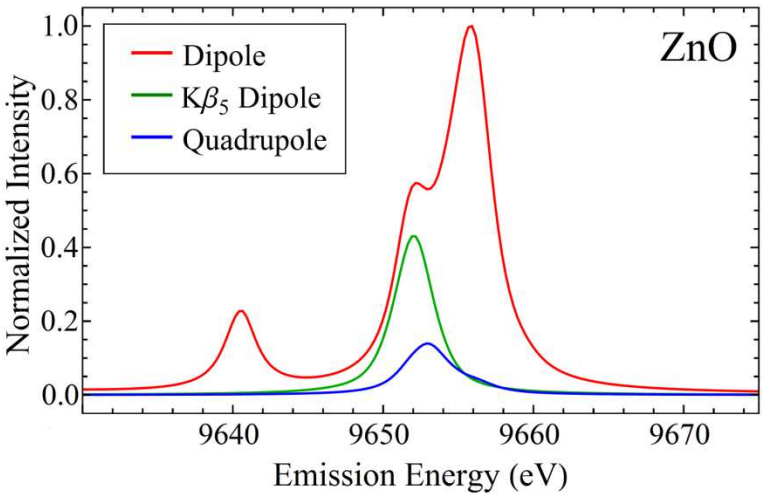

Figure 7.8. The full dipole (red), isolated Kβ5-dipole term (green) and quadrupole (blue) contributions to the FEFF calculation for ZnO. These calculations indicate the Kβ5 term originates from states of both metal 4p and 3d character.

the weak Kβ5 line, which was first investigated in the earlier twentieth century,[321] remains a subject of modest debate. While it is generally regarded as quadrupole-allowed transitions from state of metal 3d character,[5, 29, 30, 322] it has recently been suggested that the major contribution could come instead from dipole allowed 4p-type states from neighboring atoms.[37]

Motivated by this debate, we present in Figure 7.8 the electric dipole and quadrupole contributions to the VTC spectrum of ZnO as determined by FEFF. As the Kβ5 sits atop the tail of the Kβ2 line, we isolate the Kβ5 dipole contribution for an accurate comparison. These calculations suggest that the above interpretations of Kβ5 origin are individually incomplete and that both terms can contribute significantly to the overall intensity.

We return now to a comparison of the three calculations shown in Figure 7.7. Outside of the missing quadrupole contribution in QE, we again see similar predictions made between it and

FEFF in terms of splitting between features. As was the case for Fe, the magnitude of these splittings, particularly between $K\beta_2$ and $K\beta_5$, appear to be underestimated.

In contrast, the NWChem results do an excellent job of reproducing the relative spacing of experimental features. We note that unlike the calculations for QE (3.2 eV spread) and FEFF (6.3 eV spread), the NWChem predictions require a single, *consistent* energy shift across all samples to align with experiment. As discussed in Section 7.6.1, the ability to reliably predict relative energy shifts across sample chemistries is an important feature in VTC-XES analysis and hence this is a significant result in characterizing NWChem performance. The only potential drawback of this code is the prediction of an apparent unphysical peak at ~9646 eV for pure Zn. We believe this feature may be an artifact of the finite cluster size used in calculations.

7.6.3 COMPARISON TO PREVIOUS RESULTS

As discussed in Section 7.2, a body of previous theoretical work has been conducted on inorganic molecular systems. In these studies, time-dependent DFT calculations were applied within the ORCA quantum chemistry package.[146] The full details of their methodology can be found elsewhere.[106, 323] Overall, the strength and weaknesses of these calculations in reproducing experiment match well with our own results discuss above. In general, the ORCA-DFT results have been reported to successfully track relative intensities of VTC features.[33, 35, 106, 108] While the absolute energy scale can deviated significantly, the relative energy scale, both between features within a single spectra and when comparing chemical shifts across samples, tend to show excellent agreement much like the NWChem predictions.[35, 106] In some cases, however, this code has been shown to predict features which are apparently absent in the experimental data.[35] Due to difficulties in removing the $K\beta_{1,3}$ background, it is unknown if there perhaps exist very weak features at these locations.

7.7 CONCLUSION

In summary, we have presented a high-quality VTC-XES dataset of several inorganic Fe and Zn compounds thus demonstrating the high potential of laboratory-based equipment for routine chemical studies. Using this dataset, we evaluated several state-of-the-art DFT-based electronic structure codes each built around distinct theoretical treatments. While each did a fair job of modeling experimental spectra, we found a number of important features (relative chemical shifts, importance of higher-order transitions, energy splitting, *etc.*) that distinguish their performance. We predict that our results will have broad applicability to future VTC studies and will help accelerate the development of XES as a technique on par with XAS.

Chapter 8. A VERSATILE MEDIUM-RESOLUTION X-RAY EMISSION SPECTROMETER FOR DIAMOND ANVIL CELL APPLICATIONS

Originally published as: D. R. Mortensen, G. T. Seidler, J. A. Bradley, M. J. Lipp, W. J. Evans, P. Chow, Y. M. Xiao, G. Boman and M. E. Bowden, Review of Scientific Instruments **84** (8), 4 (2013).

We present design and performance details for a polycapillary-coupled x-ray spectrometer that provides very high collection efficiency at a moderate energy resolution suitable for many studies of nonresonant x-ray emission spectroscopy, especially for samples of heavy elements under high pressures. Using a single Bragg analyzer operating close to backscattering geometry so as to minimize the effect of the weak divergence of the quasicollimated exit beam from the polycapillary optic, this instrument can maintain a typical energy resolution of 5 eV over photon energies from 5 keV to 10 keV. We find dramatically improved count rates as compared to a traditional higher-resolution instrument based on a single spherically-bent crystal analyzer.

8.1 INTRODUCTION

Nonresonant x-ray emission spectroscopy (NXES) has proven to be a powerful method for investigating f-electron behavior under high pressure.[127, 324-327] While spherically-bent crystal analyzers[328] and other high-resolution "direct" diffractive crystal configurations[69-71] ideally suited for the resolution requirements (<1 eV) of resonant x-ray emission and resonant and nonresonant inelastic x-ray scattering experiments[16, 61, 62, 128, 235, 246, 247, 329, 330] are also widely

used in NXES measurements, the large core-hole lifetime for, e.g., lanthanide 2p excitation ($\Gamma_{\text{core-hole}}$ ~ 3.7 - 4.9 eV) suggests that lower-resolution methods having higher collection solid angle can also prove beneficial.

Building on the work of Szlachetko, et. al.,[331-334] we describe here the design and operation of a polycapillary-coupled spectrometer that works near to a backscattering geometry from a single Bragg analyzer, thus maintaining a typical resolution of 5 eV over a wide energy range. Although this approach increases the overall footprint of the spectrometer and places demands on the experimenter to fabricate several suitable Bragg analyzers, the instrument obtains energy resolutions similar to the previously proposed double-analyzer system [332] while eliminating the factor of ~20 loss caused by the second Bragg reflection and greatly simplifying spectrometer operation.

8.2 INSTRUMENTATION

In Figure 8.1, we show a sequence of 3-D renderings of our spectrometer design. Note that the instrument operates in the horizontal scattering plane, unlike an earlier, prototype design;[335] this has several practical benefits, especially as regards the ease of repositioning and mounting of components. Figure 8.1(a) shows the radiation flight paths. The polycapillary optic collects and collimates fluorescence emanating from the sample. Our polycapillary half-lens (XOS, Inc.) has a working distance of 8.5 mm, a capture angle of 16 degrees, an estimated transmission efficiency of 22% (measured at 8 keV), and an output beam size of 7.8 mm. The focal spot size of ~50 μm is a good match with the typical illumination size in diamond anvil cell (DAC) studies, where small samples are used to ensure pressure homogeneity.

To minimize the contribution from elastic scatter, the spectrometer is aligned at 90 degrees to the (horizontally-polarized) incident beam. A flat crystal analyzer in the Bragg geometry is used

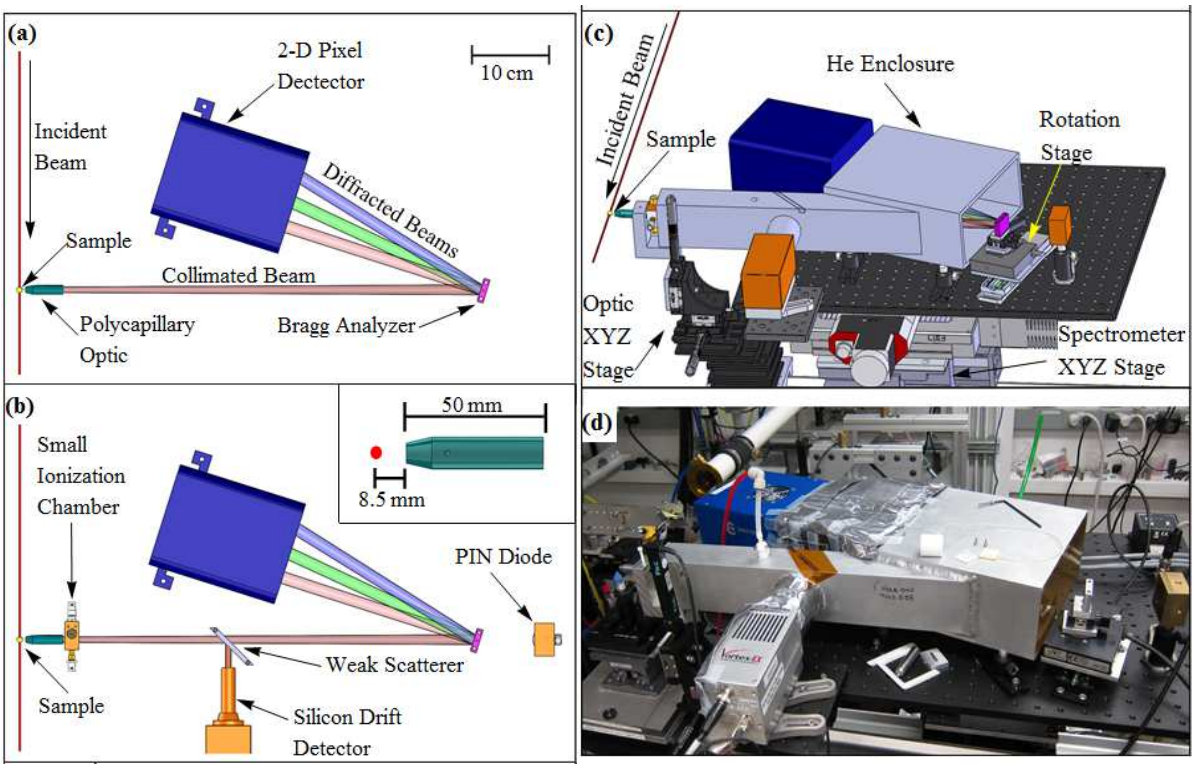

Figure 8.1. Top view of a 3-D rendering of the spectrometer showing: (a) the radiation flight paths, including the range of directions of diffracted beams as the analyzer crystal is rotated, (b) the detectors used to align the optic and characterize total fluorescence transmitted through the polycapillary lens, insert shows dimensions of the optic used in experiment, (c) full instrument, (d) installed instrument at beamline 16-ID-D of the Advanced Photon Source.

as the energy-dispersive component. The large distance between the analyzer and polycapillary output (~50 cm) is needed to ensure sufficient clearances for beam-paths and detectors when working near backscatter from the analyzer crystal.

We use a Pilatus100k detector (Dectris) to measure the diffracted intensity. The large active area of the 2-D position sensitive detector (PSD) allows the detector to remain stationary while covering 7 degrees of Bragg angle, thus decreasing the mechanical requirements and increasing

the ease of operation. Background scatter was constrained by careful shielding and also by synchronously scanning the region of interest on the 2D-PSD with the analyzer's Bragg angle. Alternatively, a scintillation detector, large diode, or other single-pixel detector can be mounted on a linear translation stage at the detector position and, again, synchronously scanned with the rotation of the Bragg analyzer.

The polycapillary lens is aligned using a strongly fluorescing sample, such as a Ni or Fe wire (~500 μm for our experiment), monitored by a PIN diode (Figure 8.1(b)) to measure the collimated signal with the crystal analyzer removed from the radiation path. With the fluorescing sample aligned to the beam the polycapillary is iteratively scanned along both the beam and the two orthogonal directions until the transmitted intensity measured on the PIN diode is maximized. This procedure defines an intersection of the optic focus with the incident beam to which the DAC samples can then be aligned.

Due to the combination of the small focal size of the polycapillary and, for the high-pressure studies presented here, a small sample size, beam drift becomes an important concern. It is therefore useful to monitor the total sample fluorescence *exiting the polycapillary*. A detector in such a location will naturally compensate for the fractional sample illumination that is coincident with the focal volume. In the present design (Figure 8.1(b)) we inserted a weak absorber into the collimated beam, with a silicon drift detector to measure subsequent scatter. The signal, however, proved to be too low to be of statistical value. The instrument will soon be modified to include a small gas ionization chamber directly behind the polycapillary output and in front of the entrance to the He enclosure (Figure 8.1(b) and Figure 8.1(c)). While the ion chamber is unable to discriminated between fluorescence signal and elastic background, the confocal nature

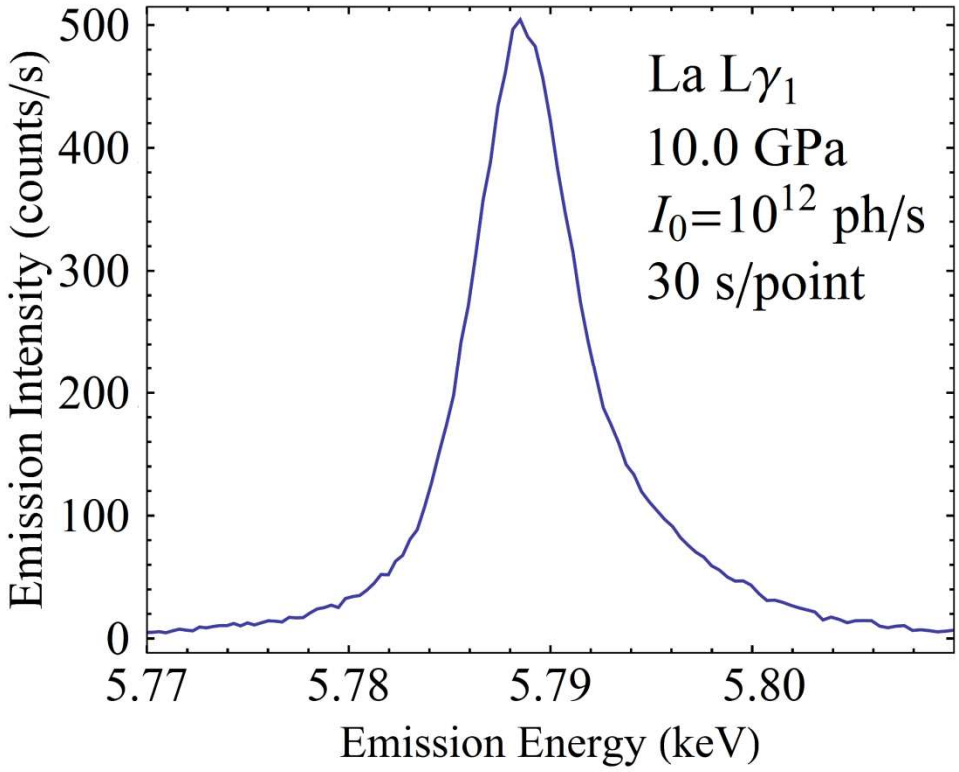

Figure 8.2. Sample La $L_{\gamma 1}$ spectrum using a Ge 333 Bragg analyzer. The data is taken at a pressure of 10.0 GPa with an energy spacing of 0.30 eV and an integration time of 30 s per point, so that the total measurement time is 54 minutes. The count rate at the peak of the emission line is ~500/sec.

of the optic combined with the dominance of the photoelectric cross section for concentrated samples and suppression of the polarization factor gained by working perpendicular to the horizontally polarized incident beam reduce the elastic signal to a negligible level compared to total fluorescence from any concentrated sample.

The complete spectrometer is illustrated in Figure 8.1(c) and shown in Figure 8.1(d). To reduce absorption losses, a helium space is inserted between the optic, analyzer, and detector. The enclosure is made by welding together two Al 6061 alloy rectangular tubes and covers a Bragg

range of 70-84.5 degrees. A similar enclosure covering 58-75 degrees has also been fabricated. The windows are sealed with a 25-μm thick polyimide film. The positioners for the collimating optic are decoupled from the main spectrometer body and its support motors, etc., resulting in a robust design where instrumentation on the spectrometer itself can be manipulated and adjusted without affecting the polycapillary alignment.

8.3 PRELIMINARY RESULTS AND DISCUSSION

Measurements of La Lγ1 NXES were performed at sector 16-ID-D (HP-CAT) of the Advanced Photon Source. The Bragg analyzer was cut from a Ge 333 wafer. An incident energy of 11.3 keV with a flux of approximately 10^{12} photons/s was used. An elemental La sample (~70 μm diameter) was loaded under dry nitrogen into a Be gasket in a panoramic DAC having a 300 μm culet. Pressures were measured using an online ruby optical fluorescence system. A representative NXES spectrum taken at 10.0 GPa is shown in Figure 8.2. Data were taken with a measurement time of 30 seconds per point and a spacing of 0.02 degrees in Bragg angle or equivalently 0.3 eV in energy. A peak count rate of ~500/s was obtained with an energy resolution of ~6 eV. Compared to several earlier lanthanide $L_{\gamma 1}$ measurements made with a single spherically bent crystal analyzer (SBCA) at the same beamline, we find approximately 20 times higher count rates for the polycapillary-coupled spectrometer. This is somewhat larger than the expected theoretical benefit from the respective spectrometer components and geometries; the 'excess' advantage is likely due to the well-known practical difficulties in fabrication of SBCAs and in maintaining perfect large He spaces.

While the short working distance of the polycapillary optic used in this study may prove incompatible with more highly constrained DAC geometries, lenses with smaller diameters or larger working distance can be used instead, albeit with a corresponding loss in solid angle. For

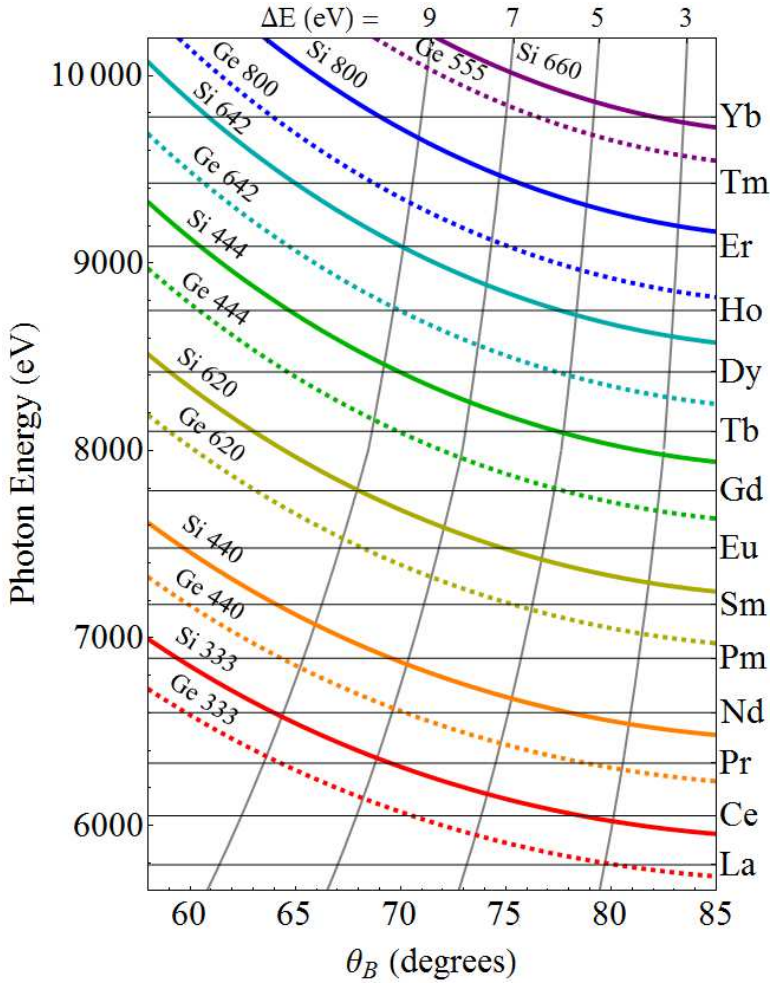

Figure 8.3. Selected reflections near backscatter for lanthanide $L_{\gamma 1}$ fluorescence. Horizontal lines indicate the Lγ1 emission energies for each element. The vertically running curves are lines of constant theoretical energy resolution. The theoretical energy resolution for the Bragg analyzer closest to backscatter ranges from 3.1 eV for La (Ge 333) to a worst case of 7.3 eV for Pm (Si 440), with ~5 eV being typical.

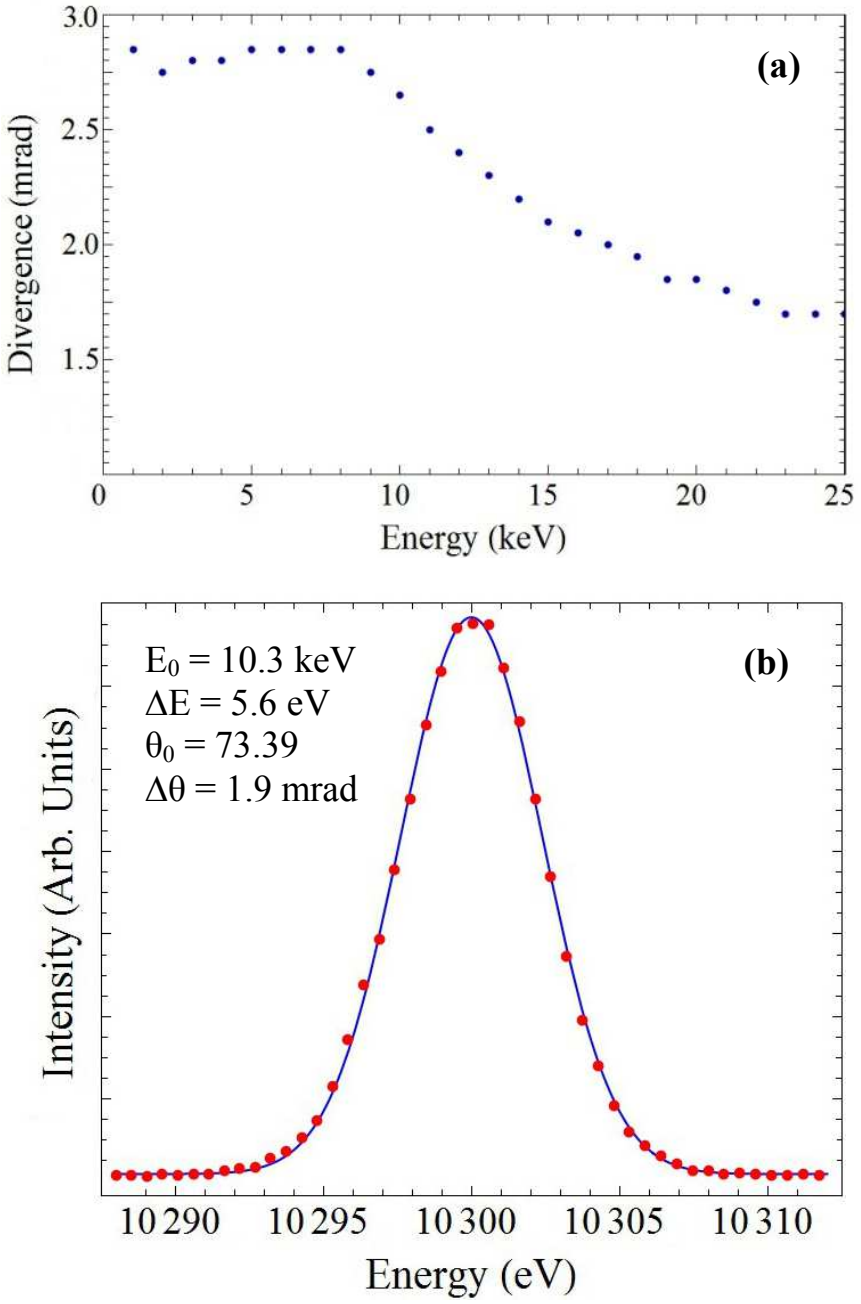

Figure 8.4. (a) Polycapillary divergence as a function of energy[25]; (b) Elastic scatter measured using a Si 555 Bragg analyzer. The red dots and blue line represent experimental data and a Gaussian fit respectively.

example the optic used in our earlier spectrometer design[335] satisfies the constraints of a standard Princeton symmetric cell while surrendering only ~30% in collection efficiency. Finally, the selection of Bragg analyzer reflections close to backscatter must be discussed. As a representative example, all lanthanide $L_{\gamma 1}$ emissions can be covered by a few Si and Ge orientations[336] (see Figure 8.3). Energy resolution is based primarily on the energy-dependent divergence angle of the quasi-collimated beam and can be estimated by error propagation in Bragg's law. The vendor-supplied simulated divergence for the optic used in our experiment[25] is shown in Figure 8.4(a). Measurements made on elastic scatter at 10.3 keV were fit to a Gaussian function yielding an energy resolution of 5.6 eV (see Figure 8.4(b)). This translates to a divergence of 1.9 mrad, which is lower than the estimate of 2.6 mrad presented in Figure 8.4(a). Using the conservative parameters provided in Figure 8.4(a) the anticipated energy resolution for the Si and Ge configurations in Figure 8.3 vary from a best case of 3.1 eV for La with Ge 333 to a worst case of 7.3 eV for Pm with Si 440 with ~5 eV being typical.

8.4 CONCLUSIONS

In summary, we have demonstrated that a simplified polycapillary-coupled spectrometer based on a single high-quality Bragg analyzer can maintain useful energy resolution and superior count rates for nonresonant XES studies of heavy elements in high-pressure environments.

Chapter 9. NON-RESONANT X-RAY EMISSION SPECTROSCOPY: INSIGHTS INTO THE BEHAVIOR OF 4F-ELECTRONS DURING VOLUME COLLAPSE

The text of this chapter is a preliminary discussion of new experimental and theoretical work by D. R. Mortensen, W. T. Chiu, M. J. Lipp, G. T. Seidler and R. T. Scalettar. Special credit is given to W. T. Chiu for his work on the theorectical calculations presented here.

Using the satellite structure of the $L\gamma_1$ line in non-resonant x-ray emission spectra, we probe the high-pressure evolution of the bare 4f moments of the early light lanthanides at ambient temperature. For Ce and Pr this satellite peak experiences a sudden reduction concurrent with their respective volume collapse transitions. The partial persistence of this feature (~70% for Ce and 60% for Pr), however, still argues qualitatively in favor of the Kondo volume collapse model. These results are supported by theoretical results from state-of-the-art extended atomic structure code. These measurements emphasize the importance of studying microscopic observables to obtain the most discerning test of the underlying, fundamental f-electron phenomenon at high pressures.

9.1 F- ELECTRONS AND VOLUME COLLAPSE: HUBBARD-MOTT VS. KONDO

The chemistry of lanthanides is of critical importance to a wide number of fields such as catalysis,[337-339] high-temperature superconductivity,[340, 341] and bioscience.[342, 343] Yet despite a rich history of research and applications, a clear theoretical treatment of these materials remains a fundamental challenge. The difficulty stems primarily from the underlying nature of f-electron states. In materials with partially filled f shells, the electrons occupy narrow energy bands

leading to strong correlations. These electronic interactions exist between the well understood atomic and uncorrelated band limits and are responsible for a veritable zoo of exotic behaviors: metal-to-insulator transitions,[344] superconductivity,[345] hidden orderings,[346] *etc*. These properties tend to show extreme sensitivity to small changes in local environment (e.g., temperature, pressure, doping) and as such are difficult to predict.

A primary example of the trouble in modeling emergent phenomena in f-electron material is the issue of volume collapse (VC); at high pressures several lanthanides are known to undergo a first-order phase transition that results in large changes to the lattice constants. After decades of study since the discovery of this phenomenon in Ce,[347-349] the mechanisms driving the VC are still uncertain. Currently two general theoretical perspectives dominate the debate, each having a distinct perspective on the relative importance of f-electron correlations and delocalization. The first is the Hubbard-Mott (HM) model[350, 351] in which high pressure increases the inter-atomic overlap of initially localized 4f wave-functions to the point of driving hopping of electrons between neighboring atoms, thus leading to an abrupt transition to a weakly correlated, delocalized 4f band. The second, the Kondo volume collapse (KVC) model,[352-354] instead attributes the behavior to an exponential rise in the Kondo temperature with compression to above the working temperature wherein the decreased unit cell volume effectively switches on a dynamic screening of the 4f electrons by the broad valence bands.[355-357] In contrast to the HM model, the KVC model anticipates a continuous and prolonged delocalization.

9.2 Probing the bare 4f Moment

While each of the HM and KVC theories has had notable successes in predicting experimental observables for Ce, particularly macroscopic observables such as the equation of state,[358, 359] they are cleanly distinguished by starkly contrasting expectations for the behavior of a foundational

microscopic observable: the bare (i.e., unscreened) 4f magnetic moment. Upon crossing the VC transition, the complete 4f itinerancy predicted by the HM model necessarily extinguishes the 4f moment whereas the hybridization, leading to increased f-screening, of the KVC anticipates much smaller effects on the *bare* moment.

Motivated by this distinction, Lipp, et. al recently presented a study of the pressure evolution of the $L\gamma_1$ ($4d^{3/2} \rightarrow 2p^{1/2}$) non-resonant x-ray emission spectra (NXES) for metallic Ce across its VC transition.[326] Analogous to the Kβ′ feature in 3d-transition metal NXES (see Section 1.4.2), the $L\gamma_1$ line exhibits a lower-energy satellite feature (the so-called $L\gamma_1'$) arising from (4f,4d) exchange. As such, the intensity of this emission provides a sensitive test of the bare 4f moment. In this work, the intensity of this satellite peak was found to experience only a 30% drop across the VC, which the authors argued offers strong support of the KVC picture.

Here, we report an extension of this methodology to La, Pr, and Nd trivalent metals. Together with Ce these early light lanthanides, which exhibit nominal $4f^0$, $4f^1$, $4f^2$, and $4f^3$ occupancies at ambient conditions, offer a compelling test bed for distinguishing between the HM and KVC models. Using the theoretical groundwork reported previously in Lipp, et. al,[326] we compared the volume-collapsed NXES data of Ce and Pr to the predictions made by advanced, modified atomic calculations. These results demonstrate both a sudden onset of 4f-conduction band hybridization and a partial persistence of 4f occupation across the VC transition, offering strong support of the KVC picture. Furthermore, we find that these results when interpreted for the central microscopic observable, i.e., the bare 4f moment, disagree qualitatively (Ce, Pr) and quantitatively (Ce, Pr, Nd) with prior state-of-the-art dynamic mean field theory (DMFT) predictions.

9.3 EXPERIMENTAL DETAILS

All measurements were performed at beam line 16ID-D of the Advanced Photon Source. Samples (99.9% purity) were loaded into panoramic diamond anvil cells fitted with either 300-700 μm culet diamonds for lower pressures or 100 μm flat beveled diamonds for higher pressures. To prevent oxide formation each sample was loaded in a glove box flushed with dry nitrogen and brought up to a low pressure to ensure a good seal. Pressure was measured by optical fluorescence from ruby chips loaded with the sample. The incident beam (11.3-20.0 keV) was brought through the diamond with the measured fluorescence escaping perpendicularly through the Be gasket, measured in the scattering plane. La, Pr, and Nd NXES experiments were conducted with newly developed polycapillary-based Bragg spectrometers.[335, 360] These spectrometers use half-lens collimating optics coupled to flat crystal analyzers (Ge 333, Ge 440 and Si 440 for La, Pr, and Nd respectively) with either a scintillation (Cyberstar) or 2D pixel detector (Dectris). All Ce $L\gamma_1$ NXES have been directly reproduced from Lipp, et. al.[326] All spectra were normalized by incident flux and corrected for a linear background.

9.4 EXPERIMENTAL RESULTS AND PRELIMINARY DISCUSSION

We present the measured $L\gamma_1$ NXES spectra as a function of pressure for La, Ce, Pr, and Nd in Figure 9.1. For clarity of presentation this data has been smoothed using a non-broadening third-order Savitzky-Golay filter with a 5 eV window (comparable to the lifetime-limited resolution of 3.7-4.0 eV) and normalized to peak intensity. Raw data (without smoothing) is used in Figure 9.2 and data analysis below. Also shown is the highest pressure data subtracted from the lowest pressure data for each element, so as to highlight the influence of pressure on the spectral shape. From the data we can identify several important features. Before discussing these results,

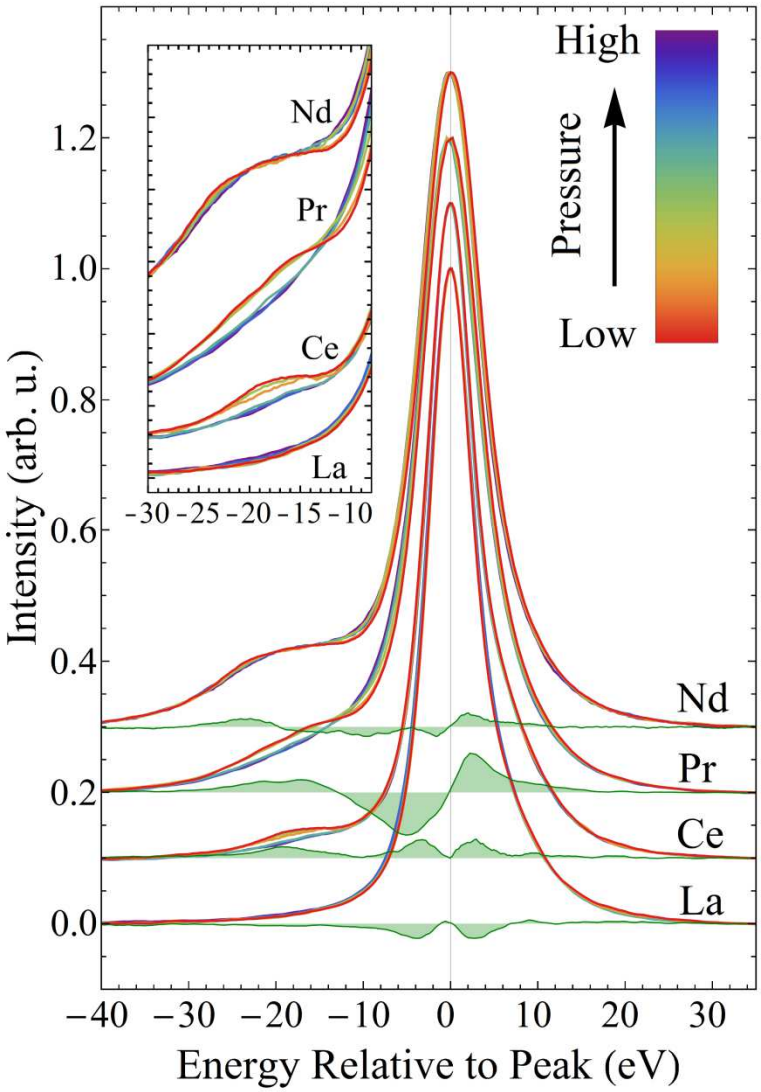

Figure 9.1. Experimental $L\gamma_1$ emission spectra normalized to peak intensity. A non-broadening, third-order Savitzky-Golay smoothing filter of 5-eV window has been applied to each spectrum. For clarity each element has been offset by 0.1. Also shown is the highest pressure data subtracted from the lowest pressure data for each element (shaded green).

however, some brief context is needed on the known behavior of the light lanthanides under pressure and on the underlying physics of the $L\gamma_1$ NXES spectra.

First, under pressure the lanthanide crystal structures initially pass through a number of high-symmetry transformations, consisting of different stacking sequences of close-packed layers, later transitioning to low-symmetry early-actinide-like phases thought to be indicative of f-electron bonding.[361-363] While in Pr this transition is accompanied with a large VC (~10%),[349, 364-368] Nd reaches its low-symmetry α-U structure entirely through smooth transformations.[369] Hence, Nd does not exhibit a VC transition. Ce is a unique case as it experiences a VC (15%) that is iso-structural (fcc) and therefore unassociated with the high-to-low symmetry transition. For this reason volume collapse is thought to be primarily an electronically-driven transition.

Second, as demonstrated in the work of Lipp, et al.,[326] NXES provides a sensitive measure of the intrinsic 4f moment evolution in Ce. In $L\gamma_1$ NXES a high-energy photon, tuned well above the L_2 ($2p^{1/2}$) edge, promotes a 2p electron into the continuum. The resulting core-level vacancy is unstable and may be filled by a $4d^{3/2}$ electron accompanied by either photon emission (i.e., $L\gamma_1$ x-ray fluorescence) or the ejection of an Auger electron. When the lanthanide species has a nonzero 4f-occupancy, a low energy satellite (commonly referred to as $L\gamma_1'$) appears below the main $L\gamma_1$ fluorescence peak due to intra-atomic exchange between the 4f and 4d orbitals, in close analogy to the much better studied case of Kβ x-ray fluorescence from the 3d transition metal systems.[16] The relative intensity and position of the $L\gamma_1'$ shoulder reflects the strength of the coupling and is directly sensitive to the size of the ground state magnetic moment.[370]

Some care, however, must be given in demonstrating that this technique is a true probe of the *bare* moment, i.e., is free of screening effects. It is important to note that the timescale of the NXES event is set by the *2p* core-hole lifetime (~1 fs) which strongly suggests a "snap-shot" picture of the electronic configuration free from screening effects. Indeed for Ce it has been explicitly demonstrated via extended local atomic calculations that there is a qualitative tracking

between $L\gamma_1'$ intensity and the *bare* $\langle J^2 \rangle$ moment.[326] This is further strengthened by the large discrepancy between $L\gamma_1'$ changes and those observed in magnetic susceptibility (proportional to the square of the *screened* 4f moment), with the latter decreasing by almost 80% across the VC compared to only 30% for the former.[371, 372] Therefore NXES effectively measures the *bare* moment of Ce. While these same susceptibility measurements have not been performed for Pr and Nd, the comparable core-hole lifetimes suggest NXES remains a suitably fast probe, unaffected by screening.

With these details in mind, we return to Figure 9.1. First, note that the La $L\gamma_1$ NXES spectra show no $L\gamma_1'$ exchange peak up to 64.0 ± 3.0 GPa, beyond the reentrant fcc phase starting at 60 GPa,[373] indicating no change from its nominally $4f^0$ configuration. This null result indicates that the changes observed in Ce, Pr, and Nd $L\gamma_1'$ peaks are physically meaningful and not the result of systematic effects. That being said, La does display an apparent broadening of the main $L\gamma_1$ peak (on the order of ~0.5 eV) with increased pressure. We propose that this effect, which to the best of our knowledge has not been previously reported, is due to increased splitting in the multiplet structure underlying to the $L\gamma_1$ peak. The changing spectral shape therefore likely contains valuable information on the evolving 4d-electron interactions[129] and thus merits future theoretical considerations.

Second, in contrast to La ($4f^0$), Ce and Pr, which are nominally $4f^1$ and $4f^2$ at ambient conditions, exhibit large and sudden decreases in $L\gamma_1'$ intensity concurrent with the VC transitions (0.9 GPa and 20.0 GPa respectively). Taken naively this result could be used as evidence in support of the HM model as described above. It must be noted, however, though that the increased 4f-5d hybridization predicted by KVC invariably mixes the 4f electrons out of their native orbitals, leading to deviations from the ground state electronic configuration; the

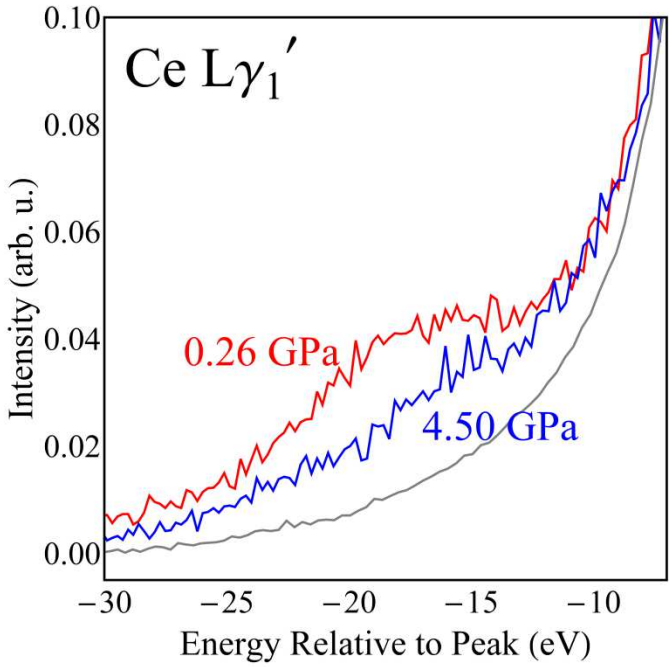

Figure 9.2. The Ce $L\gamma_1'$ satellite below (red) and above (blue) the VC transition. Although the satellite intensity is reduced above the collapse, a comparison to ambient pressure La (gray), for which there is truly a zero 4f-moment, indicates a partial persistence of the feature. For comparison the data have been normalized to peak intensity. Ce data has been reproduced from M. J. Lipp, et al., Physical Review Letters **109** (19), 195705 (2012).[326]

hybridization causes a rise in the $f^{n\pm1}$ configuration weights at the expense of the sharp, low-pressure f^n configuration. Indeed, this phenomenon has already been experimentally observed in resonant inelastic x-ray scattering measurements.[374, 375] As each configuration carries its own moment, such variations would necessarily modulate the $L\gamma_1'$ feature.

This potentially ambiguous result can be clarified by a direct comparison to La, for which there is a true zero 4f moment. As shown in Figure 9.2, the f-electron signature, while reduced, does not fully vanish in the collapsed-phase Ce spectrum, inconsistent with a complete Mott-like delocalization. Pr NXES, which has a broader main $L\gamma_1$ peak than Ce, does not lend itself to a

direct La comparison. The persistence of its 4f bare moment, however, will be demonstrated below.

Nd, which is not subject to any large VC transition, shows a minor change in the $L\gamma_1'$ peak as displayed in Figure 9.1. This is a shift in $L\gamma_1'$ to a slightly higher energy (~0.3 eV) concomitant with a transition from an fcc to a distorted-fcc structure at ~18.0 GPa.[369, 376] As the 4f electrons are still localized at this pressure, the observed shift is likely due to subtle changes in the relative positioning and subsequent electron transfer between conduction subbands which are known to occur during the high-symmetry transformations.[377] As will be shown shortly, however, the normalized amplitude of the $L\gamma_1'$ peak is unchanged during this shift. We note that this change is not associated with any known delocalization transition; for example, prior diffraction and electrical resistivity measurements suggest that 4f delocalization in Nd occurs gradually beginning only at 100 GPa.[377]

9.5 THEORETICAL PREDICTIONS AND RESULTS

To this point we have made only qualitative arguments regarding the pressure dependence of the $L\gamma_1'$ shoulder in our data. We supplement this discussion with a theoretical treatment of Ce and Pr (i.e., those elements exhibiting a VC transition). In the Kramers-Heisenberg formulism, the intensity of NXES, $I(\omega)$, is given as:

$$I(\omega) \propto \sum_{|f\rangle} \left| \sum_{|n\rangle} \frac{\langle f|T|n\rangle\langle n|a_c|g\rangle}{E_g - E_n - \omega - i\Gamma_n} \right|^2 \tag{9.1}$$

where T is the dipole operator for 4d→2p transitions, a_c is annihilation is the annihilation operator of the core electron, ω is the energy of emission, and $|g\rangle$, $|n\rangle$ and $|f\rangle$ are the ground, intermediate and final states respectively with energies E_g, E_n and E_f. For more details on this formulism see Section 3.3.

To account for finite temperature effects equation (9.1) is modified assuming a Boltzmann distribution:

$$I(T,\omega) = \langle I(\omega)\rangle_T = \frac{\sum_g e^{-Eg/kT} I(\omega)}{\sum_g e^{-Eg/kT}} \tag{9.2}$$

where T is the working temperature (300 K in the analysis below) and k is the Boltzmann constant.

In order to evaluate this equation, the electron states are determined by diagonalizing the total Hamiltonian, $H = H_1 + H_2$. The first component, H_1, is taken from the Anderson impurity model[378] :

$$\begin{aligned} H_1 = {} & \textstyle\sum_{k,\mu} \epsilon_k a^\dagger_{k,\mu} a_{k,\mu} + \sum_{f,\nu} \epsilon_f a^\dagger_{f,\nu} a_{f,\nu} + \sum_{p,\zeta} \epsilon_p a^\dagger_{p,\zeta} a_{p,\zeta} + \sum_{d,\eta} \epsilon_d a^\dagger_{d,\eta} a_{d,\eta} + \\ & \tfrac{V}{\sqrt{N}} \textstyle\sum_{k,\nu} \left(a^\dagger_{f,\nu} a_{k,\nu} + a^\dagger_{k,\nu} a_{f,\nu} \right) + u_{ff} \sum_{\nu>\nu'} a^\dagger_{f,\nu} a_{f,\nu} a^\dagger_{f,\nu'} a_{f,\nu'} - \\ & u_{fp} \textstyle\sum_{\nu,\zeta} a^\dagger_{f,\nu} a_{f,\nu} \left[1 - a^\dagger_{p,\zeta} a_{p,\zeta} \right] - u_{fd} \sum_{\nu,\zeta} a^\dagger_{f,\nu} a_{f,\nu} \left[1 - a^\dagger_{d,\eta} a_{d,\eta} \right] \end{aligned} \tag{9.3}$$

where ϵ_i is the on-site energy for orbital i, $a^{(\dagger)}_{i,\sigma}$ is the annihilation (creation) operator for an electron of orbital angular momentum i, with σ serving as a combined index of the m_l and m_s quantum numbers, u_{ff} is the f-electron Coulomb potential, $u_{fp(d)}$ is the 2p (4d) core-hole potential, and V is the hybridization between the f-electron and a conduction orbitals under pressure as predicted by the KVC model. In the absence of hybridization, the ground state consists entirely of the nominal f^n occupation (n =1,2 for Ce and Pr respectively) as discussed above. As this parameter increases with pressure, the ground state becomes a mix of f^n and $f^{n\pm1}$ configurations.

The second term, H_2, completes the electron-electron interactions by accounting for multiplet interactions terms:

$$H_2 = \textstyle\sum_{\nu_1,\nu_2,\nu_3,\nu_4} g_{ff}(\nu_1,\nu_2,\nu_3,\nu_4) a^\dagger_{f,\nu_1} a^\dagger_{f,\nu_2} a_{f,\nu_3} a_{f,\nu_4}$$

$$+\sum_{\nu_1,\nu_2,\zeta_1,\zeta_2} g_{fp}(\nu_1,\nu_2,\zeta_1,\zeta_2)a^{\dagger}_{f,\nu_1}a^{\dagger}_{p,\zeta_1}a_{p,\zeta_2}a_{f,\nu_2}$$
$$+\sum_{\nu_1,\nu_2,\eta_1,\eta_2} g_{fd}(\nu_1,\nu_2,\eta_1,\eta_2)a^{\dagger}_{f,\nu_1}a^{\dagger}_{d,\eta_1}a_{d,\eta_2}a_{f,\nu_2}$$
$$+\sum_{\nu_1,\nu_2} \alpha_{\nu_1,\nu_2}a^{\dagger}_{f,\nu_1}a_{f,\nu_2}+\sum_{\zeta_1,\zeta_2} \beta_{\zeta_1,\zeta_2}a^{\dagger}_{p,\zeta_1}a_{p,\zeta_2}$$
$$+\sum_{\eta_1,\eta_2} \gamma_{\eta_1,\eta_2}a^{\dagger}_{d,\eta_1}a_{d,\eta_2} \qquad (9.4)$$

where g are the parameters of the Slater-Koster integrals, and $\alpha, \beta,$ and γ are the spin-orbit coupling parameters for respectively the f, p, and d orbitals. All of these values were obtained from Cowan's atomic structure code[379] using the Hartree-Fock approximation and including relativistic effects. The values of g were scaled by 0.8 to account for screening.

In Figure 9.3, we present the results of these calculations compared to the experimental data. It must be noted that in the theoretical results, the atomic multiplet features composing the Lγ$_1'$ satellite are sharper than they appear in experiment. This is a result of the using only five discrete conduction orbitals in place of the true, broad 5d band for calculating hybridization. Such an approximation is necessary to ensure reasonable computation time. Nevertheless, it is clearly demonstrated that the steplike decrease in Lγ$_1'$ intensity observed in Ce and Pr concomitant with VC is consistent with a sudden onset of 4f-conduction band hybridization as predicted by the KVC model.

Taken a step further, we calculate the relationship between relative Lγ$_1'$ intensity and 4f occupation, n_f, which is given by:

$$n_f = \frac{\sum_g e^{-Eg/kT}\langle g|a^{\dagger}_{f,\nu}a_{f,\nu}|g\rangle}{\sum_g e^{-Eg/kT}}. \qquad (9.5)$$

The results, shown in Figure 9.4, demonstrate that both quantities decrease upon hybridization with the Lγ$_1'$ intensity doing so at a slightly faster rate. The important point, however, is that a persistent Lγ$_1'$ feature is indicative of continued 4f localization.

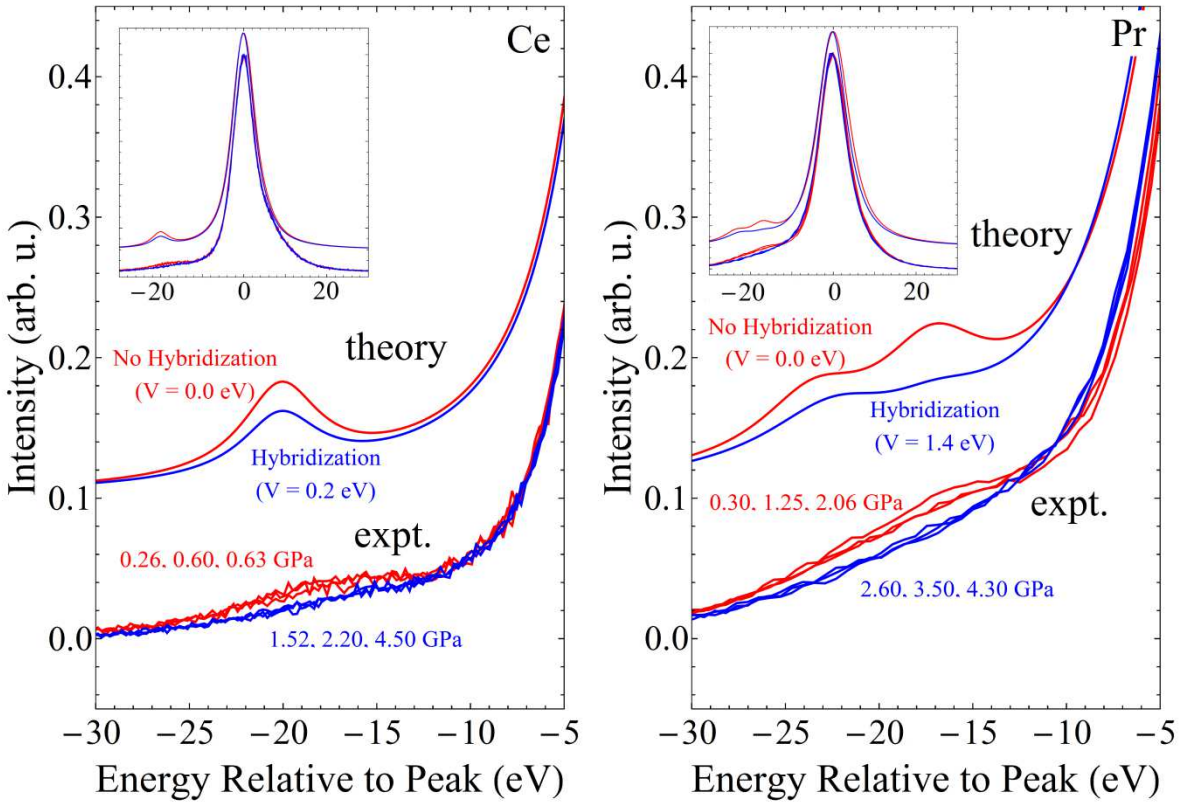

Figure 9.3. The Lγ$_1$′ feature of Ce (left) and Pr (right) as measured experimental (expt.) and calculated via an extended atomic code (theory). The theoretical results show narrow peaks due to the use of discrete conduction orbitals in the calculation. Nonetheless, the qualitative agreement between experiment and theory is excellent, showing that increased 4f-conduction hybridization (V) effectively describes the observed physics. Insets: the full Lγ$_1$ spectra.

To this end, we present a quantitative extraction of the relative Lγ$_1$′ intensities. While comparison to La is a useful diagnostic for Ce as shown above, it does not work well for Pr and Nd where the differences in the multiplet structure of the Lγ$_1$ peak are enough to prevent a direct cross evaluation. Instead we fit the low-energy side (up to approximately 2.5 eV below the Lγ$_1$ peak) of each spectrum to a sum a two Lorenztians: one to model the contribution from the main

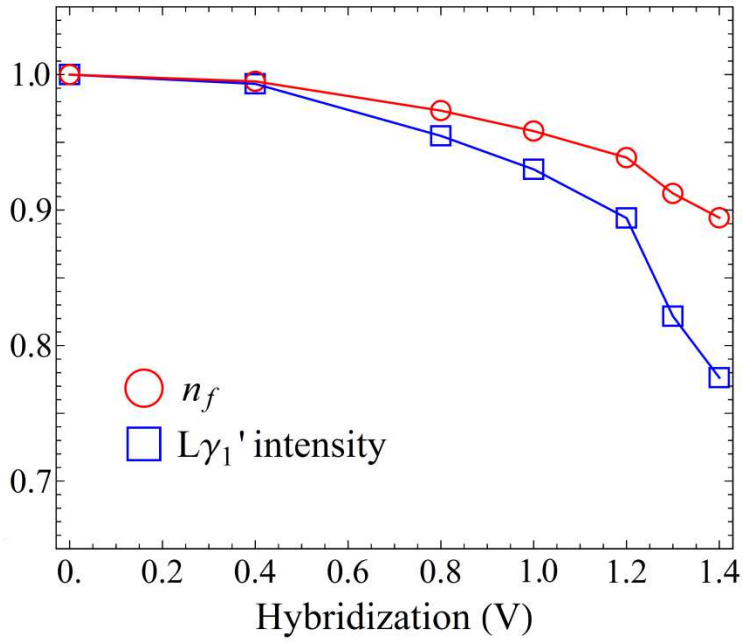

Figure 9.4. A comparison of the evolution of calculated 4f occupation, n_f, and Lγ_1' intensity of Pr with hybridization (V).

peak in the satellite region and the other to fit the Lγ_1' peak proper. This procedure has previously been used for Ce NXES.[326] The results shown in Figure 9.5 reflect the spectral weight of the shoulder relative to the main peak. For Ce, Pr, and Nd these results have been normalized to the largest intensity below the transition for each sample. This procedure is needed to eliminate small run-to-run variations due to differences in spectrometer tune up that would otherwise prevent direct comparison.

La, which was found to have constant, negligible intensity at all pressures, is left unnormalized. Nd is similarly found to have negligible variation even during the minor change in spectral shape upon the fcc to distorted-fcc transition at 18.0 GPa discussed in Section 9.4.

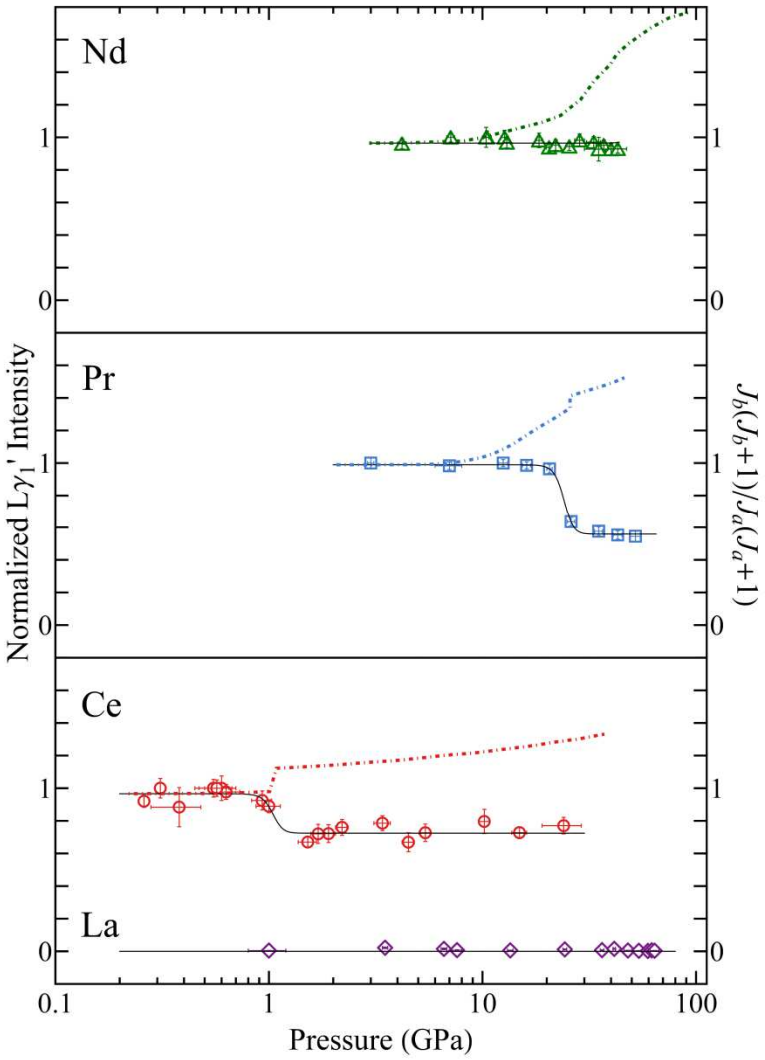

Figure 9.5. Comparison of relative Lγ$_1$′ intensity (data points) with DMFT predictions for $J_b(J_b+1)$ (dot-dashed lines). Intensity of the Lγ$_1$′ satellite is calculated relative to the main Lγ$_1$ peak. For Ce, Pr, and Nd the intensities have been normalized to the largest value below the transition for each sample in order to reduce the effects of run-to-run variations. La, which has negligible Lγ$_1$′ intensity, is left unnormalized. The solid black lines are meant as a guide for the eye. The dot-dashed lines show the DMFT *bare moment* values, $J_b(J_b+1)$ relative to the atomic-limiting values, $J_a(J_a+1)$.

Further measurements are required to determine if Nd eventually undergoes $L\gamma_1'$ reduction, similar to Ce and Pr, upon reaching its delocalized α-U phase at ~100 GPa.[369]

As anticipated both Ce and Pr $L\gamma_1'$ intensities undergo a large, sudden drop with the VC. These reductions, however, are incomplete with ~70% and ~60% for Ce and Pr respectively. This result, taken in consideration with the trend shown in Figure 9.4, clearly demonstrates a prolonged localization of the 4f electrons. This picture is inconsistent with the formation of a 4f band as predicted by HM and instead strongly favors the description put forth by the Kondo model.We can further compare these results with recent LDA+DMFT calculations of the bare 4f moment.[380, 381] These theoretical predictions, whose dependence on unit-cell volume has been converted to a pressure dependence using experimental equation of state data,[364-369, 376] are shown in Figure 9.5 as the dot-dashed lines for each of Ce, Pr, and Nd. . While these calculations have had great success in predicting the behavior of the *screened* 4f moment as inferred from magnetic susceptibility measurements,[371, 372] we see here very poor agreement in its expectation of the *bare* moment.

For each element the calculations predict a growth in *bare* moment with compression due to an increase in the f-shell occupancy caused by a rise in the 6s and 6p bands relative to the 4f levels. This is incorrect for Ce and Pr, and although our experimental data does show an increase in the case of Nd, it occurs less gradually and its onset is at a much higher pressure than predicted. It must be noted that these calculations were carried out at a higher temperature (623 K), however the authors expect only modest corrections at room temperature. Nonetheless, it remains that these theoretical methods are demonstrably insufficient in modelling *bare* 4f moment evolution and at the very least overestimate the configuration interaction between 6s, 6p and 4f electrons.

9.6 CONCLUSION

In summary, we have presented a high-quality dataset of high pressure $L\gamma_1$ NXES useful for the characterization of *bare* 4f moment evolution in the early light lanthanide metals. The persistence of a 4f-4d exchange feature beyond the volume collapse Pr has been clearly demonstrated in contradiction to the predictions made by the Hubbard-Mott model and in favor of the Kondo volume collapse picture previously promoted by the Ce data.[326] These observations are supported by state-of-the-art modified atomic calculations which show a clear relationship between $L\gamma_1'$ intensity and 4f-conduction band hybridization. We anticipate that these results will contribute to continued work of understanding f-electron chemistry in highly correlated systems.

Chapter 10. CONCLUSION

10.1 SUMMARY

In this dissertation, I have presented several studies demonstrating the strength of non-resonant x-ray emission spectroscopy (NXES) in determining the structure of near Fermi-level electronic states in transition metal and lanthanide systems. These studies, ranging from ambient conditions to high pressures and temperatures, highlight the versatility of NXES in elucidating chemical state in condensed matter experiment. Indeed, in some cases this technique provides the only direct measure of key electronic information.

In support of this work, several novel crystal spectrometers were developed and commissioned. Of primary importance are the Rowland-circle, laboratory-based monochromators discussed in Chapters 4-6. This research program, which began in 2013, has proven to be a paradigm-shifting event, enabling new courses of study conducted at the University of Washington. Prior to this work, all x-ray spectroscopic measurements were conducted off-site at synchrotron facilities. The continued development and refinement of this instrumentation has resulted in two US provisional patents (62/271,989 and 62/271,992) for myself and Prof. Gerald Seidler.

While also suited to absorption measurements, here I have demonstrated the power of these spectrometers for NXES applications. In particular, I have presented a high-quality dataset of weak, valence-to-core (VTC) emission lines which, as discussed in Chapter 3, are of growing importance to chemical studies. This dataset, comprised of several inorganic Fe and Zn compounds, provides an interesting range of local electronic and atomic structure which I applied as a benchmark test of several state-of-the-art density functional (DFT) theory calculations. These tests highlighted the key strengths of DFT methods as well as identifying

several areas which require careful consideration for robust prediction and interpretation of experimental results.

Additionally, I have described a unique, medium-resolution spectrometer for use at synchrotron facilities. This instrument was used to accelerate a course of study aimed at investigating the evolving behavior of 4f-electrons under high pressure. By careful consideration of the $L\gamma_1'$ NXES line, combined with extended atomic calculations, we determined a persistent 4f-localization upon crossing the volume collapse transitions in cerium and praseodymium. This observation provides strong supporting evidence of a Kondo-like screening transition, helping to resolve a decades-long debate.

10.2 FUTURE DIRECTIONS

We anticipate that the laboratory-based spectrometers discussed above will continue to have high impact in the scientific community. In particular, we predict that the ready availability of instrumentation will open new avenues of opportunity underserved by the current access model such as teaching, quality control, long baseline studies, *etc*. As part of this effort, one of these instruments (CEI-XANES) is now operating as part of the Molecular Analysis Facility on the University of Washington campus. This shared facility is opened to both internal and external users, having already been used in both academic and industrial research. It is our sincere hope that this work will expand and strengthen the x-ray spectroscopy community, establishing these techniques as routine materials characterization methods.

As mentioned in Chapter 9, a series of papers are currently in preparation based on the new experimental and theoretical work of f-electron behavior under high pressure. In addition to the calculations presented in this work, we anticipate that multiplet theory will soon be completed for lanthanum and neodymium. High-quality data has also been collected for samarium and

europium. This analysis, along with the continued development of the supporting electronic structure calculations, will continue to be an area of focus with our collaborators at Lawrence Livermore and UC Davis. As a next step, we propose this work be extended to gadolinium which also exhibits a volume collapse transition.

BIBLIOGRAPHY

1. M. Newville, in *The XAFS Model Compound Library* (Cr2O3 powder, 1997; http://cars.uchicago.edu/xaslib/spectrum/695).
2. M. Newville, in *Spectroscopic Methods in Mineralology and Materials Sciences*, edited by G. S. Henderson, D. R. Neuville and R. T. Downs (Mineralogical Soc Amer, Chantilly, 2014), Vol. 78, pp. 33-74.
3. J. E. Penner-Hahn, Coordination Chemistry Reviews **249** (1-2), 161-177 (2005).
4. M. Rovezzi and P. Glatzel, Semiconductor Science and Technology **29** (2), 19 (2014).
5. A. C. Thompson, J. Kirz, D. T. Attwood, E. M. Gullikson, M. R. Howells, J. B. Kortright, Y. Liu, A. L. Robinson, J. H. Underwood, K. J. Kim, I. Lindau, P. Pianetta, H. Winick, G. P. Williams and J. H. Scofield, *X-ray Data Booklet*, Third edition ed. (Lawrence Berkeley Laboratory, Berkeley, 2001).
6. G. H. Zschornack, *Handbook of X-ray Data*. (Springer Berlin Heidleberg, Berlin, 2007).
7. J. A. Bearden, Reviews of Modern Physics **39** (1), 78-& (1967).
8. M. O. Krause and J. H. Oliver, Journal of Physical and Chemical Reference Data **8** (2), 329-338 (1979).
9. J. Kawai, C. Suzuki, H. Adachi, T. Konishi and Y. Gohshi, Physical Review B **50** (16), 11347-11354 (1994).
10. J. Kawai, M. Ohta and T. Konishi, Analytical Sciences **21** (7), 865-868 (2005).
11. P. Glatzel, Ph.D. thesis, Hamburg University, 2001.

12. O. Sogut, E. Buyukkasap and H. Erdogan, Radiation Physics and Chemistry **64** (5-6), 343-348 (2002).

13. S. Raj, H. C. Padhi, P. Palit, D. K. Basa, M. Polasik and F. Pawlowski, Physical Review B **65** (19), 4 (2002).

14. F. Pawlowski, M. Polasik, S. Raj, H. C. Padhi and D. K. Basa, Nuclear Instruments & Methods in Physics Research Section B-Beam Interactions with Materials and Atoms **195** (3-4), 367-373 (2002).

15. I. Han and L. Demir, Physical Review A **82** (4), 6 (2010).

16. P. Glatzel and U. Bergmann, Coordination Chemistry Reviews **249** (1-2), 65-95 (2005).

17. H. C. Padhi, C. R. Bhuinya and B. B. Dhal, Journal of Physics B: Atomic, Molecular and Optical Physics **26** (23), 4465 (1993).

18. P. Glatzel, U. Bergmann, F. M. F. de Groot and S. P. Cramer, Physical Review B **64** (4), 045109 (2001).

19. G. Peng, F. M. F. Degroot, K. Hamalainen, J. A. Moore, X. Wang, M. M. Grush, J. B. Hastings, D. P. Siddons, W. H. Armstrong, O. C. Mullins and S. P. Cramer, Journal of the American Chemical Society **116** (7), 2914-2920 (1994).

20. S. D. Gamblin and D. S. Urch, Journal of Electron Spectroscopy and Related Phenomena **113** (2-3), 179-192 (2001).

21. H. Visser, E. Anxolabehere-Mallart, U. Bergmann, P. Glatzel, J. H. Robblee, S. P. Cramer, J. J. Girerd, K. Sauer, M. P. Klein and V. K. Yachandra, Journal of the American Chemical Society **123** (29), 7031-7039 (2001).

22. S. A. Pizarro, P. Glatzel, H. Visser, J. H. Robblee, G. Christou, U. Bergmann and V. K. Yachandra, Physical Chemistry Chemical Physics **6** (20), 4864-4870 (2004).

23. U. Bergmann, P. Glatzel, J. H. Robblee, J. Messinger, C. Fernandez, R. Cinco, H. Visser, K. McFarlane, E. Bellacchio, S. Pizarro, K. Sauer, V. K. Yachandra, M. P. Klein, B. L. Cox, K. H. Nealson and S. P. Cramer, Journal of Synchrotron Radiation **8**, 199-203 (2001).

24. U. Bergmann and P. Glatzel, Photosynth. Res. **102** (2-3), 255-266 (2009).

25. P. E. Best, Journal of Chemical Physics **44** (9), 3248-& (1966).

26. A. S. Koster and H. Mendel, Journal of Physics and Chemistry of Solids **31** (11), 2523-& (1970).

27. K. Tsutsumi, H. Nakamori and K. Ichikawa, Physical Review B **13** (2), 929-933 (1976).

28. M. U. Delgado-Jaime, S. DeBeer and M. Bauer, Chemistry-a European Journal **19** (47), 15888-15897 (2013).

29. T. Okura and T. Kanazawa, Journal of Materials Science Letters **9** (7), 790-792 (1990).

30. I. Torok, T. Papp, J. Palinkas, M. Budnar, A. Muhleisen, J. Kawai and J. L. Campbell, Nuclear Instruments & Methods in Physics Research Section B-Beam Interactions with Materials and Atoms **114** (1-2), 9-14 (1996).

31. S. Fazinic, L. Mandic, M. Kavcic and I. Bozicevic, Journal of Analytical Atomic Spectrometry **26** (12), 2467-2476 (2011).

32. U. Bergmann, C. R. Horne, T. J. Collins, J. M. Workman and S. P. Cramer, Chemical Physics Letters **302** (1-2), 119-124 (1999).

33. G. Smolentsev, A. V. Soldatov, J. Messinger, K. Merz, T. Weyhermuller, U. Bergmann, Y. Pushkar, J. Yano, V. K. Yachandra and P. Glatzel, Journal of the American Chemical Society **131** (36), 13161-13167 (2009).

34. V. A. Safonov, L. N. Vykhodtseva, Y. M. Polukarov, O. V. Safonova, G. Smolentsev, M. Sikora, S. G. Eeckhout and P. Glatzel, Journal of Physical Chemistry B **110** (46), 23192-23196 (2006).

35. M. A. Beckwith, M. Roemelt, M. N. Collomb, C. DuBoc, T. C. Weng, U. Bergmann, P. Glatzel, F. Neese and S. DeBeer, Inorganic Chemistry **50** (17), 8397-8409 (2011).

36. J. C. Swarbrick, Y. Kvashnin, K. Schulte, K. Seenivasan, C. Lamberti and P. Glatzel, Inorganic Chemistry **49** (18), 8323-8332 (2010).

37. S. G. Eeckhout, O. V. Safonova, G. Smolentsev, M. Biasioli, V. A. Safonov, L. N. Vykhodtseva, M. Sikora and P. Glatzel, Journal of Analytical Atomic Spectrometry **24** (2), 215-223 (2009).

38. S. Fazinic, L. Mandic, M. Kavcic and I. Bozicevic, Spectrochimica Acta Part B-Atomic Spectroscopy **66** (6), 461-469 (2011).

39. J. B. Jones and D. S. Urch, Journal of the Chemical Society-Dalton Transactions (19), 1885-1889 (1975).

40. M. Torres Deluigi, F. M. F. de Groot, G. López-Díaz, G. Tirao, G. Stutz and J. Riveros de la Vega, The Journal of Physical Chemistry C **118** (38), 22202-22210 (2014).

41. J. N. Ullom and D. A. Bennett, Superconductor Science & Technology **28** (8), 36 (2015).

42. J. Uhlig, W. B. Doriese, J. W. Fowler, D. S. Swetz, C. Jaye, D. A. Fischer, C. D. Reintsema, D. A. Bennett, L. R. Vale, U. Mandal, G. C. O'Neil, L. Miaja-Avila, Y. I. Joe, A. El Nahhas, W. Fullagar, F. P. Gustafsson, V. Sundstrom, D. Kurunthu, G. C. Hilton, D. R. Schmidt and J. N. Ullom, Journal of Synchrotron Radiation **22**, 766-775 (2015).

43. W. H. Bragg and W. L. Bragg, Proceedings of the Royal Society of London Series a-Containing Papers of a Mathematical and Physical Character **88** (605), 428-438 (1913).

44. A. T. Macrander, V. I. Kushnir and R. C. Blasdell, Review of Scientific Instruments **66** (2), 1546-1548 (1995).

45. R. Verbeni, M. Kocsis, S. Huotari, M. Krisch, G. Monaco, F. Sette and G. Vanko, Journal of Physics and Chemistry of Solids **66** (12), 2299-2305 (2005).

46. A. H. Said, H. Sinn and R. Divan, Journal of Synchrotron Radiation **18**, 492-496 (2011).

47. H. H. Johann, Zeitschrift Fur Physik **69** (3-4), 185-206 (1931).

48. T. Johansson, Zeitschrift Fur Physik **82** (7-8), 507-528 (1933).

49. L. v. Hamos, Naturwiss. **20**, 705 (1932).

50. J. W. M. DuMond and B. B. Watson, Physical Review **46** (4), 0316-0317 (1934).

51. H. A. Rowland, Philosophical Magazine Series 5 **16** (99), 197-210 (1883).

52. P. Suortti, P. Pattison and W. Weyrich, Journal of Applied Crystallography **19**, 343-352 (1986).

53. D. B. Wittry and S. Q. Sun, Journal of Applied Physics **71** (2), 564-568 (1992).

54. H. Legall, H. Stiel, M. Schnurer, M. Pagels, B. Kanngiesser, M. Muller, B. Beckhoff, I. Grigorieva, A. Antonov, V. Arkadiev and A. Bjeoumikhov, Journal of Applied Crystallography **42**, 572-579 (2009).

55. A. P. Shevelko, Y. S. Kasyanov, O. F. Yakushev and L. V. Knight, Review of Scientific Instruments **73** (10), 3458-3463 (2002).

56. J. C. Dousse and J. Hoszowska, in *High Resolution XAS/XES: Analyzing Electronic Structures of Catalysts*, edited by J. Sa (CRC Press, Boca Raton, 2015).

57. Y. Cauchois, Journal De Physique Et Le Radium **3**, 320-336 (1932).

58. R. Caciuffo, S. Melone, F. Rustichelli and A. Boeuf, Physics Reports **152** (1), 1-71 (1987).

59. J. B. Hastings, B. M. Kincaid and P. Eisenberger, Nuclear Instruments & Methods **152** (1), 167-171 (1978).

60. V. Stojanoff, K. Hamalainen, D. P. Siddons, J. B. Hastings, L. E. Berman, S. Cramer and G. Smith, Review of Scientific Instruments **63** (1), 1125-1127 (1992).

61. T. Gog, G. T. Seidler, D. M. Casa, M. H. Upton, J. Kim, S. Stoupin, K. P. Nagle, M. Balasubramanian, R. A. Gordon, T. T. Fister, S. M. Heald, T. Toellner, J. P. Hill, D. S. Coburn, Y.-J. Kim, A. H. Said, E. E. Alp, W. Sturhahn, H. Yavas and C. A. Burns, Synchrotron Radiation News **22** (6), 12-21 (2009).

62. R. Verbeni, T. Pylkkanen, S. Huotari, L. Simonelli, G. Vanko, K. Martel, C. Henriquet and G. Monaco, Journal of Synchrotron Radiation **16**, 469-476 (2009).

63. E. Kleymenov, J. A. van Bokhoven, C. David, P. Glatzel, M. Janousch, R. Alonso-Mori, M. Studer, M. Willimann, A. Bergamaschi, B. Henrich and M. Nachtegaal, Review of Scientific Instruments **82** (6), 7 (2011).

64. D. Sokaras, T. C. Weng, D. Nordlund, R. Alonso-Mori, P. Velikov, D. Wenger, A. Garachtchenko, M. George, V. Borzenets, B. Johnson, T. Rabedeau and U. Bergmann, Review of Scientific Instruments **84** (5), 8 (2013).

65. U. Bergmann and S. P. Cramer, 1998 (unpublished).

66. R. Alonso-Mori, J. Kern, R. J. Gildea, D. Sokaras, T. C. Weng, B. Lassalle-Kaiser, R. Tran, J. Hattne, H. Laksmono, J. Hellmich, C. Glockner, N. Echols, R. G. Sierra, D. W. Schafer, J. Sellberg, C. Kenney, R. Herbst, J. Pines, P. Hart, S. Herrmann, R. W. Grosse-Kunstleve, M. J. Latimer, A. R. Fry, M. M. Messerschmidt, A. Miahnahri, M. M. Seibert, P. H. Zwart, W. E. White, P. D. Adams, M. J. Bogan, S. Boutet, G. J. Williams, A. Zouni, J. Messinger, P. Glatzel, N. K. Sauter, V. K. Yachandra, J. Yano and U.

Bergmann, Proceedings of the National Academy of Sciences of the United States of America **109** (47), 19103-19107 (2012).

67. J. Hoszowska and J. C. Dousse, Journal of Electron Spectroscopy and Related Phenomena **137**, 687-690 (2004).

68. J. Szlachetko, M. Nachtegaal, E. de Boni, M. Willimann, O. Safonova, J. Sa, G. Smolentsev, M. Szlachetko, J. A. van Bokhoven, J. C. Dousse, J. Hoszowska, Y. Kayser, P. Jagodzinski, A. Bergamaschi, B. Schmitt, C. David and A. Lucke, Review of Scientific Instruments **83** (10), 7 (2012).

69. J. Hoszowska, J. C. Dousse, J. Kern and C. Rheme, Nuclear Instruments & Methods in Physics Research Section a-Accelerators Spectrometers Detectors and Associated Equipment **376** (1), 129-138 (1996).

70. B. A. Mattern, G. T. Seidler, M. Haave, J. I. Pacold, R. A. Gordon, J. Planillo, J. Quintana and B. Rusthoven, Review of Scientific Instruments **83** (2), 023901 (2012).

71. J. I. Pacold, J. A. Bradley, B. A. Mattern, M. J. Lipp, G. T. Seidler, P. Chow, Y. Xiao, E. Rod, B. Rusthoven and J. Quintana, Journal of Synchrotron Radiation **19**, 245-251 (2012).

72. D. C. Koningsberger, in *X-Ray Absorption: Principles, Applications, Techniques of EXAFS, SEXAFS and XANES*, edited by D. C. Koningsberger and R. Prins (John Wiley & Sons, 1988), pp. 163-210.

73. E. A. Stern, D. E. Sayers and F. W. Lytle, Physical Review B **11** (12), 4836-4846 (1975).

74. D. E. Sayers, E. A. Stern and F. W. Lytle, Physical Review Letters **27** (18), 1204 (1971).

75. F. W. Lytle, D. E. Sayers and E. A. Stern, Physical Review B **11** (12), 4825-4835 (1975).

76. E. A. Stern, *Laboratory EXAFS Facilities*. (American Institute of Physics, New York, 1980).

77. K. Nishihagi, A. Kawabata and K. Taniguchi, Japanese Journal of Applied Physics Part 1-Regular Papers Short Notes & Review Papers **32**, 258-260 (1993).

78. K. Sakurai and X. M. Guo, Spectrochimica Acta Part B-Atomic Spectroscopy **54** (1), 99-107 (1999).

79. T. Taguchi, J. Harada, A. Kiku, K. Tohji and K. Shinoda, Journal of Synchrotron Radiation **8**, 363-365 (2001).

80. T. Taguchi, Q. F. Xiao and J. Harada, Journal of Synchrotron Radiation **6**, 170-171 (1999).

81. T. Taguchi, K. Shinoda and K. Tohji, Physica Scripta **T115**, 1017-1018 (2005).

82. Y. N. Yuryev, H.-J. Lee, H.-M. Park, Y.-K. Cho, M.-K. Lee and K. J. Pogrebitsky, Review of Scientific Instruments **78** (2), 025108 (2007).

83. R. Buschert, M. D. Giardina, A. Merlini, A. Balerna and S. Mobilio, Journal of Applied Crystallography **21**, 79-85 (1988).

84. A. Mosset, P. Lecante, P. Baules, J. Jaud, J. Galy and A. Burian, Acta Physica Polonica A **91** (4), 825-828 (1997).

85. P. Lecante, J. Jaud, A. Mosset, J. Galy and A. Burian, Review of Scientific Instruments **65** (4), 845-849 (1994).

86. L. Anklamm, C. Schlesiger, W. Malzer, D. Grotzsch, M. Neitzel and B. Kanngiesser, Review of Scientific Instruments **85** (5), 053110 (2014).

87. M. Szlachetko, M. Berset, J. C. Dousse, J. Hoszowska and J. Szlachetko, Review of Scientific Instruments **84** (9), 093104 (2013).

88. U. Kaminaga, T. Matsushita and K. Kohra, Japanese Journal of Applied Physics **20** (5), L355-L358 (1981).

89. L. J. Liu, T. K. Sham, H. Hayashi, N. Kanai, Y. Takehara, N. Kawamura, M. Mizumaki and R. A. Gordon, Journal of Chemical Physics **136** (19), 8 (2012).

90. H. Hayashi, Y. Takehara, N. Kawamura and M. Mizumaki, Analytical Sciences **26** (8), 885-889 (2010).

91. H. Hayashi and K. Okada, Spectrochimica Acta Part B-Atomic Spectroscopy **64** (8), 753-755 (2009).

92. H. Hayashi, N. Kawamura, M. Mizumaki and T. Takabatake, Analytical Chemistry **81** (4), 1522-1528 (2009).

93. H. Hayashi, N. Kanai, Y. Takehara, N. Kawamura, M. Mizumaki and A. Mitsuda, Journal of Analytical Atomic Spectrometry **26** (9), 1858-1862 (2011).

94. H. Hayashi, N. Kanai, N. Kawamura, M. Mizumaki, K. Imura, N. K. Sato, H. S. Suzuki and F. Iga, Journal of Analytical Atomic Spectrometry **28** (3), 373-378 (2013).

95. P. Glatzel, U. Bergmann, F. M. F. de Groot and S. P. Cramer, AIP Conference Proceedings **652** (1), 250-255 (2003).

96. L. Mandic, S. Fazinic and M. Jaksic, Physical Review A **80** (4), 10 (2009).

97. C. Sternemann, A. Kaprolat, M. H. Krisch and W. Schulke, Physical Review A **61** (2), 4 (2000).

98. H. Enkisch, C. Sternemann, M. Paulus, M. Volmer and W. Schulke, Physical Review A **70** (2), 7 (2004).

99. M. Labanowska, Chemphyschem **2** (12), 712-731 (2001).

100. A. Bruckner, Chemical Society Reviews **39** (12), 4673-4684 (2010).

101. G. J. Kennedy, M. Afeworki, D. C. Calabro, C. E. Chase and R. J. Smiley, Applied Spectroscopy **58** (6), 698-704 (2004).

102. M. Hunger and W. Wang, in *Advances in Catalysis, Vol 50*, edited by B. C. Gates and H. Knozinger (Elsevier Academic Press Inc, San Diego, 2006), Vol. 50, pp. 149-225.

103. J. M. Butler, M. W. George, J. R. Schoonover, D. M. Dattelbaum and T. J. Meyer, Coordination Chemistry Reviews **251** (3-4), 492-514 (2007).

104. A. Kudelski, Talanta **76** (1), 1-8 (2008).

105. S. Bordiga, F. Bonino, A. Damin and C. Lamberti, Physical Chemistry Chemical Physics **9** (35), 4854-4878 (2007).

106. N. Lee, T. Petrenko, U. Bergmann, F. Neese and S. DeBeer, Journal of the American Chemical Society **132** (28), 9715-9727 (2010).

107. C. J. Pollock and S. DeBeer, Journal of the American Chemical Society **133** (14), 5594-5601 (2011).

108. C. J. Pollock and S. DeBeer, Accounts of Chemical Research **48** (11), 2967-2975 (2015).

109. J. Kowalska and S. DeBeer, Biochimica Et Biophysica Acta-Molecular Cell Research **1853** (6), 1406-1415 (2015).

110. K. M. Lancaster, M. Roemelt, P. Ettenhuber, Y. L. Hu, M. W. Ribbe, F. Neese, U. Bergmann and S. DeBeer, Science **334** (6058), 974-977 (2011).

111. Y. Pushkar, J. Yano, P. Glatzel, J. Messinger, A. Lewis, K. Sauer, U. Bergmann and V. Yachandra, Journal of Biological Chemistry **282** (10), 7198-7208 (2007).

112. C. Kupitz, S. Basu, I. Grotjohann, R. Fromme, N. A. Zatsepin, K. N. Rendek, M. S. Hunter, R. L. Shoeman, T. A. White, D. J. Wang, D. James, J. H. Yang, D. E. Cobb, B. Reeder, R. G. Sierra, H. G. Liu, A. Barty, A. L. Aquila, D. Deponte, R. A. Kirian, S.

Bari, J. J. Bergkamp, K. R. Beyerlein, M. J. Bogan, C. Caleman, T. C. Chao, C. E. Conrad, K. M. Davis, H. Fleckenstein, L. Galli, S. P. Hau-Riege, S. Kassemeyer, H. Laksmono, M. N. Liang, L. Lomb, S. Marchesini, A. V. Martin, M. Messerschmidt, D. Milathianaki, K. Nass, A. Ros, S. Roy-Chowdhury, K. Schmidt, M. Seibert, J. Steinbrener, F. Stellato, L. F. Yan, C. Yoon, T. A. Moore, A. L. Moore, Y. Pushkar, G. J. Williams, S. Boutet, R. B. Doak, U. Weierstall, M. Frank, H. N. Chapman, J. C. H. Spence and P. Fromme, Nature **513** (7517), 261-+ (2014).

113. J. Yano, J. Kern, K. Sauer, M. J. Latimer, Y. Pushkar, J. Biesiadka, B. Loll, W. Saenger, J. Messinger, A. Zouni and V. K. Yachandra, Science **314** (5800), 821-825 (2006).

114. J. Yano, Y. Pushkar, P. Glatzel, A. Lewis, K. Sauer, J. Messinger, U. Bergmann and V. Yachandra, Journal of the American Chemical Society **127** (43), 14974-14975 (2005).

115. J. Yano, J. Kern, K. D. Irrgang, M. J. Latimer, U. Bergmann, P. Glatzel, Y. Pushkar, J. Biesiadka, B. Loll, K. Sauer, J. Messinger, A. Zouni and V. K. Yachandra, Proceedings of the National Academy of Sciences of the United States of America **102** (34), 12047-12052 (2005).

116. Y. Pushkar, X. Long, P. Glatzel, G. W. Brudvig, G. C. Dismukes, T. J. Collins, V. K. Yachandra, J. Yano and U. Bergmann, Angewandte Chemie-International Edition **49** (4), 800-803 (2010).

117. V. K. Yachandra, K. Sauer and M. P. Klein, Chemical Reviews **96** (7), 2927-2950 (1996).

118. A. D. Dayan and A. J. Paine, Human & Experimental Toxicology **20** (9), 439-451 (2001).

119. WHO, *Chromium (Environmental Health Criteria)*. (World Health Organization, Geneva, Switzerland, 1988).

120. EPA, *Toxicological Review of Trivalent Chromium. CAS No. 16065-83-1*. (Environmental Protection Agency, Washington, D.C., 1998).

121. M. Biasioli, R. Barberis and F. Ajmone-Marsan, Science of the Total Environment **356** (1-3), 154-164 (2006).

122. M. Biasioli, H. Grcman, T. Kralj, F. Madrid, E. Diaz-Barrientos and E. Ajmone-Marsan, Journal of Environmental Quality **36** (1), 70-79 (2007).

123. M. Biasioli and F. Ajmone-Marsan, Journal of Environmental Monitoring **9** (8), 862-868 (2007).

124. J. Sakurai, *Advanced Quantum Mechanics*. (Addison-Wesley, Reading, MA, 1967).

125. W. Schulke, *Electron Dynamics by Inelastic X-Ray Scattering* (Oxford University Press, 2007).

126. K. Gottfried and T. M. Yan, *Quantum Mechanics: Fundamentals*. (Springer-Verlag, New York, 2004).

127. F. de Groot and A. Kotani, *Core Level Spectroscopy of Solids* (CRC Press, 2008).

128. F. de Groot, Chemical Reviews **101** (6), 1779-1808 (2001).

129. F. de Groot, Coordination Chemistry Reviews **249** (1-2) (2005).

130. L. H. Thomas, Proceedings of the Cambridge Philosophical Society **23**, 542-548 (1927).

131. E. Fermi, Atti Accad.Naz.Lincei, Rend. **6**, 602-607 (1927).

132. P. Hohenberg and W. Kohn, Physical Review **136** (3B), B864-B871 (1964).

133. P. Giannozzi, S. Baroni, N. Bonini, M. Calandra, R. Car, C. Cavazzoni, D. Ceresoli, G. L. Chiarotti, M. Cococcioni, I. Dabo, A. Dal Corso, S. de Gironcoli, S. Fabris, G. Fratesi, R. Gebauer, U. Gerstmann, C. Gougoussis, A. Kokalj, M. Lazzeri, L. Martin-Samos, N. Marzari, F. Mauri, R. Mazzarello, S. Paolini, A. Pasquarello, L. Paulatto, C. Sbraccia, S.

Scandolo, G. Sclauzero, A. P. Seitsonen, A. Smogunov, P. Umari and R. M. Wentzcovitch, Journal of Physics-Condensed Matter **21** (39), 19 (2009).

134. J. Enkovaara, C. Rostgaard, J. J. Mortensen, J. Chen, M. Dulak, L. Ferrighi, J. Gavnholt, C. Glinsvad, V. Haikola, H. A. Hansen, H. H. Kristoffersen, M. Kuisma, A. H. Larsen, L. Lehtovaara, M. Ljungberg, O. Lopez-Acevedo, P. G. Moses, J. Ojanen, T. Olsen, V. Petzold, N. A. Romero, J. Stausholm-Moller, M. Strange, G. A. Tritsaris, M. Vanin, M. Walter, B. Hammer, H. Hakkinen, G. K. H. Madsen, R. M. Nieminen, J. Norskov, M. Puska, T. T. Rantala, J. Schiotz, K. S. Thygesen and K. W. Jacobsen, Journal of Physics-Condensed Matter **22** (25), 24 (2010).

135. X. Gonze, J. M. Beuken, R. Caracas, F. Detraux, M. Fuchs, G. M. Rignanese, L. Sindic, M. Verstraete, G. Zerah, F. Jollet, M. Torrent, A. Roy, M. Mikami, P. Ghosez, J. Y. Raty and D. C. Allan, Computational Materials Science **25** (3), 478-492 (2002).

136. X. Gonze, G. M. Rignanese, M. Verstraete, J. M. Beuken, Y. Pouillon, R. Caracas, F. Jollet, M. Torrent, G. Zerah, M. Mikami, P. Ghosez, M. Veithen, J. Y. Raty, V. Olevano, F. Bruneval, L. Reining, R. Godby, G. Onida, D. R. Hamann and D. C. Allan, Zeitschrift Fur Kristallographie **220** (5-6), 558-562 (2005).

137. X. Gonze, B. Amadon, P. M. Anglade, J. M. Beuken, F. Bottin, P. Boulanger, F. Bruneval, D. Caliste, R. Caracas, M. Cote, T. Deutsch, L. Genovese, P. Ghosez, M. Giantomassi, S. Goedecker, D. R. Hamann, P. Hermet, F. Jollet, G. Jomard, S. Leroux, M. Mancini, S. Mazevet, M. J. T. Oliveira, G. Onida, Y. Pouillon, T. Rangel, G. M. Rignanese, D. Sangalli, R. Shaltaf, M. Torrent, M. J. Verstraete, G. Zerah and J. W. Zwanziger, Computer Physics Communications **180** (12), 2582-2615 (2009).

138. G. Kresse and J. Furthmuller, Physical Review B **54** (16), 11169-11186 (1996).

139. K. Schwarz and P. Blaha, Computational Materials Science **28** (2), 259-273 (2003).

140. K. Schwarz, Journal of Solid State Chemistry **176** (2), 319-328 (2003).

141. J. J. Rehr, J. J. Kas, F. D. Vila, M. P. Prange and K. Jorissen, Physical Chemistry Chemical Physics **12** (21), 5503-5513 (2010).

142. J. J. Rehr, J. J. Kas, M. P. Prange, A. P. Sorini, Y. Takimoto and F. Vila, Comptes Rendus Physique **10** (6), 548-559 (2009).

143. Y. Joly, Physical Review B **63** (12), 10 (2001).

144. M. Benfatto and S. Della Longa, Journal of Synchrotron Radiation **8**, 1087-1094 (2001).

145. M. Benfatto, A. Congiu-Castellano, A. Daniele and S. D. Longa, Journal of Synchrotron Radiation **8**, 267-269 (2001).

146. F. Neese, Wiley Interdisciplinary Reviews: Computational Molecular Science **2** (1), 73-78 (2012).

147. M. Valiev, E. J. Bylaska, N. Govind, K. Kowalski, T. P. Straatsma, H. J. J. Van Dam, D. Wang, J. Nieplocha, E. Apra, T. L. Windus and W. de Jong, Computer Physics Communications **181** (9), 1477-1489 (2010).

148. G. Bunker, *Introduction to XAFS: A Practical Guide to X-ray Absorption Fine Structure Spectroscopy*. (Cambridge University Press, 2010).

149. J. Stohr, *NEXAFS Spectroscopy* (Springer, 2010).

150. L. Baggetto, E. J. M. Hensen and P. H. L. Notten, Electrochimica Acta **55** (23), 7074-7079 (2010).

151. J. R. Croy, M. Balasubramanian, D. Kim, S.-H. Kang and M. M. Thackeray, Chemistry of Materials **23** (24), 5415-5424 (2011).

152. G. de Combarieu, S. Hamelet, F. Millange, M. Morcrette, J.-M. Tarascon, G. Ferey and R. I. Walton, Electrochemistry Communications **11** (10), 1881-1884 (2009).

153. A. Deb, U. Bergmann, E. J. Cairns and S. P. Cramer, Journal of Synchrotron Radiation **11**, 497-504 (2004).

154. A. Deb, U. Bergmann, S. P. Cramer and E. J. Cairns, Journal of the Electrochemical Society **154** (6), A534-A541 (2007).

155. A. Deb and E. J. Cairns, Fluid Phase Equilibria **241** (1-2), 4-19 (2006).

156. R. Dominko, I. Arcon, A. Kodre, D. Hanzel and M. Gaberscek, Journal of Power Sources **189** (1), 51-58 (2009).

157. H. Kobayashi, Y. Takenaka, Y. Arachi, H. Nitani, T. Okumura, M. Shikano, H. Kageyama and K. Tatsumi, Solid State Ionics **225**, 580-584 (2012).

158. S. Kobayashi, I. R. M. Kottegoda, Y. Uchimoto and M. Wakihara, Journal of Materials Chemistry **14** (12), 1843-1848 (2004).

159. J. B. Leriche, S. Hamelet, J. Shu, M. Morcrette, C. Masquelier, G. Ouvrard, M. Zerrouki, P. Soudan, S. Belin, E. Elkaim and F. Baudelet, Journal of the Electrochemical Society **157** (5), A606-A610 (2010).

160. T. Nedoseykina, M. G. Kim, S.-A. Park, H.-S. Kim, S.-B. Kim, J. Cho and Y. Lee, Electrochimica Acta **55** (28), 8876-8882 (2010).

161. T. Nonaka, C. Okuda, Y. Seno, H. Nakano, K. Koumoto and Y. Ukyo, Journal of Power Sources **162** (2), 1329-1335 (2006).

162. Y. Shiraishi, I. Nakai, T. Tsubata, T. Himeda and F. Nishikawa, Journal of Solid State Chemistry **133** (2), 587-590 (1997).

163. L. Simonin, J.-F. Colin, V. Ranieri, E. Canevet, J.-F. Martin, C. Bourbon, C. Baehtz, P. Strobel, L. Daniel and S. Patoux, Journal of Materials Chemistry **22** (22), 11316-11322 (2012).

164. Y. Terada, K. Yasaka, F. Nishikawa, T. Konishi, M. Yoshio and I. Nakai, Journal of Solid State Chemistry **156** (2), 286-291 (2001).

165. Y. W. Tsai, B. J. Hwang, G. Ceder, H. S. Sheu, D. G. Liu and J. F. Lee, Chemistry of Materials **17** (12), 3191-3199 (2005).

166. W. S. Yoon, C. P. Grey, M. Balasubramanian, X. Q. Yang and J. McBreen, Chemistry of Materials **15** (16), 3161-3169 (2003).

167. W. S. Yoon, Y. Paik, X. Q. Yang, M. Balasubramanian, J. McBreen and C. P. Grey, Electrochemical and Solid State Letters **5** (11), A263-A266 (2002).

168. W.-S. Yoon, K. Y. Chung, K.-W. Nam, J. McBreen, D. Wang, X. Huang, H. Li, L. Chen and X.-Q. Yang, Journal of Power Sources **183** (1), 427-430 (2008).

169. P.-F. Yu, Z.-H. Cui, J.-W. Meng and X.-X. Guo, Chinese Physics Letters **30** (3), 036102 (2013).

170. W. Zhang, P. N. Duchesne, Z.-L. Gong, S.-Q. Wu, L. Ma, Z. Jiang, S. Zhang, P. Zhang, J.-X. Mi and Y. Yang, Journal of Physical Chemistry C **117** (22), 11498-11505 (2013).

171. X. Zhang, M. Gao, Y. Gu, H. Bao, X. Li, X. Zhou and W. Wen, Journal of Physical Chemistry C **116** (38), 20230-20238 (2012).

172. S. R. Bare, S. D. Kelly, B. Ravel, N. Greenlay, L. King and G. E. Mickelson, Physical Chemistry Chemical Physics **12** (27), 7702-7711 (2010).

173. T. B. Bolin, T. Wu, N. Schweitzer, R. Lobo-Lapidus, A. J. Kropf, H. Wang, Y. Hu, J. T. Miller and S. M. Heald, Catalysis Today **205**, 141-147 (2013).

174. W.-F. Chen, K. Sasaki, C. Ma, A. I. Frenkel, N. Marinkovic, J. T. Muckerman, Y. Zhu and R. R. Adzic, Angewandte Chemie-International Edition **51** (25), 6131-6135 (2012).

175. A. J. Dent, Topics in Catalysis **18** (1-2), 27-35 (2002).

176. A. I. Frenkel, Chemical Society Reviews **41** (24), 8163-8178 (2012).

177. A. I. Frenkel, M. W. Cason, A. Elsen, U. Jung, M. W. Small, R. G. Nuzzo, F. D. Vila, J. J. Rehr, E. A. Stach and J. C. Yang, Journal of Vacuum Science & Technology A **32** (2), 020801 (2014).

178. A. I. Frenkel, J. A. Rodriguez and J. G. Chen, Acs Catalysis **2** (11), 2269-2280 (2012).

179. J. D. Grunwaldt and B. S. Clausen, Topics in Catalysis **18** (1-2), 37-43 (2002).

180. J. D. Grunwaldt, S. Hannemann, J. Goettlicher, S. Mangold, M. A. Denecke and A. Baiker, Physica Scripta **T115**, 769-772 (2005).

181. S. Hannemann, M. Casapu, J.-D. Grunwaldt, P. Haider, P. Trussel, A. Baiker and E. Welter, Journal of Synchrotron Radiation **14**, 345-354 (2007).

182. C. La Fontaine, L. Barthe, A. Rochet and V. Briois, Catalysis Today **205**, 148-158 (2013).

183. J. Ohyama, K. Teramura, Y. Higuchi, T. Shishido, Y. Hitomi, K. Kato, H. Tanida, T. Uruga and T. Tanaka, Chemphyschem **12** (1), 127-131 (2011).

184. A. Patlolla, P. Baumann, W. Xu, S. D. Senanayake, J. A. Rodriguez and A. I. Frenkel, Topics in Catalysis **56** (11), 896-904 (2013).

185. A. Patlolla, E. V. Carino, S. N. Ehrlich, E. Stavitski and A. I. Frenkel, Acs Catalysis **2** (11), 2216-2223 (2012).

186. C. Prestipino, O. Mathon, R. Hino, A. Beteva and S. Pascarelli, Journal of Synchrotron Radiation **18**, 176-182 (2011).

187. D. E. Ramaker and D. C. Koningsberger, Physical Chemistry Chemical Physics **12** (21), 5514-5534 (2010).

188. A. Stierle and A. M. Molenbroek, Mrs Bulletin **32** (12), 1001-1005 (2007).

189. J. M. Thomas and G. Sankar, Accounts of Chemical Research **34** (7), 571-581 (2001).

190. J. M. Thomas and G. Sankar, Journal of Synchrotron Radiation **8**, 55-60 (2001).

191. S. J. Tinnemans, J. G. Mesu, K. Kervinen, T. Visser, T. A. Nijhuis, A. M. Beale, D. E. Keller, A. M. J. van der Eerden and B. M. Weckhuysen, Catalysis Today **113** (1-2), 3-15 (2006).

192. L. Wang, S. Zhang, Y. Zhu, A. Patlolla, J. Shan, H. Yoshida, S. Takeda, A. I. Frenkel and F. Tao, Acs Catalysis **3** (5), 1011-1019 (2013).

193. Y. Inada and S. Funahashi, Review of Scientific Instruments **65** (1), 18-24 (1994).

194. Y. Inada and S. Funahashi, Zeitschrift Fur Naturforschung Section B-a Journal of Chemical Sciences **52** (6), 711-718 (1997).

195. J. C. Lee, S. A. Song, Y. Yuryev, Y. Terada, I. Nakai and C. B. Lim, Journal of Synchrotron Radiation **8**, 360-362 (2001).

196. A. T. Shuvaev, B. Y. Helmer, T. A. Lyubeznova and V. A. Shuvaeva, Journal of Synchrotron Radiation **6**, 158-160 (1999).

197. Y. N. Yuryev, H. J. Lee, J. H. Kim, Y. K. Cho, M. K. Lee and K. J. Pogrebitsky, X-Ray Spectrometry **37** (5), 476-481 (2008).

198. H. Kageyama, H. Shigemura, M. Tabuchi, K. Ado and H. Kobayashi, Journal of Synchrotron Radiation **8**, 863-865 (2001).

199. V. L. McLarcn, A. R. West, M. Tabuchi, A. Nakashima, H. Takahara, H. Kobayashi, H. Sakaebe, H. Kageyama, A. Hirano and Y. Takedac, Journal of the Electrochemical Society **151** (5), A672-A681 (2004).

200. H. Shigemura, H. Sakaebe, H. Kageyama, H. Kobayashi, A. R. West, R. Kanno, S. Morimoto, S. Nasu and M. Tabuchi, Journal of the Electrochemical Society **148** (7), A730-A736 (2001).

201. M. Tabuchi, A. Nakashima, H. Shigemura, K. Ado, H. Kobayashi, H. Sakaebe, H. Kageyama, T. Nakamura, M. Kohzaki, A. Hirano and R. Kanno, Journal of the Electrochemical Society **149** (5), A509-A524 (2002).

202. Y. Kayser, W. Blachucki, J. C. Dousse, J. Hoszowska, M. Neff and V. Romano, Review of Scientific Instruments **85** (4), 043101 (2014).

203. H.-W. Chan, J.-G. Duh and J.-F. Lee, Electrochemistry Communications **8** (11), 1731-1736 (2006).

204. A. Deb, U. Bergmann, E. J. Cairns and S. P. Cramer, Journal of Physical Chemistry B **108** (22), 7046-7049 (2004).

205. A. Deb, U. Bergmann, S. P. Cramer and E. J. Cairns, Journal of Applied Physics **97** (11), 113523 (2005).

206. S. Hayakawa, Y. Kubouchi, T. Hayashi, T. Onakado, H. Namatame and T. Hirokawa, Electrochemistry **78** (5), 454-456 (2010).

207. M. Holzapfel, O. Proux, P. Strobel, C. Darie, M. Borowski and M. Morcrette, Journal of Materials Chemistry **14** (1), 102-110 (2004).

208. F. Huguenin, E. A. Ticianelli and R. M. Torresi, Electrochimica Acta **47** (19), 3179-3186 (2002).

209. C. T. Love, A. Korovina, C. J. Patridge, K. E. Swider-Lyons, M. E. Twigg and D. E. Ramaker, Journal of the Electrochemical Society **160** (5), A3153-A3161 (2013).

210. M. C. Menard, A. C. Marschilok, K. J. Takeuchi and E. S. Takeuchi, Electrochimica Acta **94**, 320-326 (2013).

211. G. Ouvrard, N. Bourgeon, D. Guyomard, F. Baudelet and S. Belin, Physica Scripta **T115**, 346-348 (2005).

212. M. Shikano, H. Kobayashi, S. Koike, H. Sakaebe, Y. Saito, H. Hori, H. Kageyama and K. Tatsumi, Journal of Power Sources **196** (16), 6881-6883 (2011).

213. M. E. Bowden, K. J. Alvine, J. L. Fulton, J. R. Lemmon, X. Lu, B.-J. Webb-Robertson, S. M. Heald, M. Balasubramanian, D. R. Mortensen, G. T. Seidler and N. J. Hess, Journal of Power Sources **247**, 517-526 (2014).

214. C. S. Johnson, S. H. Kang, J. T. Vaughey, S. V. Pol, M. Balasubramanian and M. M. Thackeray, Chemistry of Materials **22** (3), 1263-1270 (2010).

215. H. Sugie, M. Tanemura, V. Filip, K. Iwata, K. Takahashi and F. Okuyama, Applied Physics Letters **78** (17), 2578-2580 (2001).

216. G. Z. Yue, Q. Qiu, B. Gao, Y. Cheng, J. Zhang, H. Shimoda, S. Chang, J. P. Lu and O. Zhou, Applied Physics Letters **81** (2), 355-357 (2002).

217. G. S. Knapp, H. Chen and T. E. Klippert, Review of Scientific Instruments **49** (12), 1658-1666 (1978).

218. G. G. Cohen, D. A. Fischer, J. Colbert and N. J. Shevchik, Review of Scientific Instruments **51** (3), 273-277 (1980).

219. P. Georgopoulos and G. S. Knapp, Journal of Applied Crystallography **14** (FEB), 3-7 (1981).

220. K. Tohji, Y. Udagawa, T. Kawasaki and K. Masuda, Review of Scientific Instruments **54** (11), 1482-1487 (1983).

221. W. Thulke, R. Haensel and P. Rabe, Review of Scientific Instruments **54** (3), 277-283 (1983).

222. A. Williams, Review of Scientific Instruments **54** (2), 193-197 (1983).

223. U. Bergmann, P. Glatzel, F. deGroot and S. P. Cramer, Journal of the American Chemical Society **121** (20), 4926-4927 (1999).

224. U. Bergmann, M. M. Grush, C. R. Horne, P. DeMarois, J. E. Penner-Hahn, C. F. Yocum, D. W. Wright, C. E. Dube, W. H. Armstrong, G. Christou, H. J. Eppley and S. P. Cramer, Journal of Physical Chemistry B **102** (42), 8350-8352 (1998).

225. K. M. Davis, I. Kosheleva, R. W. Henning, G. T. Seidler and Y. Pushkar, Journal of Physical Chemistry B **117** (31), 9161-9169 (2013).

226. K. M. Davis, B. A. Mattern, J. I. Pacold, T. Zakharova, D. Brewe, I. Kosheleva, R. W. Henning, T. J. Graber, S. M. Heald, G. T. Seidler and Y. Pushkar, Journal of Physical Chemistry Letters **3** (14), 1858-1864 (2012).

227. S. K. Deshpande, S. M. Chaudhari, A. Pimpale, A. S. Nigavekar, S. B. Ogale and V. G. Bhide, Pramana-Journal of Physics **37** (4), 373-385 (1991).

228. M. Ito and H. Iwasaki, Japanese Journal of Applied Physics Part 1-Regular Papers Short Notes & Review Papers **22** (2), 357-360 (1983).

229. S. Khalid, R. Emrich, R. Dujari, J. Shultz and J. R. Katzer, Review of Scientific Instruments **53** (1), 22-33 (1982).

230. G. S. Knapp, A. G. McKale, J. Quintana and T. Georgopoulos, Physica B **158** (1-3), 328-329 (1989).

231. K. Tohji and Y. Udagawa, Japanese Journal of Applied Physics Part 1-Regular Papers Short Notes & Review Papers **22** (5), 882-885 (1983).

232. K. Tohji, Y. Udagawa, T. Kawasaki and K. Mieno, Review of Scientific Instruments **59** (7), 1127-1131 (1988).

233. Y. Yacoby, M. Brettschneider and M. Bezalel, Review of Scientific Instruments **58** (4), 588-592 (1987).

234. T. Gog, D. M. Casa, A. H. Said, M. H. Upton, J. Kim, I. Kuzmenko, X. R. Huang and R. Khachatryan, Journal of Synchrotron Radiation **20**, 74-79 (2013).

235. T. T. Fister, G. T. Seidler, L. Wharton, A. R. Battle, T. B. Ellis, J. O. Cross, A. T. Macrander, W. T. Elam, T. A. Tyson and Q. Qian, Review of Scientific Instruments **77** (6), 063901 (2006).

236. M. Newville, in *The XAFS Model Compound Library* (Co foil, 2001; http://cars9.uchicago.edu/~newville/ModelLib/).

237. L. G. Parratt, C. F. Hempstead and E. L. Jossem, Physical Review **105** (4), 1228-1232 (1957).

238. M. D. de Jonge, Z. Barnea, C. Q. Tran and C. T. Chantler, Physical Review A **69** (2), 022717 (2004).

239. J. L. Glover and C. T. Chantler, Measurement Science & Technology **18** (9), 2916-2920 (2007).

240. X. Gao, S. Q. Gu, Q. Gao, Y. Zou, Z. Jiang, S. Zhang, X. J. Wei, H. S. Yu, G. D. Sheng, P. Q. Duan and Y. Y. Huang, X-Ray Spectrometry **42** (6), 502-507 (2013).

241. J.-L. Hazemann, O. Proux, V. Nassif, H. Palancher, E. Lahera, C. Da Silva, A. Braillard, D. Testemale, M.-A. Diot, I. Alliot, W. Del Net, A. Manceau, F. Gelebart, M. Morand, Q. Dermigny and A. Shukla, Journal of Synchrotron Radiation **16**, 283-292 (2009).

242. J. P. Hill, D. S. Coburn, Y. J. Kim, T. Gog, D. M. Casa, C. N. Kodituwakku and H. Sinn, Journal of Synchrotron Radiation **14**, 361-365 (2007).

243. A. P. Honkanen, R. Verbeni, L. Simonelli, M. M. Sala, G. Monaco and S. Huotari, Journal of Synchrotron Radiation **21**, 104-110 (2014).

244. E. Kleymenov, J. A. van Bokhoven, C. David, P. Glatzel, M. Janousch, R. Alonso-Mori, M. Studer, M. Willimann, A. Bergamaschi, B. Henrich and M. Nachtegaal, Rev. Sci. Instrum. **82** (6), 065107 (2011).

245. I. Llorens, E. Lahera, W. Delnet, O. Proux, A. Braillard, J. L. Hazemann, A. Prat, D. Testemale, Q. Dermigny, F. Gelebart, M. Morand, A. Shukla, N. Bardou, O. Ulrich, S. Arnaud, J. F. Berar, N. Boudet, B. Caillot, P. Chaurand, J. Rose, E. Doelsch, P. Martin and P. L. Solari, Review of Scientific Instruments **83** (6), 063104 (2012).

246. D. Sokaras, D. Nordlund, T. C. Weng, R. A. Mori, P. Velikov, D. Wenger, A. Garachtchenko, M. George, V. Borzenets, B. Johnson, Q. Qian, T. Rabedeau and U. Bergmann, Review of Scientific Instruments **83** (4), 043112 (2012).

247. D. Sokaras, T. C. Weng, D. Nordlund, R. Alonso-Mori, P. Velikov, D. Wenger, A. Garachtchenko, M. George, V. Borzenets, B. Johnson, T. Rabedeau and U. Bergmann, Rev. Sci. Instrum. **84** (5), 053102 (2013).

248. E. Gallo and P. Glatzel, Adv. Mater. **26** (46), 7730-7746 (2014).

249. M. Kavcic, M. Budnar, A. Muhleisen, F. Gasser, M. Zitnik, K. Bucar and R. Bohinc, Review of Scientific Instruments **83** (6), 1 (2012).

250. G. T. Seidler, D. R. Mortensen, A. J. Remesnik, J. I. Pacold, N. A. Ball, N. Barry, M. Styczinski and O. R. Hoidn, Review of Scientific Instruments **85** (11), 12 (2014).

251. C. Masciovecchio, U. Bergmann, M. Krisch, G. Ruocco, F. Sette and R. Verbeni, Nuclear Instruments & Methods in Physics Research Section B-Beam Interactions with Materials and Atoms **111** (1-2), 181-186 (1996).

252. R. Verbeni, F. Sette, M. H. Krisch, U. Bergmann, B. Gorges, C. Halcoussis, K. Martel, C. Masciovecchio, J. F. Ribois, G. Ruocco and H. Sinn, Journal of Synchrotron Radiation **3**, 62-64 (1996).

253. H. Sinn, E. E. Alp, A. Alatas, J. Barraza, G. Bortel, E. Burkel, D. Shu, W. Sturhahn, J. P. Sutter, T. S. Toellner and J. Zhao, Nuclear Instruments & Methods in Physics Research Section a-Accelerators Spectrometers Detectors and Associated Equipment **467**, 1545-1548 (2001).

254. C. C. Kao, K. Hamalainen, M. Krisch, D. P. Siddons, T. Oversluizen and J. B. Hastings, Review of Scientific Instruments **66** (2), 1699-1702 (1995).

255. M. Schwoerer-Bohning, A. T. Macrander, P. M. Abbamonte and D. A. Arms, Review of Scientific Instruments **69** (9), 3109-3112 (1998).

256. T. T. Fister, G. T. Seidler, L. Wharton, A. R. Battle, T. B. Ellis, J. O. Cross, A. T. Macrander, W. T. Elam, T. A. Tyson and Q. Qian, Review of Scientific Instruments **77** (6), 7 (2006).

257. Y. V. Shvyd'ko, J. P. Hill, C. A. Burns, D. S. Coburn, B. Brajuskovic, D. Casa, K. Goetze, T. Gog, R. Khachatryan, J. H. Kim, C. N. Kodituwakku, M. Ramanathan, T. Roberts, A. Said, H. Sinn, D. Shu, S. Stoupin, M. Upton, M. Wieczorek and H. Yavas, Journal of Electron Spectroscopy and Related Phenomena **188**, 140-149 (2013).

258. G. T. Seidler, D. R. Mortensen, A. S. Ditter, N. A. Ball and A. J. Remesnik, Journal of Physics: Conference Series **712** (1), 012015 (2016).

259. D. R. Mortensen, G. T. Seidler, A. S. Ditter and P. Glatzel, Journal of Physics: Conference Series **712** (1), 012036 (2016).

260. D. S. Covita, M. Ay, S. Schlesser, D. Gotta, L. M. Simons, E. O. Le Bigot and J. M. F. dos Santos, Review of Scientific Instruments **79** (3), 3 (2008).

261. E. Collart, A. Shukla, F. Gelebart, M. Morand, C. Malgrange, N. Bardou, A. Madouri and J. L. Pelouard, Journal of Synchrotron Radiation **12**, 473-478 (2005).

262. A. P. Honkanen, R. Verbeni, L. Simonelli, M. M. Sala, A. Al-Zein, M. Krisch, G. Monaco and S. Huotari, Journal of Synchrotron Radiation **21**, 762-767 (2014).

263. M. de Broglie, Comptes Rendus Hebdomadaires Des Seances De L Academie Des Sciences **157**, 924-926 (1913).

264. E. M. Rowe and F. E. Mills, Particle Accelerators **4** (4), 211-227 (1973).

265. S. Doniach, K. Hodgson, I. Lindau, P. Pianetta and H. Winick, Journal of Synchrotron Radiation **4**, 380-395 (1997).

266. K. R. Lea, Physics Reports-Review Section of Physics Letters **43** (8), 337-375 (1978).

267. D. H. Bilderback, P. Elleaume and E. Weckert, Journal of Physics B: Atomic, Molecular and Optical Physics **38** (9), S773 (2005).

268. B. G. Levi, Physics Today;(United States) **44** (4) (1991).

269. B. W. McNeil and N. R. Thompson, Nature photonics **4** (12), 814-821 (2010).

270. J. J. Kas, K. Jorissen and J. J. Rehr, in *X-Ray Absorption and X-Ray Emission Spectroscopy* (John Wiley & Sons, Ltd, 2016), pp. 51-72.

271. D. E. Sayers, F. W. Lytle and E. A. Stern, *Advances in X-ray Analysis*. (Plenum, New York, 1970).

272. C. A. Ashley and S. Doniach, Physical Review B **11** (4), 1279-1288 (1975).

273. P. A. Lee and J. B. Pendry, Physical Review B **11** (8), 2795-2811 (1975).

274. P. A. Lee and G. Beni, Physical Review B **15** (6), 2862-2883 (1977).

275. B. K. Teo and P. A. Lee, Journal of the American Chemical Society **101** (11), 2815-2832 (1979).

276. S. J. Gurman, N. Binsted and I. Ross, Journal of Physics C-Solid State Physics **17** (1), 143-151 (1984).

277. S. J. Gurman, N. Binsted and I. Ross, Journal of Physics C-Solid State Physics **19** (11), 1845-1861 (1986).

278. C. R. Natoli, M. Benfatto and S. Doniach, Physical Review A **34** (6), 4682-4694 (1986).

279. J. J. Rehr and R. C. Albers, Physical Review B **41** (12), 8139-8149 (1990).

280. J. J. Rehr and R. C. Albers, Reviews of Modern Physics **72** (3), 621-654 (2000).

281. G. Onida, L. Reining and A. Rubio, Reviews of Modern Physics **74** (2), 601-659 (2002).

282. T. E. Westre, P. Kennepohl, J. G. DeWitt, B. Hedman, K. O. Hodgson and E. I. Solomon, Journal of the American Chemical Society **119** (27), 6297-6314 (1997).

283. M. A. Arrio, S. Rossano, C. Brouder, L. Galoisy and G. Calas, Europhysics Letters **51** (4), 454-460 (2000).

284. E. L. Shirley, Journal of Electron Spectroscopy and Related Phenomena **136** (1-2), 77-83 (2004).

285. F. Farges, Physical Review B **71** (15), 14 (2005).

286. S. D. George, P. Brant and E. I. Solomon, Journal of the American Chemical Society **127** (2), 667-674 (2005).

287. T. Yamamoto, X-Ray Spectrometry **37** (6), 572-584 (2008).

288. S. DeBeer George, P. Brant and E. I. Solomon, Journal of the American Chemical Society **127** (2), 667-674 (2005).

289. S. T. Liu, L. Wang, R. Ohnishi and M. Ichikawa, Journal of Catalysis **181** (2), 175-188 (1999).

290. W. Li, G. D. Meitzner, R. W. Borry and E. Iglesia, Journal of Catalysis **191** (2), 373-383 (2000).

291. M. Fernandez-Garcia, Catalysis Reviews-Science and Engineering **44** (1), 59-121 (2002).

292. S. T. Oyama, X. Wang, Y. K. Lee, K. Bando and F. G. Requejo, Journal of Catalysis **210** (1), 207-217 (2002).

293. G. Jacobs, T. K. Das, P. M. Patterson, J. Li, L. Sanchez and B. H. Davis, Applied Catalysis A: General **247** (2), 335-343 (2003).

294. Y. S. Chen, J. L. Fulton, J. C. Linehan and T. Autrey, Journal of the American Chemical Society **127** (10), 3254-3255 (2005).

295. W. J. Song, M. S. Seo, S. DeBeer, T. Ohta, R. Song, M. J. Kang, T. Tosha, T. Kitagawa, E. I. Solomon and W. Nam, Journal of the American Chemical Society **129** (5), 1268-1277 (2007).

296. J. Singh, C. Lamberti and J. A. van Bokhoven, Chemical Society Reviews **39** (12), 4754-4766 (2010).

297. J. Corker, F. Lefebvre, C. Lécuyer and V. Dufaud, Science **271** (5251), 966 (1996).

298. I. Nakai, K. Takahashi, Y. Shiraishi, T. Nakagome and F. Nishikawa, Journal of Solid State Chemistry **140** (1), 145-148 (1998).

299. I. Nakai and T. Nakagome, Electrochemical and Solid State Letters **1** (6), 259-261 (1998).

300. H. Ota, T. Akai, H. Namita, S. Yamaguchi and M. Nomura, Journal of Power Sources **119**, 567-571 (2003).

301. Y. Itou and Y. Ukyo, Journal of Power Sources **146** (1-2), 39-44 (2005).

302. N. Yabuuchi, Y. Koyama, N. Nakayama and T. Ohzuku, Journal of the Electrochemical Society **152** (7), A1434-A1440 (2005).

303. D. Asakura, E. Hosono, H. Niwa, H. Kiuchi, J. Miyawaki, Y. Nanba, M. Okubo, H. Matsuda, H. S. Zhou, M. Oshima and Y. Harada, Electrochemistry Communications **50**, 93-96 (2015).

304. H. Niwa, M. Saito, M. Kobayashi, Y. Harada, M. Oshima, S. Moriya, K. Matsubayashi, Y. Nabae, S. Kuroki, T. Ikeda, K. Terakura, J. Ozaki and S. Miyata, Journal of Power Sources **223**, 30-35 (2013).

305. C. Werkheiser, (University of Washington, Seattle, 2015).

306. J. A. Bearden and C. H. Shaw, Physical Review **48** (1), 18-30 (1935).

307. J. A. Bearden and H. Friedman, Physical Review **58** (5), 387-395 (1940).

308. J. A. Bearden and W. W. Beeman, Physical Review **58** (5), 396-399 (1940).

309. M. U. Delgado-Jaime, C. P. Mewis and P. Kennepohl, Journal of Synchrotron Radiation **17**, 132-137 (2010).

310. M. U. Delgado-Jaime and P. Kennepohl, Journal of Synchrotron Radiation **17**, 119-128 (2010).

311. J. P. Perdew, K. Burke and M. Ernzerhof, Physical Review Letters **77** (18), 3865-3868 (1996).

312. J. P. Perdew, International Journal of Quantum Chemistry, 497-523 (1985).

313. J. J. Rehr, Radiation Physics and Chemistry **75** (11), 1547-1558 (2006).

314. Y. Zhang, S. Mukamel, M. Khalil and N. Govind, Journal of Chemical Theory and Computation **11** (12), 5804-5809 (2015).

315. W. R. Wadt and P. J. Hay, Journal of Chemical Physics **82** (1), 284-298 (1985).

316. P. J. Hay and W. R. Wadt, Journal of Chemical Physics **82** (1), 270-283 (1985).

317. P. J. Hay and W. R. Wadt, Journal of Chemical Physics **82** (1), 299-310 (1985).

318. T. H. Dunning and P. J. Hay, *In Modern Theoretical Chemistry*. (Plenum, New York, 1977).

319. T. Noro, M. Sekiya and T. Koga, Theoretical Chemistry Accounts **131** (2), 8 (2012).

320. C. Adamo and V. Barone, Journal of Chemical Physics **110** (13), 6158-6170 (1999).

321. E. Carlsson, Zeitschrift Fur Physik **80** (9-10), 604-609 (1933).

322. J. H. Scofield, Atomic Data and Nuclear Data Tables **14** (2), 121-137 (1974).

323. S. D. George, T. Petrenko and F. Neese, Journal of Physical Chemistry A **112** (50), 12936-12943 (2008).

324. J. P. Rueff and A. Shukla, Reviews of Modern Physics **82** (1), 847-896 (2010).

325. B. R. Maddox, A. Lazicki, C. S. Yoo, V. Iota, M. Chen, A. K. McMahan, M. Y. Hu, P. Chow, R. T. Scalettar and W. E. Pickett, Physical Review Letters **96** (21), 215701 (2006).

326. M. J. Lipp, A. P. Sorini, J. Bradley, B. Maddox, K. T. Moore, H. Cynn, T. P. Devereaux, Y. Xiao, P. Chow and W. J. Evans, Physical Review Letters **109** (19), 195705 (2012).

327. J. A. Bradley, K. T. Moore, G. van der Laan, J. P. Bradley and R. A. Gordon, Physical Review B **84** (20), 205105 (2011).

328. W. Schulke and H. Nagasawa, Nuclear Instruments & Methods in Physics Research Section a-Accelerators Spectrometers Detectors and Associated Equipment **222** (1-2), 203-206 (1984).

329. A. Kotani and S. Shin, Reviews of Modern Physics **73** (1), 203-246 (2001).

330. L. J. P. Ament, M. van Veenendaal, T. P. Devereaux, J. P. Hill and J. van den Brink, Reviews of Modern Physics **83** (2), 705-767 (2011).

331. M. Cotte, J. Szlachetko, S. Lahlil, M. Salome, V. A. Sole, I. Biron and J. Susini, Journal of Analytical Atomic Spectrometry **26** (5), 1051-1059 (2011).

332. J. Szlachetko, M. Cotte, J. Morse, M. Salome, P. Jagodzinski, J. C. Dousse, J. Hoszowska, Y. Kayser and J. Susini, Journal of Synchrotron Radiation **17**, 400-408 (2010).

333. J. Hoszowska, J. C. Dousse, J. Szlachetko, Y. Kayser, W. Cao, P. Jagodzinski, M. Kavcic and S. H. Nowak, Physical Review Letters **107** (5), 053001 (2011).

334. S. Lahlil, M. Cotte, I. Biron, J. Szlachetko, N. Menguy and J. Susini, Journal of Analytical Atomic Spectrometry **26** (5), 1040-1050 (2011).

335. S. Heald, G. T. Seidler, D. Mortensen, B. Mattern, J. A. Bradley, N. Hess and M. Bowden, Proc. SPIE, Advances in X-Ray/EUV Optics and Components VII **8502**, 85020I (2012).

336. T. Gog, D. M. Casa, A. Said, M. H. Upton, J. Kim, I. Kuzmenko, X. Huang and R. Khachatryan, Journal of Synchrotron Radiation **20**, 74-79 (2013).

337. F. T. Edelmann, Chemical Society Reviews **41** (23), 7657-7672 (2012).

338. B. T. Kilbourn, Journal of the Less-Common Metals **126**, 101-106 (1986).

339. M. Shibasaki and N. Yoshikawa, Chemical Reviews **102** (6), 2187-2209 (2002).

340. J. G. Bednorz and K. A. Muller, Zeitschrift Fur Physik B-Condensed Matter **64** (2), 189-193 (1986).

341. A. L. Ivanovskii, Physics-Uspekhi **51** (12), 1229-1260 (2008).

342. J. P. Chen, S. Patil, S. Seal and J. F. McGinnis, Nature Nanotechnology **1** (2), 142-150 (2006).

343. C. Bouzigues, T. Gacoin and A. Alexandrou, Acs Nano **5** (11), 8488-8505 (2011).

344. M. Imada, A. Fujimori and Y. Tokura, Reviews of Modern Physics **70** (4), 1039-1263 (1998).

345. C. Pfleiderer, Reviews of Modern Physics **81** (4), 1551-1624 (2009).

346. P. Chandra, P. Coleman, J. A. Mydosh and V. Tripathi, Nature **417** (6891), 831-834 (2002).

347. P. W. Bridgman, Proceedings of the American Academy of Arts and Sciences **62** (8), 207-226 (1927).

348. P. W. Bridgman, Proceedings of the American Academy of Arts and Sciences **76** (3), 71-87 (1948).

349. A. W. Lawson and T. Y. Tang, Physical Review **76** (2), 301-302 (1949).

350. B. Johansson, Philosophical Magazine **30** (3), 469-482 (1974).

351. B. Johansson, Physical Review B **11** (8), 2740-2743 (1975).

352. J. W. Allen and R. M. Martin, Physical Review Letters **49** (15), 1106-1110 (1982).

353. M. Lavagna, C. Lacroix and M. Cyrot, Physics Letters A **90** (4), 210-212 (1982).

354. J. W. Allen and L. Z. Liu, Physical Review B **46** (9), 5047-5054 (1992).

355. A. K. McMahan, K. Held and R. T. Scalettar, Physical Review B **67** (7), 18 (2003).

356. K. Held, A. K. McMahan and R. T. Scalettar, Physical Review Letters **87** (27), 4 (2001).

357. K. Haule, V. Oudovenko, S. Y. Savrasov and G. Kotliar, Physical Review Letters **94** (3), 4 (2005).

358. M. J. Lipp, D. Jackson, H. Cynn, C. Aracne, W. J. Evans and A. K. McMahan, Physical Review Letters **101** (16), 4 (2008).

359. B. Johansson, A. V. Ruban and I. A. Abrikosov, Physical Review Letters **102** (18), 1 (2009).

360. D. R. Mortensen, G. T. Seidler, J. A. Bradley, M. J. Lipp, W. J. Evans, P. Chow, Y. M. Xiao, G. Boman and M. E. Bowden, Review of Scientific Instruments **84** (8), 4 (2013).

361. W. B. Holzapfel, Journal of Alloys and Compounds **223** (2), 170-173 (1995).

362. A. K. McMahan, C. Huscroft, R. T. Scalettar and E. L. Pollock, Journal of Computer-Aided Materials Design **5** (1998).

363. A. Lindbaum, S. Heathman, T. Le Bihan, R. G. Haire, M. Idiri and G. H. Lander, Journal of Physics-Condensed Matter **15** (28), S2297-S2303 (2003).

364. J. S. Olsen, L. Gerward, U. Benedict and J. P. Itie, Physica B & C **133** (2-3), 129-137 (1985).

365. Y. K. Vohra, S. L. Beaver, J. Akella, C. A. Ruddle and S. T. Weir, Journal of Applied Physics **85** (4), 2451-2453 (1999).

366. H. K. Mao, R. M. Hazen, P. M. Bell and J. Wittig, Journal of Applied Physics **52** (7), 4572-4574 (1981).

367. G. S. Smith and J. Akella, Journal of Applied Physics **53** (12), 9212-9213 (1982).

368. B. J. Baer, H. Cynn, V. Iota, C. S. Yoo and G. Y. Shen, Physical Review B **67** (13), 7 (2003).

369. G. N. Chesnut and Y. K. Vohra, Physical Review B **61** (6), R3768-R3771 (2000).

370. K. Jouda, S. Tanaka and O. Aita, Journal of Physics-Condensed Matter **9** (48), 10789-10794 (1997).

371. M. R. MacPherson, G. E. Everett, D. Wohlleben and M. B. Maple, Physical Review Letters **26** (1), 4 (1971).

372. T. Naka, T. Matsumoto and N. Mori, Physica B **205** (1), 121-126 (1995).

373. F. Porsch and W. B. Holzapfel, Physical Review Letters **70** (26), 4087-4089 (1993).

374. J. P. Rueff, J. P. Itie, M. Taguchi, C. F. Hague, J. M. Mariot, R. Delaunay, J. P. Kappler and N. Jaouen, Physical Review Letters **96** (23), 4 (2006).

375. J. A. Bradley, K. T. Moore, M. J. Lipp, B. A. Mattern, J. I. Pacold, G. T. Seidler, P. Chow, E. Rod, Y. M. Xiao and W. J. Evans, Physical Review B **85** (10), 5 (2012).

376. J. Akella, S. T. Weir, Y. K. Vohra, H. Prokop, S. A. Catledge and G. N. Chesnut, Journal of Physics-Condensed Matter **11** (34), 6515-6520 (1999).

377. N. Velisavljevic, Y. K. Vohra and S. T. Weir, High Pressure Research **25** (2), 137-144 (2005).

378. P. W. Anderson, Physical Review **124** (1), 41-& (1961).

379. R. D. Cowan, *The Theory of Atomic Structure and Spectra*. (University of California Press, Berkeley, 1981).

380. A. K. McMahan, R. T. Scalettar and M. Jarrell, Physical Review B **80** (23), 11 (2009).

381. A. K. McMahan, Physical Review B **72** (11), 14 (2005).

VITA

Devon Mortensen was born in Walnut Creek, California on May 9, 1986, the third child of Steven Mortensen and Kathleen Tuck. In 1995, he moved with his family to Boise, Idaho where he graduated from Centennial High School in 2004. From 2005-2007 he served a church mission in Sri Lanka, Malaysia, and Singapore. Upon his return he continued his undergraduate studies at Brigham Young University. During this time he had his first encounter with experimental physics, working with Prof. David Allred in the Extreme-Ultraviolet (XUV) research group. After graduating summa cum laude with a BS in physics from BYU in 2010, Devon began his graduate studies at the University of Washington. In 2011 he joined Prof. Gerald Seidler's X-ray Spectroscopy group where he conducted the research comprising this Ph.D. dissertation.